ABSTRACT

Title of dissertation: THE LOW TEMPERATURE

MAGNETOCONDUCTANCE OF

DELTA-DOPED SILICON

Dan Francis Sullivan, Doctor of Philosophy, 2005

Dissertation directed by: Dr. Bruce E. Kane

Department of Physics

The low temperature electronic transport properties of delta-doped silicon are established here, in an effort to determine the technological limitations facing the construction of semiconductor wafers with monolayer doping profiles. Both phosphorous (Si:P) and boron (Si:B) delta-doped silicon wafers prepared by molecular beam epitaxy have been investigated. Devices fabricated from samples of these wafers were cooled to approximately 130 mK in a dilution refrigerator, where four wire resistance measurements were performed in the presence of magnetic fields both perpendicular and parallel to the plane of the devices. The data obtained was interpreted using the theory of weak localization.

For Si:P samples, the effective thickness of the delta-doped region can be inferred by comparing the magnetoconductance signal in parallel magnetic fields to

that of perpendicular fields. Using this technique on several different samples which were annealed at 850 °C, an estimate of the diffusivity of phosphorus in silicon at this temperature is established. In addition, it is shown that the primary mechanism for the loss of quantum mechanical phase coherence in these samples at low temperatures is the electron-electron interaction, and provide evidence for lattice defects enhancing this dephasing. For Si:B samples, the spin-orbit interaction is shown to dominate the dephasing, and the temperature dependence of this interaction is found to be substantially different from that observed in Si:P devices.

Based on these results, I conclude that specific epitaxial growth techniques must be followed if monolayer doping profiles are ever to be achieved in silicon. In addition, because this weak localization technique for measuring the thickness of delta-doped regions is highly sensitive and non-destructive, it may ultimately prove to be the most effective method yet established for probing ultra-thin doping profiles. Finally, several theoretical desiderata are established, which would enable a more accurate interpretation of experimental data.

THE LOW TEMPERATURE MAGNETOCONDUCTANCE OF DELTA-DOPED

SILICON

by

Dan Francis Sullivan

Dissertation submitted to the Faculty of the Graduate School of the

University of Maryland, College Park in partial fulfillment

of the requirements for the degree of

Doctor of Philosophy

2005

Advisory Committee:

 Professor Frederick C. Wellstood, Chair

 Doctor Bruce E. Kane

 Professor Chia-Hung Yang

 Professor James R. Anderson

 Adjunct Professor Keith C. Schwab

 Professor Thomas D. Cohen

To Amanda and Rosalee.

Acknowledgments

It is unfortunately impossible to acknowledge every individual who has contributed in one way or another to this dissertation. Accordingly the people who are mentioned below are those who have figured most prominently in these efforts.

I would first like to thank my dissertation advisor, Dr. Bruce Kane, for supporting me financially through the five plus years I worked for him. I also appreciate him giving me the opportunity to work on this project essentially independently, and for the many conversations we had which helped to deepen my understanding of delta-doping in silicon.

Dr. Phillip E. Thompson was a great help in preparing the epitaxially grown delta-doped wafers which were investigated in this dissertation. This research would not have been possible without his assistance, and I am grateful for the service he provided.

Professor Richard Webb, one of the pioneers in low temperature experiments involving weak localization, graciously provided extensive experimental consultations. His insights and recommendations have been incorporated throughout this work. Although he was originally slated to be the committee chair for this dissertation, an unfortunate set of circumstances prevented him from being able to do so. His presence is sorely missed, and I wish him the best of luck in his new post at the University of South Carolina.

I was blessed to have an outstanding group of coworkers at the Laboratory for

mathematics, and who will no doubt be pleased with the continuing evolution of the "new and improved version" he so often cites. My wife Amanda has truly been phenomenal with her patience and support throughout the long and arduous struggle that is graduate school. It's finally over, honey. Lastly, and perhaps most of all, I thank my beautiful daughter Rosalee, for being so impossibly perfect. You are the light of my life.

Contents

Chapter 1

Introduction

This introductory chapter provides a comprehensive framework for understanding the data and theoretical analysis presented throughout this dissertation. A brief outline of the material I will cover is included at end of this chapter.

1.1   Background

The importance of semiconductor physics in everyday life, and that of silicon, in particular, can hardly be overstated. Since the invention of the transistor by Bardeen, Brattain, and Shockley in 1948, semiconductor technology has steadily advanced, with transistors simultaneously becoming both faster and smaller. These devices have found applications in an endless list of areas, including basic scientific research, personal computers, and all aspects of communication and information technology. Indeed, the myriad of roles the internet now plays in our

lives would be impossible without the computational power provided by microprocessors, with *billions* of transistors integrated onto a single silicon wafer. State-of-the-art transistors now (2005) have dimensions of less than 100 nm, and the trend towards ever smaller devices, with a concurrent doubling of the transistor density on a single wafer every two years ("Moore's law"), is expected to continue for at least another decade.

There are, however, physical limits to this scaling. As the dimensions of these devices become smaller and smaller, the atomic nature of matter can no longer be ignored, and quantum mechanical phenomena, such as charging energies and tunneling events, become manifest. Ultimately, the ability to control doping profiles in semiconductors with *atomic precision*, will determine how small functional devices, such as transistors, can be built. The technique known as *delta-doping* of semiconductors represents the frontier in this effort [1], and is the subject of research in this dissertation.

1.2 Definition

A single delta-doped region in a semiconductor is referred to as a delta-layer (δ-layer), and is simply an extremely thin layer of impurity atoms in an otherwise pure crystal. Ideally, the dopants occupy a single atomic layer (monolayer) in the lattice. A schematic representation of this situation is shown in Figure 1.1. Figure 1.1 (a) shows that the impurity atoms (dopants) are confined to a narrow, *planar* region of the crystal, "sandwiched" between two layers nominally devoid of

dopants. Figure 1.1 (b) shows a plot of the doping density, n(z), as a function of vertical position in the crystal. We see that n(z) = 0 everywhere except at the position z_0, hence the name δ-layer implies a "Dirac delta" doping distribution, $\delta(z - z_0)$. Mathematically, this ideal delta-doping profile n(z) is represented by

$$n(z) = n_{2D}\delta(z - z_0) \tag{1.1}$$

where n_{2D} is the *two-dimensional* density of atoms in the δ-layer. The relevant consideration for the work in this thesis (δ-layers in Si) is that an actual *physical* δ-layer, composed of real atoms, must possess a finite width, or have a thickness, $\mathcal{T}$, associated with it. Although the physical limit of $\mathcal{T}$ is a monolayer, all the samples investigated in this work, and thus far reported in the literature, far exceed this lower bound. Nonetheless, very thin ($\mathcal{T} \leq 5$ nm) δ-layers have been produced in a variety of semiconductors, and the ultimate limits in preparing these structures are still being explored.

1.3 Thickness Determination

One of the central questions I will address in this thesis is to quantify precisely how two-dimensional a given δ-doped sample is (that is, measuring $\mathcal{T}$). The way I approach this problem is through a *weak localization* analysis of low temperature, four-wire conductance measurements (σ), performed on δ-doped samples in the presence of a magnetic field (**H**); hence the term *magnetoconductance*, $\sigma(\mathbf{H})$. Both perpendicular ($\sigma(\mathbf{H}_\perp)$) and parallel ($\sigma(\mathbf{H}_\parallel)$) magnetic field configurations play an important role in this $\mathcal{T}$ measurement, as does as the temperature, T. The

3
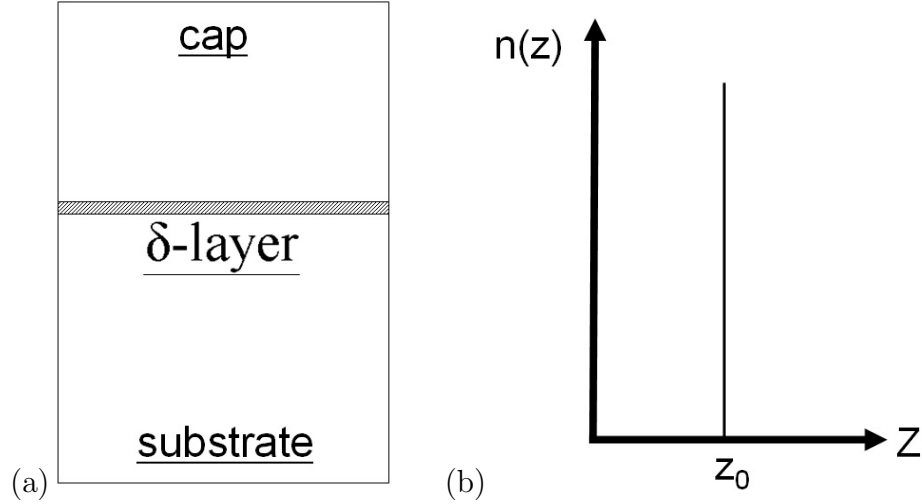
Figure 1.1: (a) Schematic representation of a δ-doped wafer, and (b), a plot of the doping density versus vertical position in the crystal for an ideal δ-layer. The doping density is zero everywhere except at the position z_0.

theory of weak localization will be discussed in Chapter 2, but for now it suffices to say that such a measurement of $\mathcal{T}$ amounts to a comparison of the effective cross sectional areas subtended by the δ-layer in $\mathbf{H}_\perp$ and $\mathbf{H}_\parallel$. To illustrate this idea, consider the right circular cylinder of radius R and height $\mathcal{T}$, sketched in Figure 1.2.

When viewed from "above" (corresponding to the $\mathbf{H}_\perp$ configuration), the observed cross sectional area is simply that of a circle: $A_\perp = \pi R^2$. If the cylinder is rotated and viewed from the side (corresponding to $\mathbf{H}_\parallel$), the cross section becomes rectangular, with area $A_\parallel = 2R\mathcal{T}$. Solving these two equations for $\mathcal{T}$ gives $\mathcal{T} = A_\parallel \sqrt{\pi/4A_\perp}$. Clearly, an accurate estimate of $\mathcal{T}$ requires a similar accuracy in determining the areas $A_\perp$ and $A_\parallel$. The discussion of weak localization
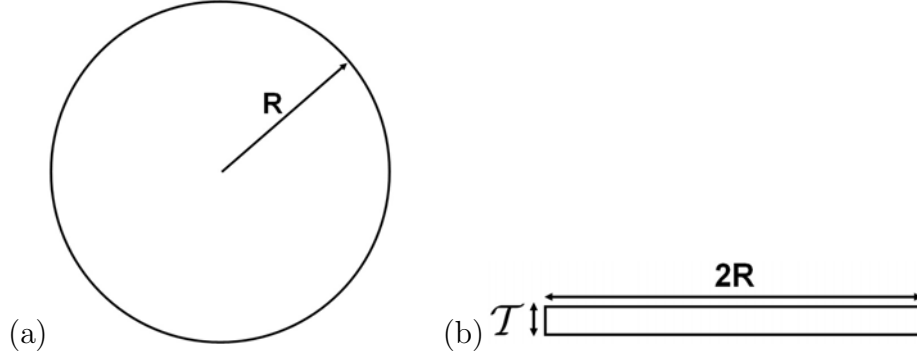
Figure 1.2: A weak localization measurement of the δ-layer thickness, $\mathcal{T}$, corresponds to a comparison of two effective cross sectional areas in perpendicular and parallel magnetic fields. In (a) (corresponding to $\mathbf{H}_\perp$), the appropriate effective area is $A_\perp = \pi R^2$. In (b) (corresponding to $\mathbf{H}_\parallel$), the effective area is $A_\parallel = 2R\mathcal{T}$. From these relations one obtains $\mathcal{T} = A_\parallel \sqrt{\pi/4A_\perp}$.

in Chapter 2 will make clear how this is done, as well as taking into account some of the details neglected in this simplified example.

To see how these considerations are involved in $\sigma(\mathbf{H})$ measurements, typical weak localization spectra for a phosphorous-doped silicon (Si:P) δ-layer sample are shown in Figure 1.3 (these measurements were taken at the base temperature of the dilution refrigerator used to cool the samples, $T \simeq 130$ mK). The upper curve corresponds to $\mathbf{H}_\perp$ data, the lower to $\mathbf{H}_\parallel$ data. The difference in the response of the conductance to $\mathbf{H}$ between the two configurations is obviously well-resolved. In general, $\sigma(\mathbf{H}_\perp)$ is always greater than $\sigma(\mathbf{H}_\parallel)$, and the more of a contrast that exists between the two configurations, the thinner is the δ-layer in the device. Again, by exploiting the asymmetry between $\sigma(\mathbf{H}_\perp)$ and $\sigma(\mathbf{H}_\parallel)$ and applying the
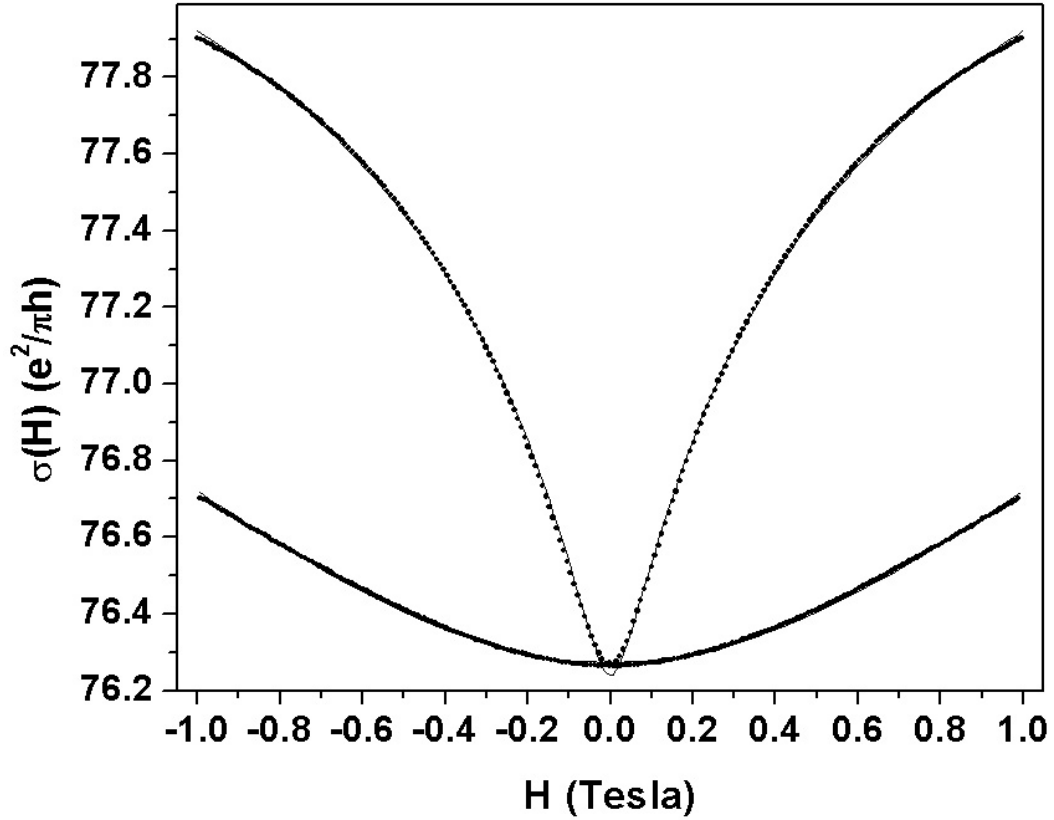
Figure 1.3: Typical weak localization data (points), with theoretical fits (solid lines). The upper curve corresponds to $\sigma(\mathbf{H}_\perp)$ data, the lower to $\sigma(\mathbf{H}_\parallel)$ data. The greater the difference between $\sigma(\mathbf{H}_\perp)$ and $\sigma(\mathbf{H}_\parallel)$, the *thinner* is $\mathcal{T}$.

appropriate theory to estimate the relevant cross sectional areas, a measurement of $\mathcal{T}$ is obtained.

Now that the reader has some feel for what will be presented in this dissertation, some justification for carrying out this work will be discussed.

1.4   Motivation

This dissertation research was originally motivated by an interest in quantum computing (QC), specifically the proposal of my advisor, Bruce Kane, [4]. The idea was to use individual P donors in crystalline Si (c-Si) as quantum bits ("qubits"). The requirements and implications of QC have been elaborated upon extensively elsewhere, and will not be discussed in any detail here, except to say that such an achievement would render certain formidable computations (e.g. factoring large numbers [5]) tractable.

Before QC can be achieved, however, many fundamental and practical questions must be addressed. One is how accurately can P donors can be placed in a Si crystal? This issue turns out to be of high importance for QC [6]. Various groups have made efforts to investigate the issue of precise P donor placement in c-Si through techniques such as scanning tunneling microscope positioning [7] and ion implantation [9], but perhaps the most readily available system for study are δ-layers grown by molecular beam epitaxy (MBE), as used in this thesis. Although other techniques for constructing δ-layers have been demonstrated (such as chemical vapor deposition (CVD) [8]), MBE offers many advantages, which will be presented in Chapter 3.

QC is far from the only application for δ-layer structures, however. They are widely used in charge coupled devices (CCDs) as highly efficient detectors for photons and low-energy fluxes in particle physics [10]. Another application is in resonant interband tunnel diodes (RITDs), which dissipate little power and are

therefore desirable for use in integrated circuits [12]. A possible future use of δ-layers is in the construction of single electron transistors (SETs), which have a host of potential applications, including use as a current standard in metrology [13] and ultra-sensitive charge detection [14].

I also note that δ-layers are of interest from a purely theoretical perspective. The electronic system associated with a δ-distribution is inherently two-dimensional, and some of the most striking discoveries in solid state research over the past 20 years stem from the physics of associated with two-dimensional electron gases (2DEGs). One of the most prominent is von Klitzing's discovery in 1980 [15] of the quantum Hall effect (QHE) in an Si MOSFET (Metal Oxide Semiconductor Field Effect Transistor). This effect now forms the basis for a resistance standard [16]. Another important discovery was of that the fractional quantum Hall effect (FQHE), first observed by Störmer and Tsui in 1984 [17] and explained theoretically by Laughlin in 1985 [18]. In the FQHE, charge carriers with a *fractional* electronic charge (e.g. 1/3, 2/3, 1/5, etc.) are observed in very high mobility (typically GaAs) heterostructures at low temperatures and high magnetic fields. δ-layers are a member of this exotic 2DEG family, but display carrier mobilities many orders of magnitude lower than their ballistic transport, high mobility MOSFET and GaAs cousins, and will consequently display rather different physical characteristics.

1.5 Prospectus

Chapter 2 will present those theoretical considerations most pertinent to this work. Specifically, the band structure of δ-layers in Si will be discussed, along with the impact this structure has on magnetoconductance measurements. Since this thesis hinges on interpreting such data using the theory of weak localization, a systematic treatment of this phenomenon is covered. Lastly, the subtle effect of a Berry phase and its influence on interpreting $\mathcal{T}$ using weak localization will be explored.

Chapter 3 is concerned with the samples used in my experiments. I include a brief discussion of previous efforts in preparing Si:P δ-layers, the MBE conditions necessary for constructing a δ-doped wafer, and the appropriate methods used in device fabrication. The presentation of the device fabrication process is rather "hands-on", and is meant to serve as a reference recipe to be followed in order to produce high quality devices for measurement.

Chapter 4 is perhaps the most important of the entire dissertation, and deals with the measurement techniques and equipment which were used to obtain my weak localization data. Since this is an experimental thesis, Chapter 4 will be somewhat more detailed in its exposition than the other chapters, and explains the precise conditions under which my magnetoconductance measurements were performed.

In Chapter 5 I present the results and analysis of my experiments, along with a discussion of the various systematic errors involved in the measurements. One

set of measurements is concerned with annealing several different devices constructed from the *same* Si:P δ-doped wafer, extracting $\mathcal{T}$ from each device as described in Chapter 2, and using this information to determine the diffusion coefficient of Si:P at T = 850 °C. Other experiments involve weak localization $\mathcal{T}$ measurements performed on devices constructed from *different* wafers with varying carrier densities, n. A brief account of measurements on a device constructed from a boron-doped silicon (Si:B) δ-layer is also presented, showing the dramatic influence of spin-orbit scattering has on $\sigma(\mathbf{H})$.

Chapter 6 summarizes my results and suggests new directions for future investigation.

The appendices cover ancillary points relevant my work, including a discussion of elementary transport theory, the programming code I used in data analysis, and the modifications and improvements I made to the dilution refrigerator I used. The works of the numerous authors who helped to lay the foundations for this research are listed in the bibliography.

Chapter 2

Theory

This chapter presents three theoretical aspects crucial to understanding the physics of delta-doped silicon. The first section is on the electronic band structure of a δ-layer system in Si, and how this structure influences the interpretation of magnetoconductance data. The second is an overview of the theory of weak localization and its use in probing δ-layer structures. Lastly, the phenomenon of a Berry or geometric phase is discussed, and I describe how this phase manifested itself in the magnetoconductance measurements I performed.

2.1   Band Structure

This section will describe the energy characteristics of electrons in Si, culminating with a theory particular to Si:P δ-layers.

2.1.1 General Considerations for Si

I will outline the main results for the band structure of Si here to establish specific numbers and notions pertinent to my work. These results are reasonably well-known, and are taken primarily from [19, 20, 21].

The term "band structure" refers to specifying the energy of an electron (or hole) in a given crystalline potential as a function of either wavevector $\mathbf{k}$, position $\mathbf{r}$, or both. The E($\mathbf{k}$) representation is often referred to as a dispersion relation, and in essence quantifies how the kinetic energy of an electron in a crystal depends on its direction of propagation. Since thorough discussions of this topic are in standard texts on solid state physics [2, 3], I merely summarize here.

Qualitatively, when in the presence of a *periodic* crystalline potential, solutions of the Schrödinger equation (Hψ = Eψ) have a range of energies over which no solutions exist. This is the origin of the electrical characteristics of solids, and, for the case of interest here, produces the energy (or band) gap, E_g, of crystalline Si (c-Si). To appreciate how this comes about, consider an isolated Si atom, with electronic configuration $1s^2 2s^2 2p^6 3s^2 3p^2$ (i.e. four valence electrons outside a closed Ne shell). Combining many such Si atoms into their lowest energy state produces a *covalently* bonded crystal, identical in structure to that of C atoms in diamond. In this crystal, each atom occupies the center of a tetrahedron, with nearest neighbor atoms positioned at the vertices of the tetrahedron, as depicted in Figure 2.1 (a). This is equivalent to a lattice constructed from *two* face-centered cubic (fcc) lattices (Figure 2.1 (b)), one copy of which is displaced
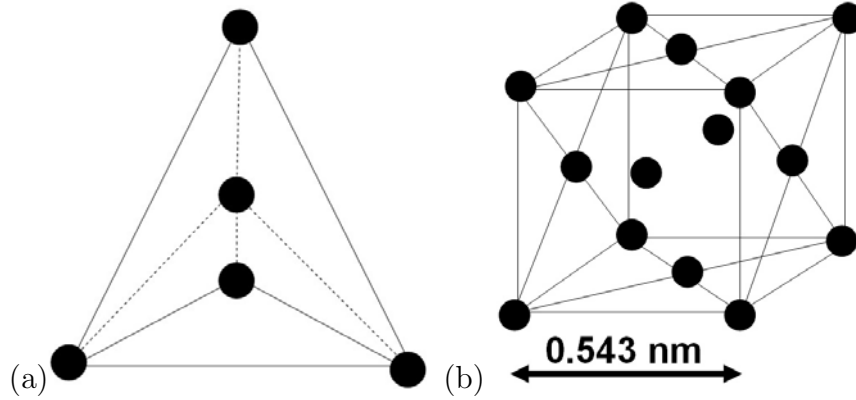
Figure 2.1: Crystal structure of Si. (a) tetrahedral structure, where each Si atom occupies the center of a tetrahedron. (b) fcc lattice. The c-Si lattice consists of *two* fcc lattices: one at the at the origin, the other 1/4 of the distance along the main body diagonal.

from the other 1/4 of the distance along the main cubic diagonal. To provide the appropriate length scale, x-ray crystallography has determined that the lattice constant for c-Si is $\simeq 0.543$ nm.

A generic semiconducting energy band diagram (in *position* space) is shown schematically in Figure 2.2. The states below the gap comprise the valence band (E_v), those above the gap the conduction band (E_c), and states with energies forbidden by the Schrödinger equation lie in E_g. In order for an electron (hole) to be transported through the crystal under the application of an arbitrarily small electric field $\mathbf{E}$, it must have an energy greater (less) than E_c (E_v). Of course, c-Si is an *indirect* gap semiconductor, meaning that the maximum of E_v and the minimum of E_c occur at different points of $\mathbf{k}$-space. Therefore the actual $E(\mathbf{k})$
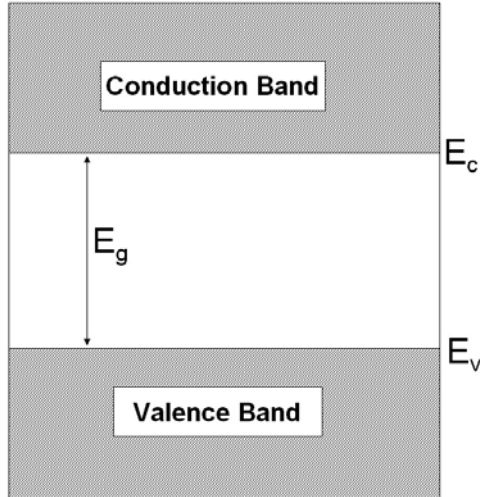
Figure 2.2: One-dimensional semiconductor energy band diagram (energy vs. position, E(x)). States with energies forbidden by the Schrödinger equation lie in the energy gap, which for Si at T = 0 is E_g = 1.17 eV. The **k**-space diagram [20] is *anisotropic*, and E_g varies with **k**.

band diagram for Si is much more complicated than that of Figure 2.2. Numerous measurements have determined that the maximum of E_v occurs at the center of the Brillouin zone (the "Γ" point), whereas the minimum of E_c occurs along the $< 100 >$ directions of **k**-space, approximately 3/4 of the distance from the center of the Brillouin zone to its boundary (the "Δ" points).

Due to the symmetry of the lattice, there is a $six - fold$ degeneracy associated with the minimum of E_c in Si, as depicted in Figure 2.3. The shape of these six conduction band valleys (or pockets) can be approximated by an ellipsoid whose eccentricity is specified by the effective mass tensor of the electrons. Cyclotron resonance measurements have established [22] that *two* effective masses are

14
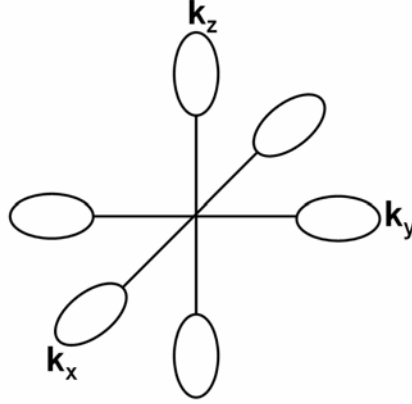
Figure 2.3: Si energy ellipsoids showing the six-fold conduction band degeneracy. The curvature near the ends of the ellipsoids corresponds to the transverse effective mass $m_\perp = 0.190 m_e$, while the curvature near the middle of the ellipsoids corresponds to the longitudinal effective mass, $m_\parallel = 0.916 m_e$

appropriate for characterizing these Si ellipsoids. Taking the center of a single pocket to be the **k**-space origin, E(**k**) takes the form

$$E(\mathbf{k}) = \frac{\hbar^2 k_x^2}{2m_\parallel} + \frac{\hbar^2 (k_y^2 + k_z^2)}{2m_\perp} \qquad (2.1)$$

with analogous expressions holding for the other symmetry-related pockets of Figure 2.3. Since $E \sim (1/m)$, a lighter mass corresponds to a more sharply curved portion of the energy ellipsoid. The results of [22] are $m_\parallel = 0.916 m_e$ and $m_\perp = 0.190 m_e$, where m_e is the free electron mass ($m_e \simeq 9.11 \times 10^{-31}$ kg). As the labels suggest, $m_\parallel$ corresponds to a **k** parallel to the major (long) axis of the ellipsoid, while $m_\perp$ corresponds to **k** perpendicular to the major axis.

Pure Si, being an intrinsic semiconductor, becomes an insulator at sufficiently low temperatures, with $E_g = 1.17$ eV at T = 0. In order to obtain a Si sample

15

which conducts even at T = 0, the crystal must be doped to a level greater than the metal-insulator transition (MIT) for the particular impurity element involved, defining the critical density, n_c. This in turn establishes a limit between the two-dimensional dopant density n in a δ-layer and its thickness $\mathcal{T}$. If $n < n_c\mathcal{T}$, the sample will not conduct at low temperatures, and cannot be investigated using weak localization techniques. The two Si dopants studied here, P and B, have $n_c = 3.7\mathrm{x}10^{18}/\mathrm{cm}^3$ and $4.0\mathrm{x}10^{18}/\mathrm{cm}^3$, respectively, while their *crystalline* ionization energies are 0.045 eV below E_c for Si:P, and 0.045 eV *above* E_v for Si:B (since B is a hole donor). Because these energies are near E_c and E_v respectively, and small compared with most other elements, P and B are known as "shallow donors" in Si.

I note here an interesting relationship which exists between n_c and the Si:P Bohr radius, a_B, which I shall refer to again in Chapter 5. First, at low temperatures it is legitimate to consider an isolated P atom in Si as an "effective Hydrogen atom" [23], since P has one more valence electron than Si, and the remainder of the crystal is insulating. Furthermore, the other Si atoms in the crystal act as a renormalized vacuum with dielectric constant κ. For Si, $\kappa = 11.9$ ϵ_0, where ϵ_0 is the permittivity of vacuum (in SI units $\epsilon_0 = 8.85\mathrm{x}10^{-12}$ $\mathrm{C}^2/\mathrm{N}\cdot\mathrm{m}^2$). Relating the kinetic energy (KE) to the potential energy (PE) of this system through the virial theorem (i.e. KE = PE/2) [24], the following relationship is obtained for a_B:

$$a_B = \frac{4\pi\kappa\hbar^2}{me^2}.$$ (2.2)

Using $m_\perp$ for m, I obtain $a_B \simeq 3.23$ nm, quite large compared to the Si lattice
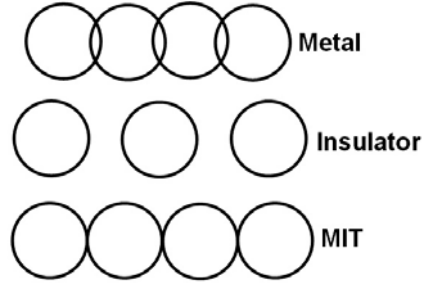
Figure 2.4: Sketch of the relationship between the conductivity of a sample and doping density. If the doping level is such that the mean donor d spacing is less than $2a_B$, the "Bohr diameter", the electron clouds (open circles) have considerable overlap, and the sample will conduct at T = 0 (i.e. it is metallic). If d > $2a_B$, the sample will insulate, and when d = $2a_B$, the MIT occurs.

spacing of 0.543 nm. The use of $m_\perp$ is only an approximation, and obviously equation (2.2) implies that a lighter electron will on average lie a greater distance from the nucleus.

The mean donor spacing at the MIT is given by taking the cube root of n_c for Si:P, for which I obtain d $\simeq$ 6.47 nm. Therefore the relationship d = $2a_B$ is nearly satisfied, to which a simple physical interpretation can be ascribed. If each P donor is thought of as a "conducting ball" of diameter $2a_B$, then Si:P samples will become insulating when these balls no longer touch. Thus, from an atomic point of view, the better a sample conducts, the greater is the electronic overlap bewtween donors. A depiction of this situation is shown in Figure 2.4. All of the samples studied in this work were metallic.

2.1.2 Density Functional Theory

The task of calculating the band structure for an arbitrarily doped, three-dimensional Si sample from first principles is, in general, intractable. Nevertheless, accurate numerical techniques have been developed to overcome this problem. For crystalline samples the most important result is Bloch's theorem, which states that the appropriate electronic wave functions can be expressed as the product of a plane wave and a periodic function, whose spatial period matches that of the crystal: $\Psi_{\mathbf{k}}(\mathbf{r}) = e^{i\mathbf{k}\cdot\mathbf{r}}\psi_n(\mathbf{k},\mathbf{r})$ ($\psi_n(\mathbf{k},\mathbf{r})$ is the lattice periodic function). The label n is the *band index*, and simply arranges the bands in order of increasing energy. Thus determining the band structure of a given crystal reduces to finding the functions $\psi_n(\mathbf{k},\mathbf{r})$. Many techniques have been developed which are in excellent agreement with experimental results for the energy gap, magnitude of carrier effective masses, etc., including Hartree-Fock calculations, density functional theory (DFT), and Monte Carlo and Green's function methods. I present a brief outline of DFT here. The other methods are discussed in [20] and the refernces therein.

DFT, first introduced by Hohenburg and Kohn in 1964 [25], asserts that the ground state energy of a many-body (N-electron) wave function can be transformed into N *one − electron* equations in which the electrons are subjected to an effective local potential, $V_{eff}(\mathbf{r})$. Since the properties of a homogeneous electron gas are well-known over a wide range of densities [26], characteristics of inhomogeneous systems can be calculated by "integrating over" a given

distribution, using the $V_{eff}(\mathbf{r})$ appropriate for a homogeneous gas. This DFT

approach is known as the "local density approximation" (LDA), and requires that

the density of electrons per unit volume, n($\mathbf{r}$), be a sufficiently slowly-varying

function of position. Precisely what constitutes "sufficiently slowly-varying" is a

problem-specific question, which is addressed in [25].

Once the potential of interest has been specified, DFT requires the

self − consistent solution of two coupled partial differential equations. These are

the Schrödinger equation (Hψ_i = E$_i\psi_i$) for the subband wave functions and

energies, and Poisson's equation (∇^2 V($\mathbf{r}$) = -$\rho(\mathbf{r})/\kappa$), relating the electrostatic

potential V($\mathbf{r}$) to the charge density ρ and dielectric constant κ.

To proceed, I first note Hohenberg and Kohn's result [25] for the ground-state

energy of an inhomogeneous, interacting electron gas in a static potential, $v(\mathbf{r})$:

$$E = e \int v(\mathbf{r})n(\mathbf{r})d\mathbf{r} + \left(\frac{e^2}{8\pi\kappa}\right) \int \int \frac{n(\mathbf{r})n(\mathbf{r}')d\mathbf{r}d\mathbf{r}'}{|\mathbf{r} - \mathbf{r}'|} + G[n]. \qquad (2.3)$$

In this equation G[n] is a universal *functional* of the density, G[n] = T[n] + $E_{xc}[n]$,

where T[n] is the kinetic energy and $E_{xc}[n]$ the exchange-correlation energy for a

system of *non − interacting* electrons. In the LDA, $E_{xc}[n] = \int n(\mathbf{r})\epsilon_{xc}(n(\mathbf{r}))d\mathbf{r}$,

where ϵ_{xc} is the exchange-correlation energy *per electron*, given n($\mathbf{r}$).

In this LDA limit, the ith electron's Schrödinger equation can be cast in the

form [27]

$$\{\frac{-\hbar^2\nabla^2}{2m} + [\phi(\mathbf{r}) + \mu_{xc}(n(\mathbf{r}))]\}\psi_i(\mathbf{r}) = E_i\psi_i(\mathbf{r}). \qquad (2.4)$$

Thus we have for the effective potential $V_{eff}(\mathbf{r}) = \phi(\mathbf{r}) + \mu_{\mathbf{xc}}(\mathbf{n}(\mathbf{r}))$ (i.e. an

19

"effective" Poisson equation). The two contributions to $V_{eff}(\mathbf{r})$ are given by

$$\phi(\mathbf{r}) = ev(\mathbf{r}) + \left(\frac{e^2}{4\pi\kappa}\right) \int \frac{n(\mathbf{r}')d\mathbf{r}'}{|\mathbf{r} - \mathbf{r}'|} \tag{2.5}$$

and

$$\mu_{xc} = \frac{d}{dn}(n\epsilon_{xc}(n(\mathbf{r}))). \tag{2.6}$$

Finally, $n(\mathbf{r})$ is given by the sum of the contributions to the density from the individual electrons:

$$n(\mathbf{r}) = \sum_{i=1}^{N} |\psi_i(\mathbf{r})|^2. \tag{2.7}$$

The pieces are now in place to self-consistently calculate a crystal's band structure. The typical procedure is that some initial $n(\mathbf{r})$ is assumed, and ϕ and μ_{xc} are calculated according to equations (2.5) and (2.6). Placing these quantities in the Schrödinger equation (2.4), the ψ_i's are determined. These wave functions are then used in (2.7) to obtain a new estimate for $n(\mathbf{r})$. By iterating this procedure many times, a solution is (hopefully) converged to rapidly.

2.1.3 δ-Layer Band Structure

I now present a calculation for the T $= 0$ band structure of δ-doped Si:P. The theory associated with this problem is discussed in Chapters 1 and 2 of [1]. A more general numerical calculation for Si:P δ-layers which I shall summarize subsequently has been performed in [31].

The approach I take in this calculation is to assume a planar doping distribution, and find the associated electronic potential energy. I then substitute this potential into the Schrödinger equation, and solve it for the energy eigenvalues

20
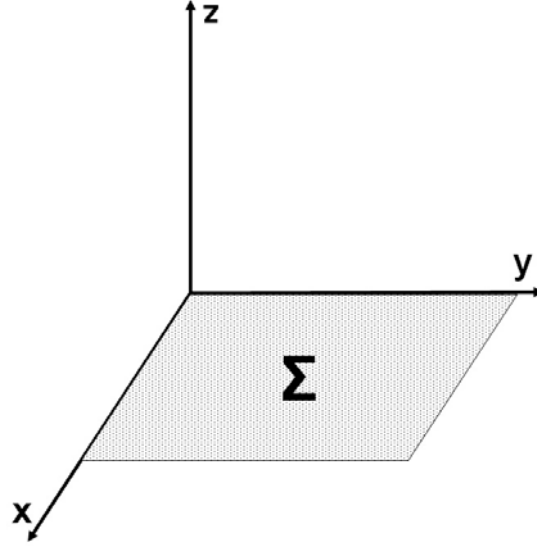
Figure 2.5: Planar charge distribution for modeling delta-doped Si:P. Σ is the charge density per unit area.

E_i and subband wave functions ψ_i. Finally, I determine the density of states, $\rho(E)$, of the system, and use $\rho(E)$ to find the Fermi energy, E_F, as a function of doping density by demanding charge neutrality.

Energy Eigenstates

As discussed in [28], the wavefunction for a general 2DEG can be approximated by the product of a plane wave $(e^{i\mathbf{k}\cdot\mathbf{x}})$ lying in the plane $z = 0$, and a subband wavefunction, $\psi_i(z)$, perpendicular to the plane. This section establishes the nature of the ψ_i.

Referring to Figure 2.5, I assume that a planar charge distribution, with charge density per unit area Σ, lies in the plane $z = 0$. Such a distribution acts as

a "quantum well", providing a confinement potential for the donor electrons. I further assume that Σ is proportional to the doping density n, and take $\Sigma = $ en for the remainder of this calculation (e is the electron charge, e $= 1.602 \times 10^{-19}$ C). A more general approach would be to take $\Sigma = \alpha$en, and examine the dependence of the results on α.

The electric field $\mathcal{E}$ produced by Σ is determined by applying Gauss's law in the standard "pillbox" form to this system, which yields a constant field in the $+/-\hat{\mathbf{z}}$ direction:

$$\mathcal{E} = \frac{\Sigma}{2\kappa}\hat{\mathbf{z}}. \tag{2.8}$$

Such a constant field leads to an electrostatic potential which is linear in z. Therefore the potential energy, V(z), of an electron a distance +/- z from the plane z = 0 is

$$\mathrm{V(z)} = e\mathcal{E}|\mathrm{z}| = \frac{e\Sigma}{2\kappa}|\mathrm{z}|. \tag{2.9}$$

The use of the absolute value of z in equation (2.9) reflects the fact that the energy of an electron in this potential is a symmetric function of z: E(z) = E(-z).

Given the potential energy defined by (2.9), the appropriate one-dimensional Schrödinger equation for subband wave function $\psi_i(z)$ with energy eigenvalue E_i becomes

$$\left(\frac{-\hbar^2}{2m_z}\right)\frac{d^2\psi_i}{dz^2} + \left(\frac{e\Sigma}{2\kappa}\right)|z|\psi_i = E_i\psi_i. \tag{2.10}$$

To solve equation (2.10), I note that the differential operator d^2/dz^2 - |z| has been studied since the 19th century, and the solutions to

$$\frac{d^2 f}{dz^2} - |z|f = -\lambda f \tag{2.11}$$

22

are the so-called Airy functions, Ai(z) and Bi(z), with eigenvalues λ [32]. An obvious physical boundary condition which the $\psi_i(z)$ must satisfy is that $\psi_i(z) \rightarrow 0$ as $|z| \rightarrow \infty$, which excludes the Bi(z) as possible wave function candidates. A second boundary condition is imposed on the z = 0 derivative of the $\psi_i(z)$ by the triangular symmetry of the potential (2.9). If the eigenvalues of (2.11) are indexed in increasing order, then the even index eigenvalues (0,2,4,...) are given by the negatives of the zeros of the *derivative* of Ai(z), while the odd index eigenvalues (1,3,5,...) correspond to the zeros of the Ai(z) itself [32]. Similarly, the even or odd parity of a particular $\psi_i(z)$ is determined by the parity of its index, with the even valued eigenfunctions satisfying $d\psi_i/dz = 0$ at z = 0.

To cast equation (2.10) in the form of (2.11), I rescale z according to x = Az, and substitute back into (2.10) to obtain:

$$\frac{d^2\psi_i}{dx^2} - \left(\frac{em_z\Sigma}{\kappa\hbar^2 A^3}\right)|x|\psi_i = -\left(\frac{2m_z E_i}{A^2\hbar^2}\right)\psi_i. \tag{2.12}$$

Choosing $A = (em_z\Sigma/\kappa\hbar^2)^{1/3}$, the left hand side of equation (2.12) is identical in form to that of (2.11), and therefore the right hand sides also equal each other. Thus the energy eigenvalues for the subband wave functions are given by

$$E_i = \lambda_i \left(\frac{e\Sigma\hbar}{\kappa\sqrt{8m_z}}\right)^{2/3} = \lambda_i \left(\frac{e^2\hbar n}{\kappa\sqrt{8m_z}}\right)^{2/3}. \tag{2.13}$$

Since electrons in Si have two possible values for m_z ($m_z = m_\perp$ and $m_z = m_\parallel$), a discrete spectrum of states exist for each of these masses. The complete energy spectrum for this system is shown plotted in Figure 2.6. In Table 2.1, the 10 lowest eigenvalues of equation (2.11) are listed [29], as well as the associated (rescaled) subband energies for either mass. Since $E \propto n^{2/3}$, all of the energies in

23
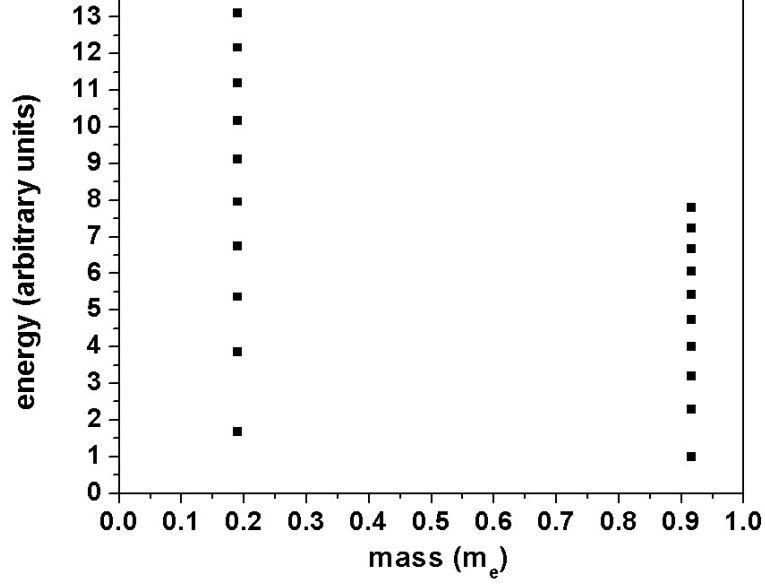
Figure 2.6: Energy spectrum of states corresponding to $m_\perp = 0.19 m_e$ and $m_\parallel = 0.916 m_e$ masses for Si. The energy of the various states have been rescaled such that $E_0 = 1$, where E_0 is the lowest available energy of the system (corresponding to $\lambda = 1.0187$ and $m = m_\parallel$ in equation (2.13)).

Figure 2.6 and Table 2.1 have been scaled relative to E_0, the lowest energy subband (i.e. $E_0 \equiv 1$). From equation (2.13), it is clear that E_0 has $m_z = m_\parallel$, $\lambda = 1.0187$, while the next lowest subband has $m_z = m_\perp$, $\lambda = 1.0187$, the next lowest $m_z = m_\parallel$, $\lambda = 2.3381$, etc.

A plot of the probability density $|\psi_i(z)|^2$ for i = 0,1,2,3 is shown in Figure 2.7. Each $\psi_i(z)$ satisfies $\int_{-\infty}^{\infty} |\psi_i^2|(z) dz = 1$, and for each increment in the index, an additional "lobe" appears in the wave function profile. The boundary conditions require that the origin be shifted for each $\psi_i(z)$, i.e. $\psi_0(z) \sim Ai(z-\lambda_0)$, $\psi_1(z) \sim Ai(z-\lambda_1)$, $\psi_2(z) \sim Ai(z-\lambda_2)$, etc [32].

24

Table 2.1: Table showing eigenvalues of equation (2.11) and corresponding (scaled) energy states for Si masses.

index	λ	$E(m_{\parallel})$	$E(m_{\perp})$
0	1.0187	1.00	1.68
1	2.3381	2.30	3.86
2	3.2482	3.19	5.36
3	4.0879	4.01	6.75
4	4.8201	4.73	7.95
5	5.5206	5.42	9.11
6	6.1633	6.05	10.17
7	6.7867	6.66	11.20
8	7.3722	7.24	12.16
9	7.9441	7.80	13.11
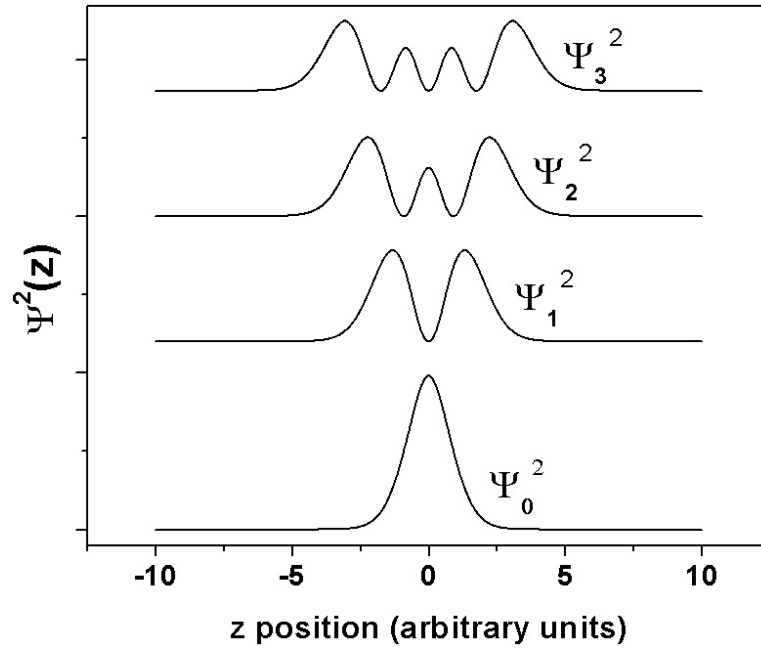
Figure 2.7: Probability densities $|\psi_i(z)|^2$ of the subband wavefunctions in δ-doped Si:P. As the band index increases, the wave functions become more extended. The ψ_i have been offset from each other vertically.

Density of States

In this section I calculate the density of states, $\rho(E)$, for an Si:P δ-doped

system. The motivation here is to understand the interplay between the

three-dimensional Si energy ellipsoids of Figure 2.3, and the two-dimensional

doping plane of Figure 2.5. Appendix A discusses the physical meaning of $\rho(E)$

(which has dimensions of 1/(energy)(area)), and calculates $\rho(E)$ for isotropic

(circular dispersion relation) and anisotropic (elliptical dispersion relation)

two-dimensional electron systems.

As shown in Appendix A, $\rho_1(E)$ for an isotropic, two-dimensional, single

subband electron system, with effective mass m*, is a constant, given by

$$\rho_1(E) = \frac{m^*}{\pi\hbar^2}. \tag{2.14}$$

For an *elliptical* dispersion relation in two dimensions, two masses, m$_1$ and m$_2$, are

required to specify $\rho_2(E)$:

$$\rho_2(E) = \frac{\sqrt{m_1 m_2}}{\pi\hbar^2}. \tag{2.15}$$

The two-fold spin degeneracy of the electrons is included in both (2.14) and (2.15).

Figure 2.8 shows why the two relations (2.14) and (2.15) are necessary for

modeling Si:P band structure. This figure is essentially the result of projecting the

ellipsoids of Figure 2.3 onto the doping plane of Figure 2.5. The cross section of

the ellipsoids perpendicular to the plane is circular, corresponding to $\rho_1(E)$, while

the cross section of the in-plane ellipsoids is elliptical, corresponding to $\rho_2(E)$.

Combining these two contributons, and ignoring, for the moment, the quantized
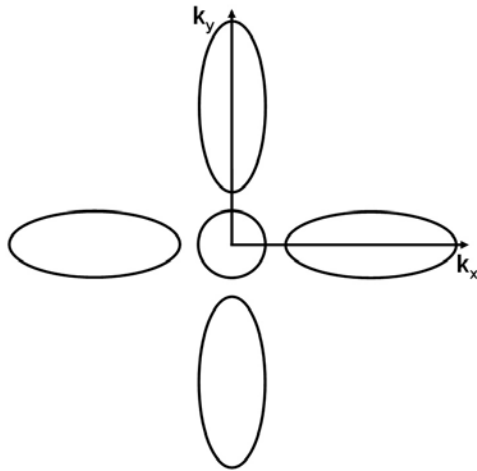
Figure 2.8: The two-dimensional density of states for Si (100). The energy ellipsoids of Figure 2.3 have been projected into the $k_z = 0$ plane, superimposing Si band structure on the doping distribution of Figure 2.5. Since equation (2.10) is concerned with motion perpendicular to this plane, the $m_{\parallel}$ subbands correspond to the circular area(s), the $m_{\perp}$ subbands to the ellipses.

nature of the energy states in this system, $\rho(E)$ for δ-doped Si:P is given by:

$$\rho(E) = \frac{2m_\perp}{\pi\hbar^2} + \frac{4\sqrt{m_\perp m_\parallel}}{\pi\hbar^2} = \rho_\parallel + \rho_\perp. \tag{2.16}$$

As suggested by the second equality, the first term in (2.16) corresponds to electrons with an $m_\parallel$ mass, the second to the $m_\perp$ mass. The prefactors of each reflect the degeneracies of the ellipses in Figure 2.8. I remark here that a counterintuitive distinction exists between the transport mass (m_t) and the density of states mass (m_ρ). For $m_t = m_\parallel$, $m_\rho = m_\perp$, while for $m_t = m_\perp$, $m_\rho = \sqrt{m_\perp m_\parallel}$.

To arrive at the final expression I shall use for $\rho(E)$ in Si:P δ-layers, I now take into account the discrete nature of the energy states calculated in the previous section. By plotting the energies in Table 2.1 in ascending order on a line (i.e. turning Figure 2.6 "on it's side"), it is (hopefully) clear that a given subband becomes occupied only if the most energetic electrons in the system (i.e. those at the Fermi energy, E_F) exceed the subband's energy eigenvalue. The lowest energy subband (E_0 in Table 2.1) corresponds to $m = m_\parallel$, the second lowest ($E_1 = 1.68$) to $m = m_\perp$, the next *two* lowest ($E_2 = 2.30$ and $E_3 = 3.19$) to $m = m_\parallel$, etc. Thus for $E_0 \leq E_F \leq E_1$, only a single subband is occupied, and $\rho(E) = \rho_\parallel$. For $E_1 \leq E_F \leq E_2$, two subbands are occupied, one for each mass, and $\rho(E) = \rho_\parallel + \rho_\perp$. For $E_2 \leq E_F \leq E_3$, three subbands are occupied (two for $\rho_\parallel$, one for $\rho_\perp$) and $\rho(E) = 2\rho_\parallel + \rho_\perp$. Continuing in this way, one can build up the "staircase" of the density of states for Si:P δ-layers, shown in Figure 2.9 (the vertical axis is scaled such that $\rho_\parallel = 1$). Comparing the two terms in equation (2.16), we see that for $\rho_\parallel = 1$, $\rho_\perp = 4.39$, and consequently it is easy to determine which steps in Figure 2.9 correspond
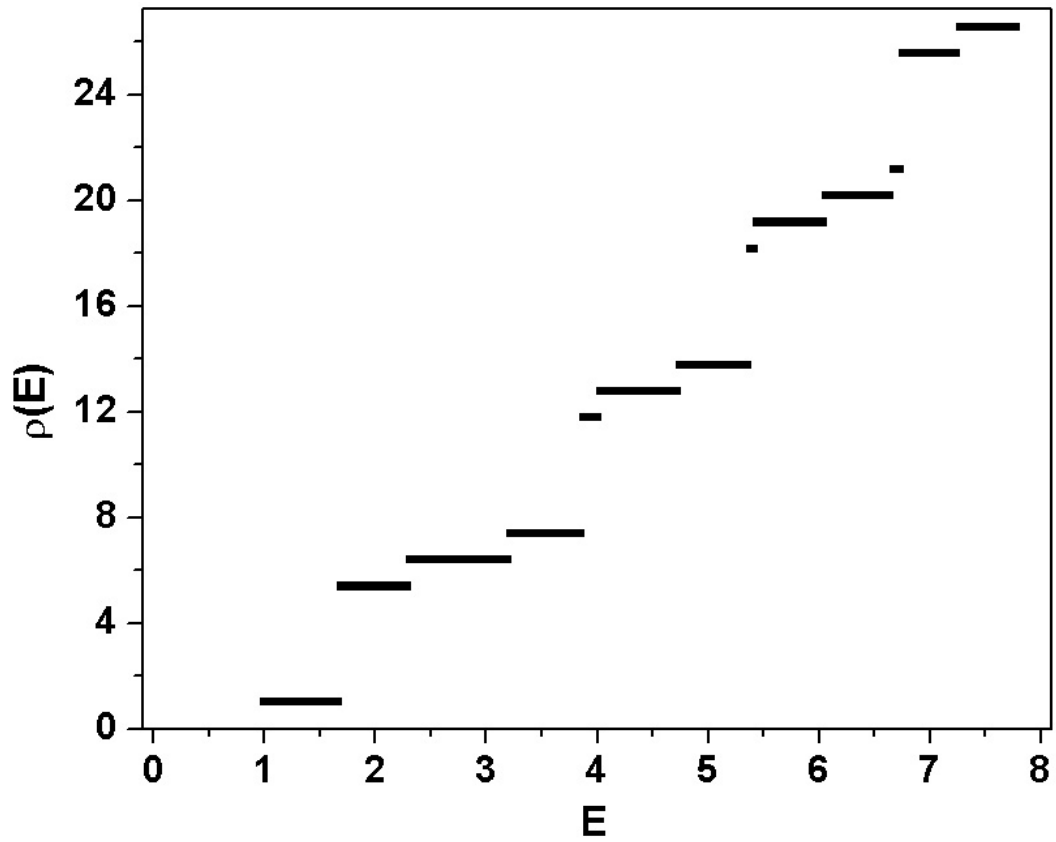
Figure 2.9: Staircase density of states $\rho(E)$ for δ-doped Si:P. The short vertical steps correspond to states with $m = m_\parallel$, large vertical steps correspond to states with $m = m_\perp$.

to $m_\perp$ or $m_\parallel$ states. The states with short (unit) steps correspond to $m_\parallel$, those with large steps to $m_\perp$ states.

With the step-like nature of $\rho(E)$ in Si:P δ-layers established, the final form I shall use in this dissertation is:

$$\rho(E) = \sum_i \rho_i \Theta(E_F - E_i). \tag{2.17}$$

Here $\Theta(x)$ is the Heaviside step function, defined as $\Theta(x) = 0$ for $x < 0$ and $\Theta(x) = 1$ for $x \geq 0$. ρ_i is either $\rho_\parallel$ or $\rho_\perp$, depending on whether E_i corresponds to an $m_\parallel$ or an $m_\perp$ state.

Fermi Energy

The final aspect of this calculation will be to determine the Fermi energy, E_F, of an Si:P δ-layer for arbitrary doping density, n.

For a single subband system, the following relation holds between n and $\rho(E)$ [2, 3]:

$$n = \int_{E_{min}}^{E_{max}} \rho(E) f(E) dE. \tag{2.18}$$

f(E) is the Fermi-Dirac distribution function. The integral (2.18) gives the number of electrons per unit area with energies between E_{min} (the lowest allowed energy in the band) and E_{max}. Since I am considering T = 0 in this computation, f(E) = 1 for E $\leq E_F$, and f(E) = 0 for E $> E_F$. Furthermore, having seen that $\rho(E)$ is constant for a 2DEG with a single subband, (2.18) becomes

$$n = \rho(E_{max} - E_{min}) = \rho(E_F - E_{min}) \tag{2.19}$$

since the integral is cut-off for $E_{max} > E_F$.

I now use (2.19) to determine the electron density at which the first subband is fully occupied. By setting $\rho = \rho_\parallel$, $\mathrm{E}_{min} = \mathrm{E}_0$ and $\mathrm{E}_F = \mathrm{E}_1$ in (2.19), and using equation (2.13) for the energies, I find that the first subband is filled when n = $3.39\mathrm{x}10^{12}/\mathrm{cm}^2$. Thus for densities greater than this, at least two subbands will be occupied. All of the samples I investigated in this work had densities greater than this value.

An analogous computation can be carried out for the second subband (i.e. for what n are the first two subbands filled?). In this case, n is given by:

$$n = \rho_\parallel(E_2 - E_0) + \rho_\perp(E_2 - E_1). \qquad (2.20)$$

Substituting in the appropriate quantities I obtain n = $6.46\mathrm{x}10^{14}/\mathrm{cm}^2$, which exceeds the highest density sample I investigated (n $\simeq 1.5\mathrm{x}10^{14}/\mathrm{cm}^2$) by roughly a factor of 4. Thus I conclude that all of the samples I measured in this work had two subbands occupied: one with $\mathrm{m}_z = \mathrm{m}_\parallel$, the other with $\mathrm{m}_z = \mathrm{m}_\perp$.

A relevant consideration here are the physical limits imposed on n. Obviously, n can be made arbitrarily small (zero doping limit), but in order to investigate a sample using weak localization it must have n $\geq \mathrm{n}_c = 2.39\mathrm{x}10^{12}/\mathrm{cm}^2$ (corresponding to the two-dimensional MIT for Si:P). There is also an upper limit to n: it can be no greater a monolayer Si (100) surface (1 ML = $6.78\mathrm{x}10^{14}/\mathrm{cm}^2$). In other words, for n > 1 ML, the doping distribution is no longer "δ-like" since the impurity atoms must begin to inhabit other lattice planes. Therefore, for truly planar Si:P doping distributions, a maximum of three subbands are occupied at T = 0.

The results of this calculation for $10^{11}/\text{cm}^2 \le \text{n} \le 10^{15}/\text{cm}^2$ are displayed in Figure 2.10. Plotted are the two lowest energy subbands for the $m_\parallel$ and $m_\perp$ masses, E_F, and the densities of the samples I have measured (labeled A, B, C, D). E_F was found by specifying n, calculating the necessary E_i from (2.13), substituting these into (2.19) or (2.20), and then solving the resulting expression for E_F. This ensures that the system obeys charge neutrality. Also labeled are the densities corresponding to the MIT and a ML doping level. According to this plot, all of the samples I measured had *two* subbands occupied.

Calculational Limitations

To illustrate some theoretical limitations of my calculational approach, I now compare my results for the band structure of δ-doped Si:P to those reported by Qian *et al.* in [31].

First, it should be clear that the potential energy approximation I used (2.9) cannot be correct, since V(z) increases indefinitely with |z|. In reality, if one assumes charge neutrality, the electric field of the donor nuclei must eventually be "screened" by the conduction electrons. In other words, sufficiently far from the δ-layer, V(z) should be *flat*, corresponding to zero electric field.

Accounting for this "band-bending" (and other factors) is done in [31]. These authors use a more general Schrödinger equation, approximating the δ-doped system by

$$[H_0 + V_{dop} + V_H + V_{xc}]\psi(\mathbf{r}) = E\psi(\mathbf{r}) \tag{2.21}$$

Here H_0 is the potential associated with a 1000 ML Si lattice, V_{dop} is the potential
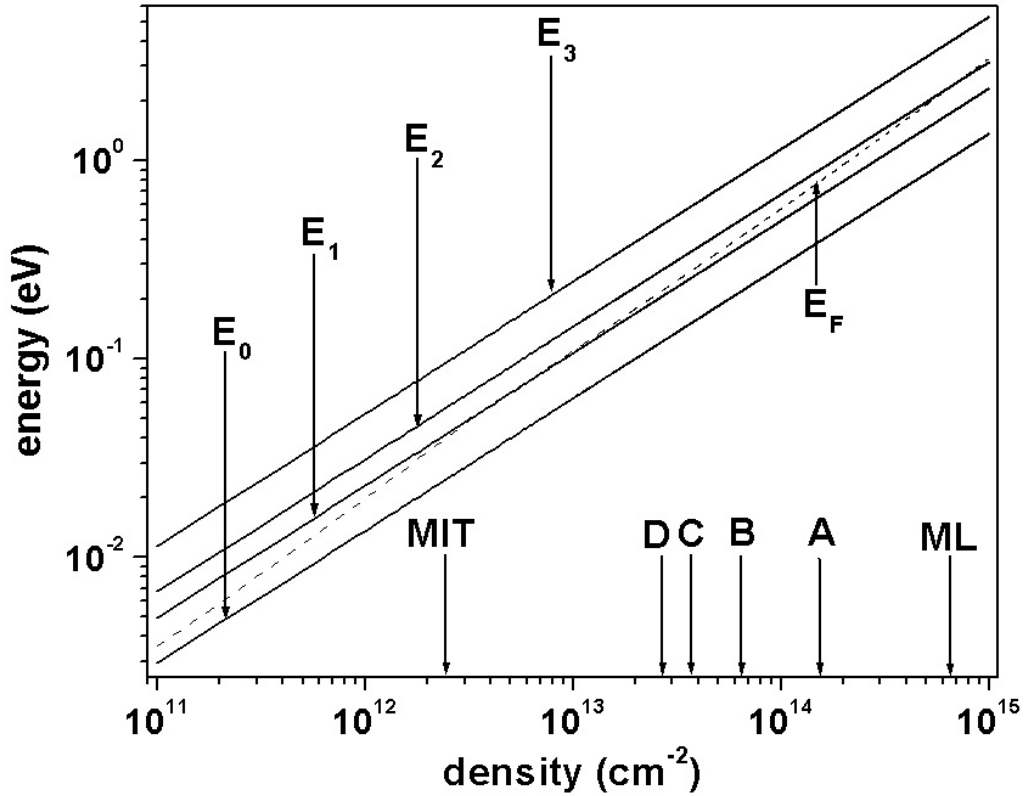
Figure 2.10: Results of calculation. E_0 and E_2 correspond to the two lowest energy subbands with with $m_z = m_\parallel$, E_1 and E_3 to the lowest energy subbands with $m_z = m_\perp$. The dashed line represents the Fermi energy, E_F. The E_1 subband starts to become occupied for a density n > $3.39 \times 10^{12}/\text{cm}^2$, the E_2 subband for n > $6.64 \times 10^{14}/\text{cm}^2$. For a 1 ML doping level (n = $6.78 \times 10^{14}/\text{cm}^2$), *three* subbands are occupied (two with $m_z = m_\parallel$, one with $m_z = m_\perp$). The approximate MIT density for δ-doped Si:P is shown, as well as the densities of the four samples measured in this work (A,B,C,D), discussed in Chapter 5. All of the samples measured in this work had two subbands populated: one with $m_z = m_\perp$, the other with $m_z = m_\parallel$.

due to the P dopants, V_H is the Hartree potential due to the electron-electron interaction, and V_{xc} the exchange-correlation potential of the electron gas. They assume a planar distribution of donors, in which the P atoms lie in a c(4x2) Si (100) surface reconstruction (see Chapter 5 of [20]). They ignore both spin-orbit scattering (which is weak in Si:P [30]), and "inter-pocket" scattering between the various energy ellipsoids in Figure 2.3. The band structure for this system is solved by by expanding $\psi(\mathbf{r})$ in a planar Wannier orbital (PWO) basis, which transforms the differential equation (2.21) into a finite-dimensional eigenvalue problem, enabling the appropriate eigenvalues and eigenvectors to be found. Since a PWO is the product of a two-dimensional plane wave and a one-dimensional Gaussian function, products of such PWOs have convenient computational properties.

Two classes of subbands result, labeled the "Γ" and "Δ" bands. Two Γ bands are found two exist, lying approximately 20 meV apart near the Γ point of the Brillouin zone, which correspond to the circles of Figure 2.8. The four equivalent Δ bands correspond to the in-plane ellipsoids of Figure 2.8. The dispersion relations for these subbands are

$$E_i(\mathbf{k}) = E_i^{(\Gamma)} + \frac{\mathbf{k}^2}{\mathrm{m}_\perp^*} \tag{2.22}$$

and

$$E_i(\mathbf{k}) = E_i^{(\Delta)} + \frac{(k_x - k^\Delta)^2}{\mathrm{m}_\parallel^*} + \frac{(k_y)^2}{\mathrm{m}_\perp^*}. \tag{2.23}$$

The effective masses are determined to be $\mathrm{m}_\perp^* = 0.211\mathrm{m}_e$ and $\mathrm{m}_\parallel^* = 0.95\mathrm{m}_e$, close to the values of $\mathrm{m}_\perp$ and $\mathrm{m}_\parallel$ for "normal" Si. Should the need arise, I will use these masses in subsequent calculations, and I define m_t^*, the *transport effective mass*

[34], by $m_t^* = 2m_\perp^* m_\parallel^* / (m_\perp^* + m_\parallel^*) \simeq 3.15 \times 10^{-31}$ kg.

Although [31] provides a more general calculation than I have performed, the results of both approaches are compatible. As an experimentalist, this is heartening, since it suggests a strong understanding of the fundamental physics governing δ-doped Si:P.

2.1.4 Perspective

The significance of subband structure in the context of 4-wire measurements can be appreciated by the fact that such a measurement actually *sums* the contribution of each subband to the total conductance signal. For example, when measuring the Hall resistance to obtain the carrier density n (see Appendix A), this quantity can be considered as the sum of the carrier densities n_i in each individual subband. Therefore, if there are M independent subbands populated in a given device, n is given by

$$n = \sum_{i=1}^{M} n_i. \tag{2.24}$$

Similar considerations apply to the measured conductance σ, assuming *independent* (decoupled) subbands. Labeling the ith subband's contribution by σ_i, and using the Drude expression for each component (see Appendix A), we arrive at

$$\sigma = \sum_{i=1}^{M} \sigma_i = \sum_{i=1}^{M} \left(\frac{n_i e^2 \tau_i}{m_i} \right). \tag{2.25}$$

Since I used $\sigma(\mathbf{H})$ to probe the thickness $\mathcal{T}$ of δ-layers (see Chapter 5), it is important to understand the contribution of each σ_i to $\mathcal{T}$. In the calculation I performed above, a perfectly planar distribution was assumed. However, Figure

2.7 clearly shows that even for a perfectly flat δ-layer, the spatial extent of the electronic distribution depends on which subband is considered. To establish a consistent definition for $\mathcal{T}$, I first define the thickness of the ith subband, $\mathcal{T}_i$, in terms of its mean-square variance in the $\hat{\mathbf{z}}$ direction:

$$\mathcal{T}_i = 2\sqrt{<z_i^2> - <z_i>^2} \tag{2.26}$$

where $<f(z)> = \int_{-\infty}^{\infty} f(z)\psi_i^*(z)\psi_i(z)dz$. Assuming only the i = 0 (lowest energy) subband is occupied, this reduces to [1]

$$\mathcal{T} = 2\sqrt{\frac{7}{5}}\left(\frac{4\hbar^2}{18em\mathcal{E}}\right)^{1/3}, \tag{2.27}$$

and evaluating this with "prototypical" device parameters (n = 10^{14}/cm^2, m = m$_t^*$ = 3.15x10^{-31} kg), I obtain $\mathcal{T} \simeq 1.1$ nm. Since $\mathcal{E} \sim$ n, as in (2.27), in general for this approximation $\mathcal{T} \sim$ n$^{-1/3}$. Thus even for a single subband and a perfectly planar distribution, different 2DEG thicknesses are obtained depending on the doping density n.

I note that although it is completely reasonable from a physical perspective that $\mathcal{T}$ of a 2DEG should vary with n, the assumed thickness of the donor distribution does *not* change with doping density. In fact, the donors in my calculation as well as [31] have been assumed to possess zero spatial extent; only the electrons are "spread out". I will neglect this effect in what follows, and assume equality between the thickness of the 2DEG, as inferred from $\sigma(\mathbf{H})$ measurements, and the donor distribution itself. This is reasonable if the donors are distributed in a non-planar fashion, which is the case for all of the samples I examined.

From equations (2.24) and (2.25), one might be tempted to define $\mathcal{T}$ as $\mathcal{T} = \sum \mathcal{T}_i$. However, given this definition, higher energy subbands, although generally less populated, would be weighted equally in the sum as the lower energy bands, whence $\mathcal{T}$ would be artificially enhanced. A more appropriate definition should take into account the fact that the $\mathcal{T}_i$ do *not* contribute uniformly to $\mathcal{T}$: they should be weighted by the subband population. Given this consideration, we are finally in a position to give a reasonable definition of $\mathcal{T}$. Using the fact that each subband contributes to n through (2.24), σ through (2.25), and $\mathcal{T}$ through (2.26) I define the "total 2DEG thickness signal" $\mathcal{T}$ by

$$\mathcal{T} = \sum_{i=1}^{M} \left(\frac{n_i}{n}\right) \mathcal{T}_i. \tag{2.28}$$

Since this is an experimental dissertation, it would have been preferable to determine the subband populations n_i through an actual measurement, instead of resorting to approximate theoretical calculations. Unfortunately, being able to resolve the contribution of each subband to the total conductance σ requires capabilities beyond those discussed in this thesis. For example, in order to infer subband occupations due to *Shubnikov de-Haas oscillations* in the magnetoresistance [2, 3], one needs to apply a field $|\mathbf{H}|$ of sufficient strength to render the cyclotron frequency ω_c at least as large as the elastic scattering rate $1/\tau_e$. Since $\omega_c = e|\mathbf{H}|/m$ and $1/\tau_e = \mathrm{v}_F/\ell_e$, this puts a lower bound on $|\mathbf{H}|$ of $|\mathbf{H}| \geq \hbar k_F/e\ell_e$. For our prototypical device n $\simeq 10^{14}/\mathrm{cm}^2$ and $\ell_e \simeq 25$ nm, which yields $|\mathbf{H}| \simeq 65$ T. This field is over 5 times stronger than the maximum $\mathbf{H}$ (12 T) the cryomagnetic system used in these measurements could attain at 4.2 K.

Accordingly the subband occupations could not be experimentally determined.

To conclude this section, I now clarify the model for the subband structure I will use for the remainder of this dissertation. What has been omitted from the work [1, 31] I have discussed are any physical effects which could lead to a *broadening* of the δ-layer band structure. This is significant, since if the energy levels of two subbands were broadened to the extent that their distributions overlaped considerably, they would then behave as as one *effective* subband. Some of the physical processes which could lead to subband broadening include inter-subband scattering, non-zero temperature, defects, a finite thickness of the δ-layer, fluctuations of $\mathcal{T}$ in a given sample, impurties, and surface effects. All of these play a role in "randomizing" the band structure of the δ-layer system. The issue of inter-subband scattering has been discussed theoretically in [33, 56], and experimentally in [34] (the measurements of [34] were on Si:Sb doped δ-layers). The results of [34] were that analysis with single subband models proved sufficient for modeling their data. Since my samples and those of [34] were both low mobility, δ-doped Si samples ($\mu \simeq 100$ cm^2/V·s), it seems reasonable to conclude that a similar approach applies here. In fact, single subband models were used for the data which will be dicussed in Chapter 5, and very good theoretical fits to the data were obtained, which experimentally justifies this approach. Thus I shall henceforth assume that a single, effective subband is responsible for the transport characteristics observed in this work.

With this single subband model in mind, I now discuss the theory of weak localization, and the application of this theory to δ-layer systems.

39
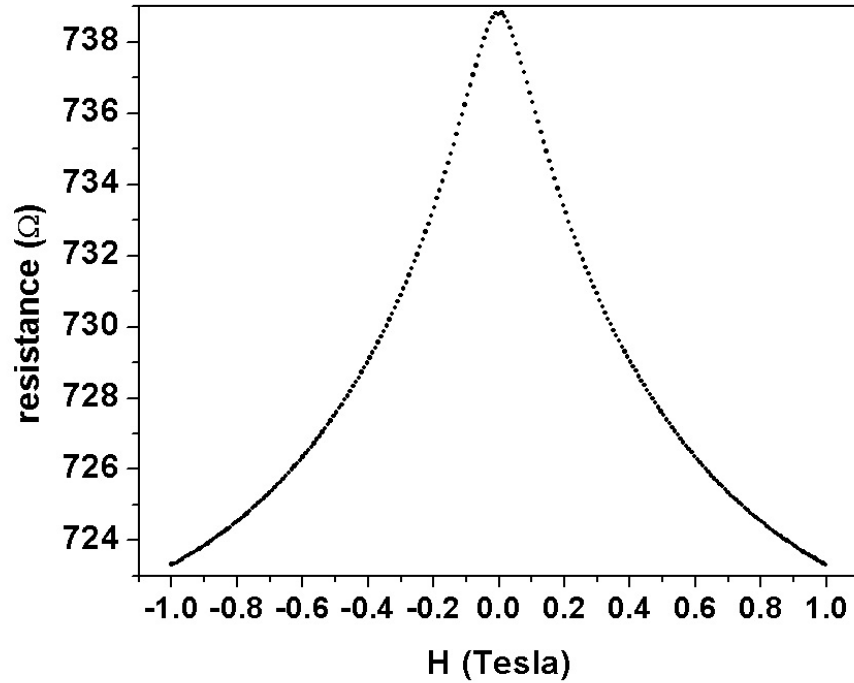
Figure 2.11: Longitudinal resistance of a δ-doped sample at T $\simeq$ 130 mK with a *perpendicular* magnetic field **H** applied. The sample displays a *negative magnetoresistance*, characteristic of the phenomenon of weak localization.

2.2 Weak Localization

2.2.1 Historical Development

Before stating any theoretical results, let us first examine magnetoresistance data from an Si:P δ-doped device taken in the presence of a perpendicular magnetic field **H** at T $\simeq$ 130 mK, shown in Figure 2.11.

We see that the resistance of the sample displays a *maximum* at **H** = 0, and

decreases monotonically for $|\mathbf{H}| \neq 0$. Such negative magnetoresistance had been observed in two-dimensional systems (such as depletion layers in MOSFETs) long before it was given a solid theoretical interpretation in the early 1980s. The questions I will address here are what causes this negative magnetoresistance to occur, and how can it be used to probe a δ-layer? Before doing so, however, a brief digression into the historical evolution of weak localization is appropriate.

The modern theory of weak localization starts with Anderson's observation [35] that a conductor which is sufficiently disordered will in fact *insulate* at $\mathrm{T} = 0$. Subsequent diagrammatic calculations carried out by Langer and Neal [36] showed that the so-called "maximally crossed" diagrams which contribute to the $\mathrm{T} = 0$ conductivity are divergent, and as we shall see, these are precsiely the diagrams used for carrying out computations of the weak localization correction to the conductivity. The scaling theory of localization, first espoused by Thouless [37], furthered our understanding of localization behavior by subdividing a conductor into *phase coherent* units, and investigating the effect boundary conditions between these units had on the macroscopic conductance (analogous to the overlap viewpoint of Figure 2.4). This led to the *theoretical* discovery by Abrahams *et al.* in 1979 that all two-dimensional systems insulate at $\mathrm{T} = 0$ [38]. The importance of the electron-electron interaction in understanding the behavior of disordered conductors was elaborated upon by many workers in the early 1980's, including seminal theoretical contributions by Altshuler [39] and Lee [40], among others, while experiments validating these theories have been demonstrated in numerous experiments, beginning with Dolan and Osherhoff [41]. Thorough presentations of

the theory of weak localization with references to the original literature can be found in the review articles by Bergmann [43] and Chakravarty and Schmid [44], as well as in [39, 40]. A more recent treatment can be found in the paper by Aleiner, *et al.* [45].

2.2.2 Quantum Conductivity

Often referred to as the "quantum correction" to the classical conductivity, the weak localization data shown in Figure 2.11 can be expressed as

$$\sigma(\mathbf{H}) = \sigma_0 + \delta\sigma(\mathbf{H}) \tag{2.29}$$

where σ_0 is the Drude ($\mathbf{H} = 0$) conductivity and $\delta\sigma(\mathbf{H})$ is the weak localization ($\mathbf{H} \neq 0$) contribution to the magnetoconductance. Here $\sigma(\mathbf{H}) = 1/\mathrm{R}_\square(\mathbf{H})$, and $\mathrm{R}_\square$ is the ohms/square resistivity of the device (see Chapter 4). This section will explore the nature of $\delta\sigma(\mathbf{H})$, including its quantum mechanical origin, magnitude and sign, etc.

As it turns out, the data of Figure 2.11, and therefore $\delta\sigma(\mathbf{H})$, can be understood by invoking a particular length scale into the problem. In addition to the mean free path, ℓ_e (Appendix A), the other length scale which can be inferred from such data is the *dephasing length*, ℓ_ϕ. The physics behind ℓ_ϕ is in some sense much more involved than that of ℓ_e, but is nevertheless conceptually easy to understand. Whereas ℓ_e is the average distance an electron can travel in a solid before undergoing an elastic (energy-conserving) collision, ℓ_ϕ is the corresponding distance for an *inelastic* (nonconservative) collison. Since the time evolution of a

quantum state with energy E is proportional to the phase $e^{-iEt/\hbar}$, any change in the state's energy will alter the evolution of the *phase* of the wave function. Given the fact that quantum mechanical probability distributions are extremely sensitive to phase relationships between state kets (i.e. matrix elements), measureable quantities including magnetoconductance are strongly influenced by these same phase correlations. The phase-breaking mechanisms in solids are the electron-electron, electron-phonon and spin-flip interactions [44]. As we shall see in Chapter 5, the electron-electron interaction is the most important for Si:P δ-layer physics.

To proceed with our explanation of Figure 2.11, consider Figure 2.12 (a), which shows a particle (electron) located at the initial position $\mathbf{r}_A$ at time t = 0. I now ask, what is the probability that it will be found at position $\mathbf{r}_B$ at some later time t? If we label the probability amplitude of an arbitrary path satisfying the specified conditions by A_α, elementary quantum mechanics dictates that the desired probability, $P_{A \to B}$, is given by the following expression [47]:

$$P_{A \to B} = \left(\sum_\alpha A_\alpha^* \right) \left(\sum_\beta A_\beta \right) \tag{2.30}$$

i.e. the squared-modulus of the sum over *all* appropriate amplitudes A_α. Carrying out the prescribed computation, I obtain

$$P_{A \to B} = \sum_\alpha |A_\alpha|^2 + \sum_{\alpha \neq \beta} A_\alpha^* A_\beta. \tag{2.31}$$

The first sum represents the classical probability of propagating from $\mathbf{r}_A$ to $\mathbf{r}_B$ along the various paths α. The second sum represents the quantum mechanical interference between arbitrary pairs of paths, labeled by α and β. For most pairs

43
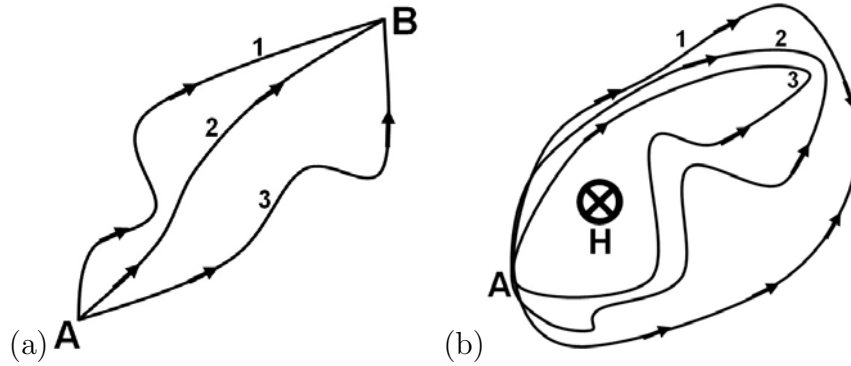
Figure 2.12: Paths from A to B. (a) The probability of propagating from A to B is given by summing the quantum mechanical amplitudes (equation (2.30)) for *all* appropriate trajectories. (b) When A = B, there is an enhanced probability for a particle to return to A (remain localized), and the resistance is maximal at $\mathbf{H} = 0$ ("coherent backscattering"). For $\mathbf{H} \neq 0$, a phase shift proportional to the flux through the loop is induced between oppositley directed paths, and the constructive interference is reduced, making the sample less resistive.

of paths, the phase accumulated along the separate trajectories is incoherent (oscillating near a *given point* $\mathbf{r}_B$ on the order of the Fermi wavelength, λ_F); thus the interference terms typically average to zero. However, if $\mathbf{r}_A = \mathbf{r}_B$, that is, we consider the *closed* trajectories of Figure 2.12 (b), the situation changes dramatically. Now each closed loop can be paired with a "time-reversed" counterpart, and whether a given loop is traversed clockwise ("forward in time") or counterclockwise ("backward in time") has no influence on the phase accumulation around the path. To explicitly illustrate this, let A_1 and A_2 represent the amplitudes for propagation around a given loop, corresponding respectively to clockwise and counterclockwise trajectories. Denoting the contribution of these two paths to $P_{A \to B}$ by p, we have

$$p = |A_1 + A_2|^2 = (A_1 + A_2)(A_1 + A_2)^* = 2|A_1|^2 + 2Re(A_1 A_2) = 4|A_1|^2. \quad (2.32)$$

I have used $|A_1|^2 = |A_2|^2$ in (2.32) due to the fact these trajectories are identical except for the direction of traversal. Note that if the contribution of the interference terms $A_1 A_2^*$ and $A_1^* A_2$ to p had been neglected, we would just have the classical probability $p = 2|A_1|^2$, one-half of that predicted by (2.32). Thus we see that these time-reversed paths are *coherent* (in phase), interfere *constructively*, and contribute to a higher probability of returning to $\mathbf{r}_A$ after a time t. These closed loop paths, collectively referred to as "Cooperons", are the source of the weak localization correction to the conductivity.

Suppose now that a uniform magnetic field $\mathbf{H}$ is "turned on" in the vicinity of these paths, and identify $\mathbf{A}$ as the vector potential corresponding to $\mathbf{H}$ in the

usual way [46] (i.e. $\mathbf{H} = \nabla \times \mathbf{A}$). The presence of $\mathbf{A}$ breaks the time-reversal

symmetry of the problem, and causes the wavefunction of a charged particle to

acquire an additional phase $\Delta\phi$ as it propagates around a loop, given by [47]

$$\Delta\phi = \left(\frac{e}{\hbar}\right) \oint \mathbf{A} \cdot d\mathbf{l} \qquad (2.33)$$

where $d\mathbf{l}$ is an infinitesimal length element tangent to the path. Since we are

considering here *closed* paths, Stokes' theorem ($\oint \mathbf{A} \cdot d\mathbf{l} = \oint (\nabla \times \mathbf{A}) \cdot d\mathbf{a} = \oint \mathbf{H} \cdot d\mathbf{a}$)

allows us to rewrite this expression for $\Delta\phi$ as

$$\Delta\phi = \left(\frac{e}{\hbar}\right) \Phi \qquad (2.34)$$

where Φ is the *magnetic flux* enclosed by the path. This path-dependent phase

accumulated by a charged particle in a magnetic field shows that, ultimately, the

phenomenon of weak localization is a particular manifestation of the

Aharonov-Bohm effect [48]. Accordingly, whether the charge traverses the loop

clockwise or counterclockwise affects the *sign* of the phase acquired, and the

amplitudes A_i in (2.30) must be transformed according to $A_i \rightarrow e^{i\Delta\phi} A_i$, as

required by gauge invariance. Taking this into account an re-computing p, I obtain

$$p = 2|A_1|^2(1 + cos(2\Delta\phi)). \qquad (2.35)$$

Thus, $\forall \mathbf{H} \neq 0$, the constructive interference which contributed to the "enhanced

backscattering" at $\mathbf{H} = 0$ is lost, and it becomes less probable for the charge to

return to its initial position. Hence the application of $\mathbf{H}$ renders the electrons in

the sample "less localized", which makes the device less resistive, and we are

finally able to appreciate the physical origin of the negative magnetoresistance

signal shown in Figure 2.11. In addition, the symmetry of the signal about $\mathbf{H} = 0$ can be understood by the $\sim \cos(2\Delta\phi)$ dependence of p on $\mathbf{H}$.

2.2.3 Calculation of $\delta\sigma(\mathbf{H})$

Although a start-to-finish calculation of $\delta\sigma(\mathbf{H})$ is too lengthy to be shown here, a brief sketch of the standard computational procedure is nonetheless appropriate, in order to appreciate the origin of the expressions which will be used for fitting data. The references cited earlier can be consulted for details.

As was shown in the previous section, Cooperons are responsible for the resistance maximum at $\mathbf{H} = 0$. Thus to calculate $\sigma(\mathbf{H})$ for a particular system, one must merely add up (integrate) the contribution of each Cooperon to obtain the total conductance signal. Several equivalent approaches include calculating $\sigma(\mathbf{H})$ using the Kubo-Greenwood formula [49], as done in [43], employing Abrikosov's result [50] for the residual resistance of a normal metal, as in [39], or through the use of linear response theory [51]. Since weak localization stems from the interference of electron waves as they *propagate* through an impurity distribution, it should come as no surprise that all of these methods employ *impurity averaged Green's functions* [50].

The interference between the time reversed paths which comprise the Cooperon can be conveniently represented using Feynman diagrams (a pedagogical introduction to the use of Feynman diagrams in many-body problems can be found in [52]). A representation of the appropriate diagrams for use in weak localization

calculations in **k**-space are shown in Figure 2.13 (a). Here a solid line corresponds to a single-particle propagator (Green's function), a wavy line to the amplitude for scattering off of an impurity, and the impurity itself by an open circle. Note that the *order* of impurity scattering between the upper propagator line ("forward in time") and lower line ("backwards in time") is reversed, as one would expect for the previously explained origin for the interference manifested by the Cooperon. Although only two scattering events are depicted here, the term "maximally crossed" diagrams is apparent from the figure, and simply refers to switching the order of the scattering sequence. If the lower propagator line is reversed, taking care to preserve the scattering sequence, the diagram is "uncrossed", and the interference between the two paths can be expressed by the "ladder diagrams" of Figure 2.13 (b). Taking into account all possible scattering sequences by summing the obvious geometric series suggested by Figure 2.13 (b), an integral equation is obtained for the Cooperon, commonly referred to as the *Dyson equation*. The diagrammatic representation for Dyson's equation is shown in Figure 2.13 (c).

A few final comments about calculations of $\delta\sigma(\mathbf{H})$ will now be made.

First, it is important to note that not all closed paths in the sample contribute to the weak localization signal: there is a cut-off parameter, namely ℓ_ϕ, which defines the average size of the phase coherent region in the sample. Furthermore, ℓ_ϕ is temperature dependent. In general, this dependence is logarithmic on the temperature, raised to a power p: $\ell_\phi \sim \ln(\mathrm{T}^{-p})$ [40]. In other words, ℓ_ϕ should diverge as $\mathrm{T} \to 0$. This can be understood by the fact that the phase-breaking rate corresponding to the electron-electron interaction varies as $1/\tau_{e-e} \simeq \mathrm{T}^2/\mathrm{E}_F$,
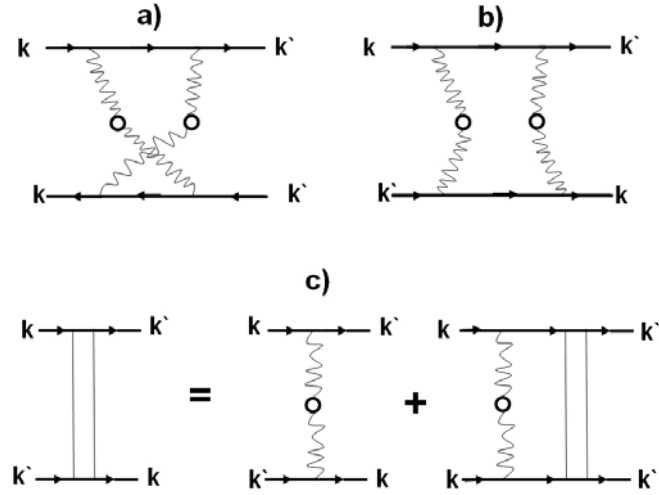
Figure 2.13: Feynman diagrams in **k**-space for calculating $\delta\sigma(\mathbf{H})$. In (a), the interference between "forward" in time electrons (upper lines), and "backward" in time electrons (lower lines) is accounted for by reversing the scattering sequence under consideration, hence the term "maximally crossed" diagrams. This is equivalent to the "ladder diagram" in (b), where the interference is between two forward in time paths, but with **k** vectors switched. Summing all such diagrams leads to the Dyson equation, represented by (c). See [52] for a discussion of Feynman diagrams in the many-body problem.

while that of the electron-phonon interaction varies as $1/\tau_{e-ph} \simeq \mathrm{T}^3/\Theta_D^2$ [45] (E_F is the Fermi energy, Θ_D the Debye frequency). For c-Si, $\Theta_D \simeq 1$ THz [20], whence it is clear that $1/\tau_{e-e}$ will dominate at low temperatures.

Second, since the phase accumulated around a given path is extremely sensitive to magnetic fields, the device under consideration must be free of magnetic impurities. In addition, if any spin-orbit effects are present in the sample, this will also cause a path-dependent phase shift. In fact, the spin-orbit interaction is quite strong in Si:B δ-doped samples, and as we shall see in Chapter 5, produces very different magnetoresistance behavior than that of Figure 2.11.

Finally, the effective dimensionality of the sample is important, and different corrections apply depending on the geometric properties assumed in the calculation. All of the samples in this work are considered to be effectively two-dimensional, but one-dimensional weak localization has also been extensively studied experimentally.

Having said all this, it should be apparent that a great deal of theory has been developed to produce useful expressions for fitting experimental data obtained from 2DEGs. Here I simply state that when placed in a *perpendicular* magnetic field ($\mathbf{H}_\perp$), the prediction for the measured change in conductance of a 2DEG system is given by [53]:

$$\delta\sigma(H_\perp) = (\frac{-e^2}{2\pi^2\hbar}) \left[\Psi\left(\frac{1}{2} + \frac{H_1}{H_\perp}\right) - \left(\frac{3}{2}\right)\Psi\left(\frac{1}{2} + \frac{H_2}{H_\perp}\right) - \left(\frac{1}{2}\right)\Psi\left(\frac{1}{2} + \frac{H_3}{H_\perp}\right) \right]$$

(2.36)

where $\Psi(\mathrm{x})$ is the *digamma function*, the "logarithmic derivative" of the gamma

function. $\Psi(x) = \frac{d}{dx}\ln(\Gamma(x))$, and asymptotically approaches the natural logarithm ln(x) for large x. The characteristic fields $H_{1,2,3}$ are associated with the transport relaxation mechanisms of impurity potential scattering (H_0), inelastic scattering (H_i, including electron-electron and electron-phonon interactions), spin scattering (H_s), and spin-orbit scattering (H_{so}), as follows [43, 53]:

$$H_1 = H_0 + H_{so} + H_s \tag{2.37}$$

$$H_2 = \frac{4}{3}H_0 + \frac{2}{3}H_s + H_i$$

$$H_3 = 2H_s + H_i.$$

In turn, a relaxation *time*, τ_i, can be associated with the H_i through

$$H_i\tau_i = \frac{\hbar}{4eD} \tag{2.38}$$

where D is the electronic diffusivity. In two dimensions, $D = v_F^2\tau_e/2$. Although in principle knowledge of the carrier effective mass would allow one to estimate D fairly accurately, the best way of independently determining D is through measurements at high frequencies [57]. Since this was not done here, I will henceforth equate an effective *length* with H_i and τ_i via

$$\ell_i = \sqrt{D\tau_i}. \tag{2.39}$$

Fortunately, equation (2.36) can be simplified considerably in the case of Si:P δ-layers, as previous work has shown that both spin and spin-orbit scattering in Si:P are weak [58]. Therefore, the relaxation times associated with these processes are very large, and can be neglected when compared with the electron-electron and

electron-phonon interactions. Taking this into account, I arrive at the final

expression I will use for modeling $\delta\sigma(H_\perp)$ in Si:P δ-layers:

$$\delta\sigma(H_\perp) = (\frac{e^2}{2\pi^2\hbar})[\Psi(\frac{1}{2} + \frac{\hbar}{4eH_\perp\ell_\phi{}^2}) - \Psi(\frac{1}{2} + \frac{\hbar}{2eH_\perp\ell_e{}^2}) + \ln(\frac{2\ell_\phi{}^2}{\ell e^2})] \qquad (2.40)$$

where ℓ_ϕ is the previously defined dephasing length ($\ell_\phi = \sqrt{D\tau_\phi}$), and ℓ_e the

elastic mean free path.

If instead the magnetic field is applied *parallel* to the 2DEG ($\mathbf{H}_\parallel$), the

appropriate expression takes the form [54, 55, 56]

$$\delta\sigma(H_\parallel) = (\frac{e^2}{2\pi^2\hbar})\ln(1 + \gamma H_\parallel^2). \qquad (2.41)$$

The physical interpretation of the parameters ℓ_ϕ and γ in the context of measuring

$\mathcal{T}$ will become apparent presently.

As discussed in Chapter 1, using weak localization to measure $\mathcal{T}$ corresponds

to a *cross section* comparison of the 2DEG in $\mathbf{H}_\perp$ and $\mathbf{H}_\parallel$ configurations. Now

that I have discussed the physical origin of the negative magnetoresistance in

Figure 2.11 (namely magnetic field dependent quantum interference effects), I

present a phenomenological approach for determining $\mathcal{T}$.

2.2.4 $\mathcal{T}$ Phenomenology

This section uses straightforward dimensional analysis to find an expression

for $\mathcal{T}$ in a δ-layer using weak localization data. Although reasonably simple, this

analysis reveals certain features of this approach to measuring $\mathcal{T}$ which *all* models

have in common.

To proceed, consider the data in Figure 1.3, which shows both $\sigma(\mathbf{H}_\perp)$ (corresponding to the upper curve in the figure) and $\sigma(\mathbf{H}_\parallel)$ (lower curve). For a *particular* value of magnetic field, say $\mathbf{H_0}$, the graphs show that the maximum value of $\sigma(\mathbf{H_0})$ is attained when $\mathbf{H_0} = \mathbf{H}_\perp$, while the minimum occurs for $\mathbf{H_0} = \mathbf{H}_\parallel$. Furthermore, both curves are *symmetric* functions of $\mathbf{H}$ (i.e. $\sigma(\mathbf{H}) = \sigma(-\mathbf{H})$), which suggests that $\sigma(\mathbf{H})$ can be represented by a Taylor series expansion with only even powers of $\mathbf{H}$:

$$\sigma(H_{\perp,\parallel}) = \sum_{n=0}^{\infty} \sigma_{2n} H_{\perp,\parallel}^{2n}. \tag{2.42}$$

Then to lowest non-vanishing order in $\mathbf{H}$, we can write

$$\delta\sigma(H_\perp) = \gamma_\perp H_\perp^2 \tag{2.43}$$

$$\text{and}$$

$$\delta\sigma(H_\parallel) = \gamma_\parallel H_\parallel^2$$

(this *is* the lowest order Taylor expansion of equation (2.41)). From our discussion of weak localization and the data of Figure 1.3, it is clear that a greater magnetic flux penetrates the 2DEG when $\mathbf{H} = \mathbf{H}_\perp$ (since the conductance is higher), and therefore that we can associate an effective area, A_{eff} (or cross section), with $\gamma_\perp$ and $\gamma_\parallel$, as follows.

First, I adopt the convention that $\delta\sigma(\mathbf{H})$ is dimensionless, measured in "Cooperon units" of $e^2/2\pi^2\hbar = e^2/\pi h$. Then in order for both sides of equation(s) (2.43) to be dimensionless, γ must have units of $1/T^2$. Because weak localization is due to interference between *pairs* of paths, the natural units of magnetic flux in

this problem are $\hbar/2e$, and this combination of physical constants has dimensions of T·m^2. Hence the desired relationship between γ and A_{eff} in this approximation is given by

$$\gamma = \left(\frac{2eA_{eff}}{\hbar}\right)^2.$$

(2.44)

The "cross section" argument presented in Chapter 1 is shown again in Figure 2.14. When $\mathbf{H} = \mathbf{H}_\perp$, all directions in the 2DEG should be treated symmetrically, which suggests that a circle is the appropriate cross sectional area to be associated with $A_\perp$. Furthermore, the characteristic length scale of the 2DEG in this configuration is ℓ_ϕ, and using this (subjectively!) as the *diameter* of the circle, we have

$$\gamma_\perp = \left(\frac{e\pi\ell_\phi^2}{2\hbar}\right)^2.$$

(2.45)

On the other hand, when $\mathbf{H} = \mathbf{H}_\parallel$, all directions in the device are not equivalent, since, due to the confinement potential, the wavefunction is coherent in the direction perpendicular to the doping plane. In fact, if the sample is to be considered two-dimensional from a quantum mechanical perspective, the condition $\mathcal{T} < \ell_\phi$ must hold [54]. Assuming this is the case, the cross sectional area for $\mathbf{H} = \mathbf{H}_\parallel$ is rectangular, with length ℓ_ϕ and height $\mathcal{T}$. That is,

$$\gamma_\parallel = \left(\frac{2e\mathcal{T}\ell_\phi}{\hbar}\right)^2.$$

(2.46)

Solving equation (2.46) for $\mathcal{T}$ yields

$$\mathcal{T} = \frac{\hbar\sqrt{\gamma_\parallel}}{2e\ell_\phi}.$$

(2.47)

Note that this expression relates $\mathcal{T}$ of the δ-layer to the perpendicular field
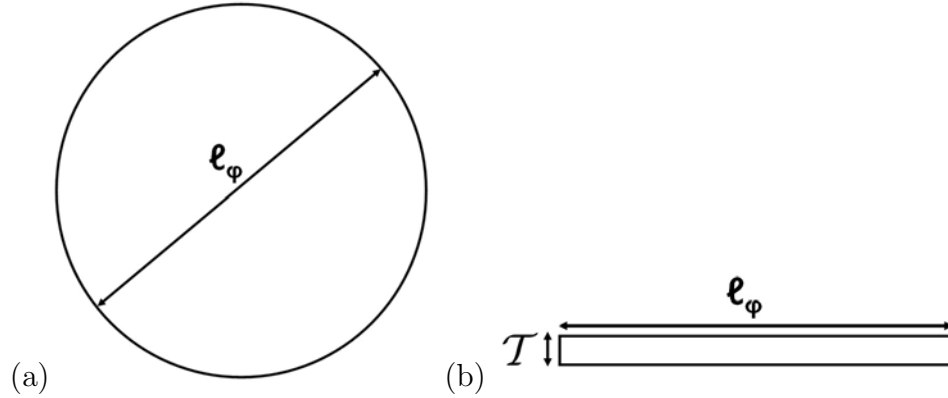
Figure 2.14: Effective cross sectional areas for $\mathbf{H}_\perp$ (a) and $\mathbf{H}_\parallel$ (b), and the corresponding weak localization length scales for defining these areas.

parameter ℓ_ϕ (derived from (2.45)) and the parallel field parameter γ (from (2.46)) as $\mathcal{T} \sim \sqrt{\gamma}/\ell_\phi$. Because $\sigma(\mathbf{H})$ is symmetric with respect to $\mathbf{H}$ but highly anisotropic, *all* weak localization models of $\mathcal{T}$ will have this form.

The rectangular model used in this analysis is of course too simple to accurately describe real δ-layer systems. This ties in with the principal difficulty one is faced with when using parallel field weak localization techniques to measure $\mathcal{T}$: proper modeling of γ in equation (2.41). I discuss this further in the following section on Berry phase.

2.3   Berry Phase

The notion of a Berry phase, also known as a geometric phase, is ubiquitous in physics. Although the modern form of Berry's theorem was not formulated until 1984 [59], the importance of path dependent phenomena in various physical

contexts has been appreciated for centuries. A familiar classical example of a geometric phase is the precession of a (Foucault) pendulum due to the rotation of the earth. The observed angular deflection of the pendulum from it's initial trajectory corresponds to a geometric phase, and depends on parameters such as how long the pendulum has been in motion and it's latitudinal position on earth. The phenomenon of weak localization itself is an example of a Berry phase, since it is based on the interference between oppositely directed Aharonov-Bohm paths, as described in the previous section. I now discuss the particular considerations of Berry phase pertinent to this work. A comprehensive discussion of Berry phase, with numerous physical examples, is contained in the book

Geometric Phases in Physics, by Wilczek and Shapere [60].

2.3.1 2DEG Berry Phase

The importance of Berry's phase in the context of 2DEGs subjected to parallel magnetic fields has been appreciated and elaborated upon previously [61, 62]. Since in essence weak localization measures a magnetic field induced electronic phase difference, it is important to distinguish whether this phase is due to Aharonov-Bohm interference, or results from the intrinsic geometry of the system. An artificial example of this effect is illustrated in Figure 2.15. The top panel (a) shows a perfectly flat 2DEG with thickness $\mathcal{T}$, the middle panel (b) a 2DEG also of thickness $\mathcal{T}$, but with a periodic "ripple" superimposed upon it. If an electron is confined to follow the boundary of these samples, say through the application of
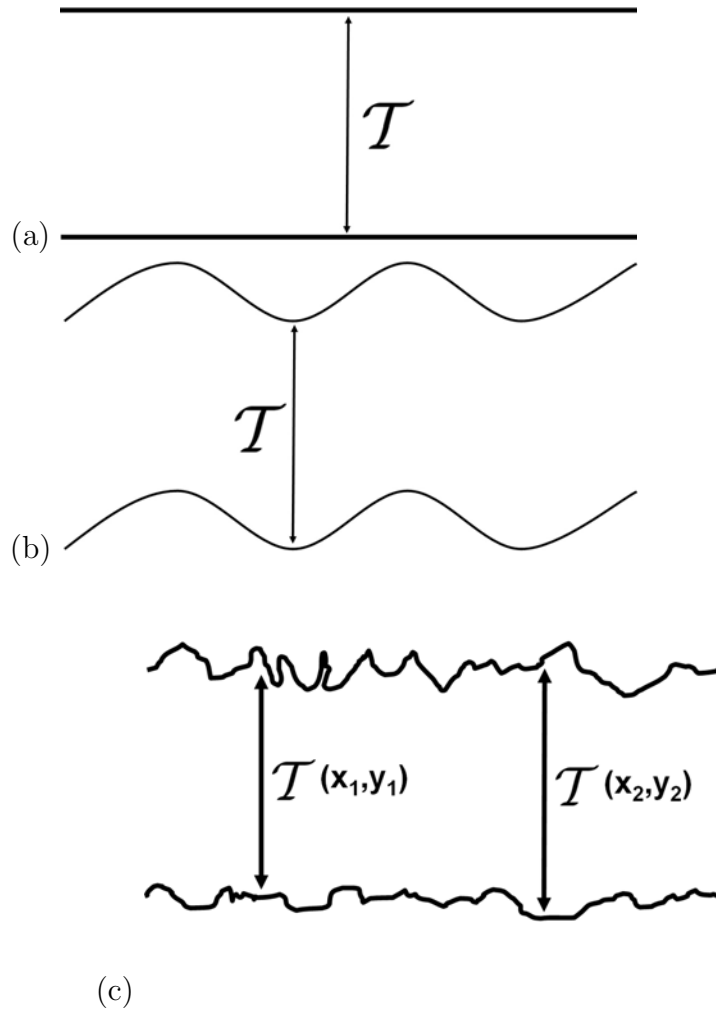
Figure 2.15: Three different models for the thickness of a 2DEG. The bottom figure (c) is the most realistic description for a δ-layer 2DEG. Geometric phase is acquired by electrons in these systems when a $\mathbf{H}_\parallel$ field is applied (*perpendicular* to the thickness direction).

an electric field, then in the "flat" sample, no additional phase is acquired, whereas in the "rippled" sample a nonzero phase *is* accumulated. If we take the parallel magnetic field $\mathbf{H} = \mathbf{H}_0$ to be in the $\hat{\mathbf{z}}$ direction, and work in the gauge $\mathbf{A} = \mathbf{H}_0 x \hat{\mathbf{y}}$, this accumulated phase $\Delta\phi$ will be proportional to $(e/\hbar)\int \mathbf{A}\cdot\mathbf{dl} \sim (eH_0\mathcal{T}^2/\hbar)$. Since $\Delta\phi$ is due entirely to the geometry of the system, the term geometric phase is indeed appropriate.

Of course, an actual δ-layer system will be quite different from these idealized examples. Rather than having a single thickness or spatial frequency which characterizes a given sample, a more realistic description requires a *distribution* of thicknesses and frequencies to be adequately specified. This is sketched in Figure 2.15 (c), where $\mathcal{T}$ is a fluctuating quantity, i.e. $\mathcal{T}$ depends on *where* in the sample plane it is measured. Representing this dependence using Cartesian coordinates, we have $\mathcal{T} = \mathcal{T}(x,y)$. Since I have suggested that the rms value of $\mathcal{T}$ is the quantity of interest in a given device, we see that in this situation an expression such as

$$< \mathcal{T} >= \left(\frac{1}{\mathcal{A}}\right) \int \mathcal{T}(x,y)dxdy \tag{2.48}$$

should be used, where $\mathcal{A}$ is the total area of the device.

To account for how the $\mathcal{T}(x,y)$ distribution influences $\delta\sigma(\mathbf{H})$, I introduce an extremely useful construct which captures the essential statistical information. I define the "thickness autocorrelation function", $C_\mathcal{T}(\mathbf{r})$ as follows:

$$C_\mathcal{T}(\mathbf{r}) =< \mathcal{T}(0)\mathcal{T}(\mathbf{r}) > . \tag{2.49}$$

The bracket $< \cdot >$ implies "averaging over all values of the origin", and $\mathbf{r}$ represents the distance from the origin to the point of interest. In other words,

equation (2.49) quantifies the *average correlation* between the thickness at an arbitrary point in the sample (taken to be the origin) with all other points a planar distance $|\mathbf{r}|$ away. Using the *Wiener-Khintchine theorem*, this can be shown to be equivalent to the following expression:

$$C_{\mathcal{T}}(\mathbf{r}) = \int_{-\infty}^{\infty} T^2(\mathbf{r})e^{i\mathbf{k}\cdot\mathbf{r}}d\mathbf{k} \tag{2.50}$$

i.e. $C_{\mathcal{T}}(\mathbf{r})$ is the Fourier transform of the absolute square of $\mathcal{T}$. Atomic force microscope (AFM) images of surfaces have established that $C_{\mathcal{T}}(\mathbf{r})$ takes the following form for random Gaussian surfaces:

$$C_{\mathcal{T}}(\mathbf{r}) = \sigma_{\infty}^2 e^{-(r/\ell_c)^{2\mathcal{H}}} \tag{2.51}$$

Where σ_{∞} is the rms surface roughness, ℓ_c the *correlation length*, and $\mathcal{H}$ the so-called "scaling exponent" (usually $\mathcal{H} \simeq 1$). Although such a surface model is probably of limited utility in δ-layer physics, we can nonetheless identify ℓ_c as the appropriate statistical quantity for taking into account how the "roughness" of the δ-layer influences the magnetoresistance.

A precise estimate of the δ-layer thickness will depend on the relationship between ℓ_e, ℓ_ϕ, and ℓ_c. For example, as discussed in [62], if the inequality $\ell_c \ll \ell_e \ll \ell_\phi$ holds, the situation is analogous to "homogeneous broadening" in nuclear magnetic resonance, and the weak localization line shape ($\sigma(\mathbf{H})$) is unaltered, as sketched in Figure 2.16 (a). In the "inhomogeneous broadening" limit (Figure 2.16 (b)), $\ell_e \ll \ell_\phi \ll \ell_c$, and the line shape *is* altered, showing a change of sign from the ideal line shape (zero roughness limit) as a function of $\mathbf{H}_\perp$. I apologize for my lack of artistry in crafting this figure.
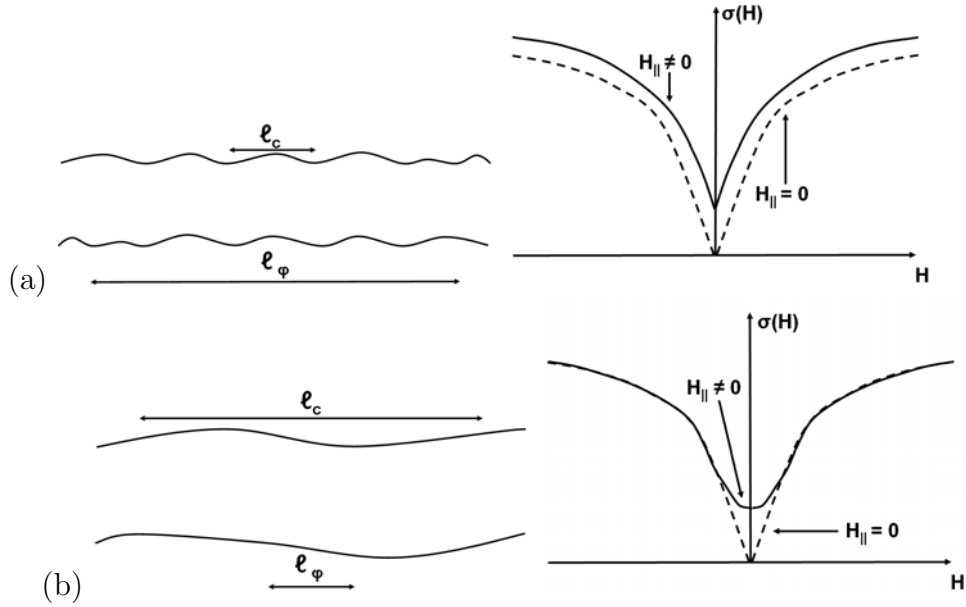
Figure 2.16: NMR analogy for parallel field weak localization measurements based on the length scales (ℓ_c, ℓ_e, ℓ_ϕ) characterizing the δ-layer. The dashed curves represent $\sigma(\mathbf{H})$ for *zero* parallel field, while the solid curves represent a finite (and constant) parallel field. The "homogeneous broadening" limit corresponds to (a), applicable when $\ell_c \ll \ell_e \ll \ell_\phi$. The "inhomogeneous broadening" limit corresponds to (b), and is applicable when $\ell_e \ll \ell_\phi \ll \ell_c$. Previous measurements, not reported in this thesis, suggest that the samples studied here are homogeneously broadened.

I will consider only two models for ℓ_c in this thesis. In the first case, I completely ignore any effects of ℓ_c on $\sigma(\mathbf{H})$, and estimate an "uncorrelated" thickness, $\mathcal{T}$:

$$\mathcal{T} = \frac{\hbar\sqrt{\gamma}}{2e\ell_\phi}. \tag{2.52}$$

This corresponds to the cross section argument presented earlier.

In the second case, I will assume homogeneous broadening of the line shape ($\ell_c \ll \ell_e \ll \ell_\phi$), and estimate a "correlated" thickness, $\mathcal{T}_c$:

$$\mathcal{T}_c = \left(\frac{1}{4\pi}\right)^{1/4}\left[\left(\frac{\hbar}{e\ell_\phi}\right)^2\left(\frac{\ell_e\gamma}{\ell_c}\right)\right]^{1/2} \tag{2.53}$$

Since independently measuring ℓ_c is presently impossible (due to the fact that the δ-layer lies beneath the device surface), all estimates of $\mathcal{T}$ in this dissertation will use the uncorrelated estimate, equation (2.52). The lone exception to this will be when I discuss Si:P diffusivity measurements in Chapter 5, and model the data using (2.53), to be consistent with the published results.

Regardless of the theoretical limitations facing a given thickness model, it seems safe to assume that the devices measured in this work were homogeneously broadened. This is suggested by previous measurements, not reported in this thesis, which more closely mimicked the homogeneous broadening case of Figure 2.16 (a). In addition, for our prototypical device $\ell_e \simeq 25$ nm and $\ell_\phi \simeq 100$ nm, while AFM images on device *surfaces* have shown $\ell_c \simeq 5$ nm. Although ℓ_c of the surface and that of the δ-layer are undoubtedly distinct, the likelihood that ℓ_c of the δ-layer exceeds 100 nm seems remote.

A natural question to ask is what actually causes the fluctuations in $\mathcal{T}$? It

seems likely that this disorder stems from two sources. The first is the intrinsic roughness of Si surfaces. A perfectly flat atomic surface does not exist, and for Si in particular the quality of the surface depends heavily on the *temperature* of the substrate during growth. Because of the technological importance of Si, such surface features have been extensively studied and characterized. According to the experts who actually grow δ-doped samples, this source of disorder is likely to be *the* limiting factor to achieving monolayer δ-doped samples, once other, less intrinsic issues, are overcome (assuming they can be).

The second source of fluctuations in $\mathcal{T}$ is from the phenomenon of *segregation*. This will be discussed more fully in Chapter 3, but for now it suffices to define segregation as the tendency of donors to migrate towards the sample surface during epitaxial growth. In other words, the donors do *not* remain on the surface where they were deposited, which leads to a broadening of the δ-layer. This tendency is much more pronounced in Si:P than in Si:B, and has recently been a subject of considerable interest. At the time of this writing, it is safe to say that segregation is the dominant contribution to a non-uniform $\mathcal{T}$ in Si:P δ-doped samples.

Chapter 3

Fabrication

The details of how a δ-doped wafer is constructed, and the processing methods used to fabricate devices for experimental investigation, are presented in this chapter. A comparison is drawn with the approaches implemented by other research groups, and the use of SIMS analysis in characterizing the quality of the samples is discussed. The wafers investigated in this dissertation were prepared by Dr. Philip E. Thompson, head of the Si MBE section at NRL. This work would not have been possible without his expertise, and his contribution is greatly appreciated.

3.1 δ-layer Requirements

Referring to Figure 1.1, it should be obvious that δ-layers do *not* occur in Nature: they must somehow be built. As mentioned in the Introduction, several methods of δ-layer construction have been demonstrated, including ion

implantation [9], chemical vapor deposition (CVD) [8], and molecular beam epitaxy (MBE), as in this and many other works. I shall first outline the physical characteristics all δ-layers should have.

3.1.1 General Considerations

Without question, MBE is by far the most powerful technique for growing δ-doped samples. What makes MBE so elegant is that, under suitable conditions, the lattice planes are grown *atom by atom*. This type of control is precisely what is sought in a δ-layer sample, where ideally donor placement in the c-Si lattice lies in a single lattice plane (i.e. in a monolayer). The basic idea behind MBE is straightforward. A substrate is placed in the MBE chamber to serve as the "base" for the heterostructure to be grown. Various "effusion cells" (specialized ovens) are distributed throughout the chamber, which act as sources for the different materials to be grown into the sample. The growth rate of a given material depends on the temperature of its cell, as well as the temperature of the substrate. Thus, in a loose sense, MBE is similar to the common technique of metallic evaporation. The MBE chamber is held at ultra-high vacuum (UHV), and therefore contamination by unwanted impurities is kept to a minimum.

Regardless of whether MBE or another approach is used, there are essentially only two factors which characterize the quality of a δ-doped sample. One, of course, is the thickness, $\mathcal{T}$, and the smaller is $\mathcal{T}$, the better. The other aspect is multifaceted, namely the defect density inherent in a particular method of

preparation. Obviously a sample with a lower defect density is "better", and there are many ways of quantifying this. Some examples include an asymmetry of the δ-layer (which, due to *segregation*, tends to be much worse in Si:P than Si:B), lattice defects (such as vacancies and interstitials), and impurities which "pollute" the δ-layer in a fashion other than intended. While quantifying $\mathcal{T}$ is relatively straightforward in that it reduces to a length measurement, the matter of defect specification is much more difficult. For instance, in the case of MBE grown layers, the *temperature sequence* incorporated during the various stages of device processing has a profound impact on the electrical characteristics a device will display. The details of this will be discussed in Chapter 5 with respect to how the resistivity of a device is influenced by a high temperature (850 °C) anneal.

At present, eliminating dopant segregation is a major area of research in the production of Si:P δ-layers. This phenomenon was described in Chapter 2 as the tendency of the donors to migrate toward the surface of the sample during growth, leading to a broader δ-layer. To see how other workers have addressed this issue, and to contrast their approaches with those used in the course of this research, I briefly digress to discuss the published results.

3.1.2 Previous Work

Three papers [64, 65, 66] on Si:P δ-layers are summarized here. The basic idea behind the MBE growth techniques used by *all* workers who have reported results on Si:P δ-layers, is illustrated by the "naive" MBE growth sequence shown in
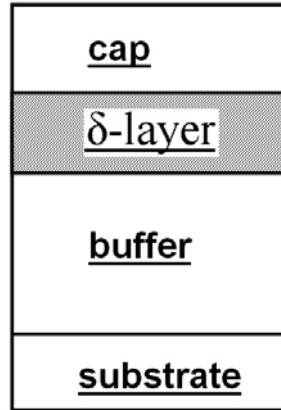
Figure 3.1: A naive approach to MBE δ-layer growth. A minimum of three steps are necessary to isolate the δ-doped region from the (100) Si substrate: 1) buffer growth (or annealing), to prepare a clean surface, 2) δ-doping, in which the donors are deposited, and 3) "cap" growth, which isolates the δ-layer and keeps unwanted impurities out of sample. Layer widths are not to scale.

Figure 3.1. In this approximation, there are only three growth steps to perform. A clean substrate of high-resistivity p-type (100) Si is used as the "base" for the rest of the heterostructure. The reason for using a p-type (100) wafer is to better isolate the n-type δ-layer from the substrate. The first step is to prepare a pristine surface for deposition of the P atoms, either by growing a so-called "buffer" layer of pure Si, or by annealing the sample at high temperatures. In the second step, δ-doping takes place by depositing P atoms (in one form or another) for a specified amount of time. This controls the doping density, n. The last step in the process is to encapsulate the δ-layer by growing pure Si (the "cap" layer) on top of the δ-doped region. This serves to isolate the P donors from the environment.

T.-C. Shen, *et al.*, at Utah State University, were the first to report results for a Si:P δ-doped wafer [64]. This work focused on the surface morphology of the sample during the various stages of growth, rather than end-result electrical characteristics. The preparation sequence employed by this group was more elaborate than the "naive" approach described above, and consisted of the following steps:

1. Start with a high-resistivity (0.1 Ω·cm) Si(100) substrate.

2. "Flash" anneal the sample at T = 1500 K to prepare the surface for P deposition.

3. Expose the substrate to a "dose" of phosphine (PH_3) gas at room temperature (RT). The P density in the δ-layer is controlled by the pressure and duration of the exposure.

4. Anneal at T = 510 K to dissociate the PH_3 and adsorb the P atoms into the substrate.

5. Deposit 0.4 nm of Si at T = 428 K.

6. Anneal at T = 773 K.

7. Deposit the cap layer, an additional 6.3 nm of Si at T = 468 K.

8. Anneal at T = 673 K.

Presumably, the annealing steps were employed to reduce the defect density in the sample. This is born out by the STM (scanning tunneling microscope) analysis

they performed of the growth stages, which showed low surface roughness and c(2x2) structures, characteristic of high-quality Si surfaces. For the two samples discussed in [64], transport measurements yielded for one sample $n = 1.3 \times 10^{14}/\mathrm{cm}^2$, with a mobility of $\mu = 13$ cm^2/V·s, while for the other sample they found $n = 8.8 \times 10^{13}/\mathrm{cm}^2$, and $\mu = 38$ cm^2/V·s. No measure of $\mathcal{T}$ in these samples was reported, nor were values for ℓ_ϕ, although they were able to observe weak localization in devices fabricated from these wafers.

A similar (and independent) approach to Si:P δ-layer construction is reported in [65], obtained by L. Oberbeck, *et al.*, at the University of New South Wales (UNSW) in Australia. For comparison with [64], I also enumerate their preparation sequence:

1. Start with a high-resistivity (~ 1 Ω·cm) Si(100) substrate.

2. "Flash" anneal the sample at T = 1150 °C for ~ 30 seconds to prepare the surface.

3. Expose the substrate to PH$_3$ at RT.

4. Anneal at T = 550 °C for 5 minutes.

5. Deposit 24 nm of Si at T = 250 °C.

These workers performed a slightly more thorough characterization of their samples by performing a SIMS (Secondary Ion Mass Spectrometry) analysis, in addition to STM and weak localization measurements. This led to identification of the annealing step after the PH$_3$ dose as *the* key element to limiting segregation.

68

Their explanation of this effect is that as the P atoms are adsorbed into the Si crystal, they become bound by *three* covalent bonds, instead of just one as when the P atom resides on the surface. Transport measurements yielded n = (2.0 +/- 0.4)x10^{14}/cm^2, and $\mu \simeq 140$ cm^2/V·s. They also observed weak localization, but did not report values for ℓ_ϕ.

The final work I shall discuss was performed by K.E.J. Goh, *et al.*, also at UNSW [66]. This is by far the most complete study on segregation in Si:P δ-doped samples reported to date. Here a systematic study of the substrate temperature on P segregation into the cap layer was performed, with different samples prepared at RT, 250, 400, and 600 °C. This paper *does* report their weak localization results, which serves as an important piece of the puzzle for optimizing δ-layers grown using phosphine. The largest value of ℓ_ϕ (and therefore the "best" from a quantum transport perspective) was obtained for the sample whose cap layer was grown at T = 250 °C, and for this sample the corresponding device parameters were determined to be $\mu \sim 61$ cm^2/V·s, n = 1.64x10^{14}/cm^2, and $\ell_\phi = 72$ nm. Their transport measurements were performed at T = 4.2 K.

Since the research in [65, 66] relied heavily on the use of SIMS to assess the quality of their process, a brief discussion of that technique is in order.

SIMS

SIMS is a very powerful technique for acquiring profiles of elemental concentrations versus depth in a given material sample. An example of a SIMS profile from an Si:P δ-doped sample is shown in Figure 3.2. The way such a profile

is obtained is to bombard the sample with a high-energy ($\sim$ keV) primary ion beam, which sputters matter away and leaves a "crater" behind. The ejected material consists of both neutral atoms and secondary ions. The secondary ions are separated from the other matter electrostatically, then directed into a mass spectrometer tuned to detect the particular elemental mass of interest. The primary beam is rastered in order to create a flat-bottomed crater, but the ions are acquired only from the center of this crater, which ensures that each data point comes from a unique depth. The intensity of the secondary ion signal is proportional to the ion concentration at a given depth, whose scale is quantified by the use of reference samples and surface profilometer measurements. By correlating the crater depth with the secondary ion intensity, the desired depth profile is constructed. It is also worth noting that SIMS can distinguish the signals between different *isotopes* of a given element, which has been used to explain the large surface signal in Figure 3.2. According to [65, 66], this signal is due not to P (with atomic number Z = 15), but to "false counts" induced by the simultaneous detection of Si (Z = 14) and H (Z =1).

The detailed procedures incorporated in a given SIMS analysis are rather extensive, and must be optimized for the particular application involved. The doping profile shown in Figure 3.2 was performed by the analytical group at Charles Evans and Associates, and used a quadrupole SIMS instrument with Cs as the primary ions. The incident ion energy was 1 keV, and the angle of incidence was 60°. The P detection limits for this analysis were $4x10^{15}/cm^3$. The "straggle" of the doping distribution toward the surface is a clear manifestation of
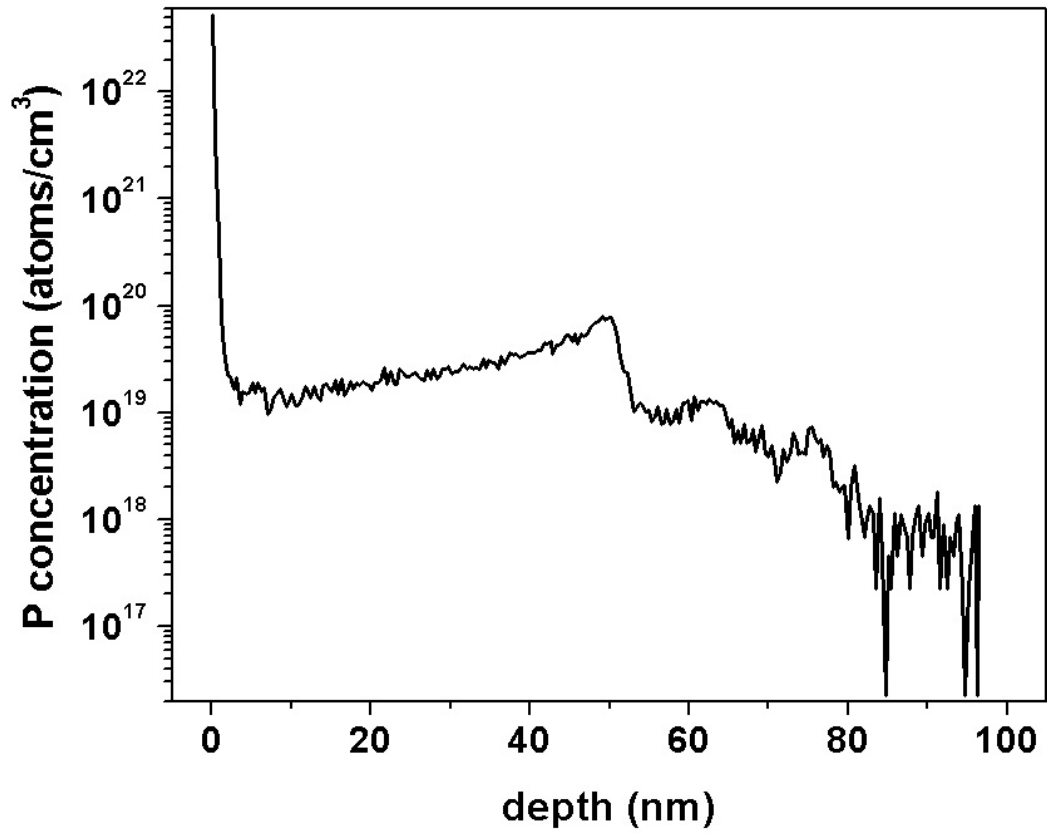
Figure 3.2: SIMS data for a Si:P δ-doped sample, with a large amount of segregation apparent (the region between 10 and 50 nm). The signal peak at the surface of the sample is likely due to Si and H (total protons = 14 + 1 = 15) "masquerading" as P (15 protons) [65, 66].

segregation.

Although this SIMS analysis has yielded a detailed cross section of the doping profile in the sample, several limitations of this technique are worth pointing out. First, $\mathcal{T}$ at only one point in the crystal is sampled, and examining many areas would require a substantial amount of time (and money). Second, the technique is *destructive*. By boring a crater in the sample through ionic bombardment, the P atoms in the δ-layer are to some extent forced further into the crystal. This often manifests itself in the profile appearing steeper near the surface of the sample than on the "backside", and thus leads to an erroneous estimate of $\mathcal{T}$. Third, little to no information in regard to electrical characteristics or defect densities can be inferred from SIMS. Fourth, and perhaps most importantly, the spatial resolution of SIMS is limited. Determining the precise resolution limits of SIMS for Si:P δ-layers is presently an unresolved question, but it is safe to say that sub-monolayer resolution is *not* possible using SIMS. In contrast, weak localization measurements for determining $\mathcal{T}$ suffer from none of these limitations. Chapter 5 will explore this more fully.

3.2 δ-doped Wafer Preparation

With the necessary background in place, I now discuss the preparation sequence for the δ-doped wafers used in this work. I shall first comment on some particular aspects of our approach.

First, the primary difference between the samples used here versus those of

| cap |
| δ-layer |
| buffer 3 |
| buffer 2 |
| buffer 1 |
| substrate |
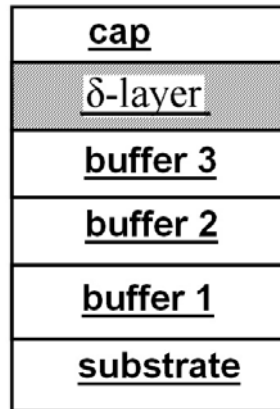
Figure 3.3: "Old" δ-doping technique. In an effort to minimize P segregation, a sequence of buffer layers are incorporated in the growth as the substrate temperature is reduced. Buffer 1 corresponds to 170 nm of Si grown at T = 650 °C, buffer 2 to 18 nm of Si grown as T was reduced to 400 °C, and buffer 3 to 12 nm of Si with T held at 400 °C. The δ-layer and cap layer (50 nm of Si) were grown with T = 400 °C. No trap layer was implemented, and the layer thicknesses are not to scale.

[64, 65, 66] is that the P was obtained through thermal decomposition ("burning") of GaP. The Ga was separated from the P by passing the GaP "fumes" through a B filter, apparently producing a very pure P source. Second, the substrates were always high-resistivity p-type Si(100) wafers. As mentioned earlier, a p-type substrate more effectively isolates the n-type δ-layer from the rest of the sample, but more importantly, a δ-layer in Si can *only* be grown along the (100) lattice direction [63]. Finally, typical vacuum levels during growth were $\sim 5 \times 10^{-9}$ Torr, and the wafers were rotated at $\sim$30 rpm during growth to promote a uniform doping density across the wafer.

An actual growth sequence for a δ-doped sample is depicted in Figure 3.3. The major difference between this recipe and the "naive" one described earlier is the *temperature sequence* the substrate is taken through in the course of growth. After placing the substrate in the MBE chamber, the wafer's temperature is raised to T = 650 °C and a 170 nm buffer layer of pure Si is grown. Next, the substrate temperature was reduced to T = 400 °C over the course of 3 minutes, then held at T = 400 °C for the remainder of the growth process. The total Si growth during the time the sample has its temperature reduced and stabilized is $\sim$ 30 nm (a constant Si growth rate of $\sim$ 0.1 (nm/s) is assumed). At this point the P δ-layer itself is grown by opening the shutter to the P source for 200 seconds, which produces a doping density of $\sim 10^{14}$ P atoms/cm^2. The heterostructure is completed by growing a 50 nm cap layer with the substrate temperature held at T = 400 °C. The SIMS analysis for the δ-layer produced by this process was shown in Figure 3.2. The most obvious feature of this plot is that the δ-layer itself is not
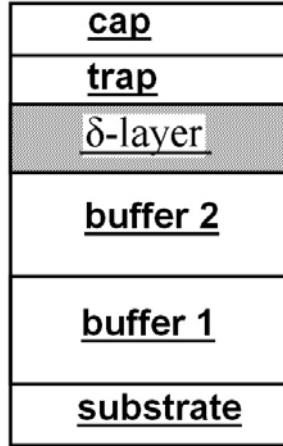
Figure 3.4: Growth sequence of δ-doped sample incorporating both substrate cooling and an Si trap layer. This technique produces the sharpest δ-profiles observed in this work. Buffer 1 corresponds to 150 nm of Si grown at T = 650 °C, and buffer 2 to 18 nm of Si grown as T was reduced to 320°C. The δ-layer and 4 nm "trap layer" were grown with T = 320°C, while the 50 nm cap layer was grown at T = 500 °C. All magnetoconductance data presented in this thesis were taken on samples using this type of growth sequence. Layer thicknesses are again not to scale.

very sharp, but rather displays a skewness or "straggle" towards the surface. This *is* segregation, and is especially pronounced in Si:P. The low growth temperature used (400 °C) was intended to minimize this segregation, but clearly was not entirely effective.

The best growth technique used in this work is shown in Figure 3.4. Two buffer layers are grown to isolate the δ-layer from the substrate, the first being a layer 150 nm thick grown at T = 650 °C, the second a 18 nm layer grown as the

substrate temperature was reduced from 650 °C to 320°C over the course of three minutes. The δ-layer was then grown at 320°C by opening the P shutter for 200 seconds. The next step is the most crucial part of the entire process: 4 nm of undoped Si were grown on top of the delta-layer at 320°C in an effort to "trap" the P donors to a narrower region than had been obtained by the methods of Figure 3.3. Incorporating this step was motivated by [65]. All growth (Si and P) was then stopped, and the substrate temperature was raised from 320 °C to 500°C over a 3 minute interval. Finally, a 50 nm cap layer was grown to complete the process. A SIMS analysis from a sample of this wafer is shown in Figure 3.5.

Clearly something rather dramatic has occurred. Whereas when using the "old" growth method the sample showed a great deal of segregation, the "new" sample shows almost none. In addition, the doping profile is much more symmetric about its maximum doping density level, and in general appears to be much more "δ-like". These are two very significant improvements to the quality of the δ-doping profile, and can be traced back to the implementation of the trap layer in the growth sequence. A heuristic explanation for this effect goes somewhat as follows. Since segregation is more pronounced at higher temperatures, it is desirable to grow the δ-layer at as a low a temperature as possible. Unfortunately, the growth of $high-quality$ c-Si has just the opposite temperature dependence: the higher the Si growth temperature, the fewer intrinsic lattice defects (vacancies and interstitials) are produced [20]. It is also well-known that diffusion is enhanced by the presence of such defects in the crystal [85]. Thus we see that growing Si at a higher temperature will reduce the intrinsic diffusivity of P in Si, and

76
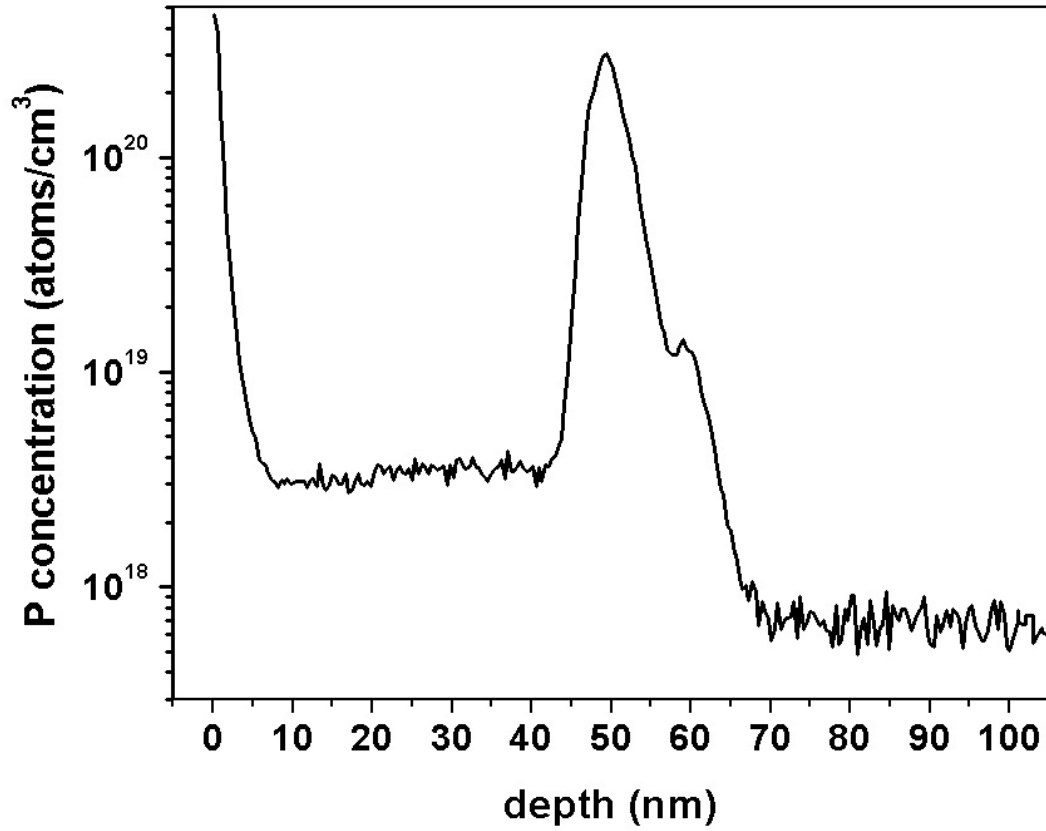
Figure 3.5: SIMS analysis of a δ-doped wafer grown *with* the 4 nm thick trap layer. A much narrower and more symmetric "δ-like" profile is obtained, showing the importance of the trap layer for Si:P δ-layer growth.

consequently will help to produce a narrower δ-layer because the P diffuses less in the c-Si lattice. These two opposing requirements are balanced by the trap layer. By growing a narrow (~ 4 nm) Si trap layer on top of the δ-doped region and *then* heating the substrate, the P donors do segregate to the surface, but no farther: they are bound to this region. Thus the name "trap layer" is highly suggestive of its function in that it limits the P segregation to a well-defined portion of the crystal. The cap layer can then be grown at a higher temperature (T = 500°C) without being overly concerned with P segregation. It should also be mentioned that a sample with a lower defect density generally has a higher electronic mobility, which is often desirable in nanostructure devices.

This insight presents interested researchers with a wide range of potential avenues for investigation. For example, does the δ-layer width correlate strongly with the trap layer width? That is, if the trap layer were grown to be only 1, 2 or 3 nm thick, would this correspondingly produce a narrower δ-profile? Another interesting question is precisely what temperatures and growth rates *optimize* the process? In other words, can true Dirac-delta (*monolayer*) doping profiles be achieved in Si:P using MBE? The available parameter space to be explored is enormous, and will not be discussed further here. Instead, we shall content ourselves to simply note that very sharp, δ-like doping distributions can indeed be achieved in MBE grown Si:P δ-layers, provided that a trap layer is incorporated in the growth process. For reference, a step-by-step algorithm to grow a high-quality δ-layer is included below.

1. Clean p-type Si(100) substrate (includes NRL clean and 2.5% HF dip to remove native oxide) and place in MBE chamber.

2. Increase substrate temperature to T = 650 °C for buffer layer growth.

3. Buffer layer growth: $\sim$ 150 nm grown at T = 650 °C. Si growth rate is $\sim$ 0.1 nm/s.

4. Reduce substrate temperature to T = 320 °C over three minutes for δ-layer growth. Total Si growth in this interval is $\sim$ 18 nm.

5. Grow δ-layer with substrate temperature at T = 320 °C. A 200 second exposure to the P source produces a doping density of $\sim 10^{14}/\text{cm}^2$.

6. Trap layer growth: 4 nm of Si grown at T = 320 °C.

7. No growth of either Si or P as substrate temperature is increased from T = 320 °C to T = 500 °C over three minutes.

8. Cap layer growth: 50 nm of Si grown with T = 500 °C.

Once a δ-doped wafer has been prepared as described, the next step in the experimental investigation is to prepare mesoscopic devices for measurement. This fabrication process will now be described.

3.3 Device Fabrication

One of the primary goals of the fabrication process is to keep the sample as free from contaminants as possible. Therefore, a substantial number of the

processing steps are devoted to "cleaning" the device. In addition, the samples are inspected optically throughout the process to be sure that nothing obvious has gone awry. Even if things "look" fine with the device (i.e. no defects are apparent), the only meaningful check is actual electronic testing. Such testing will be discussed at the end of this chapter.

Before any processing is done to a sample of the δ-doped wafer, it is advisable to simply check whether a piece of it conducts at low (liquid helium) temperatures. This is done by "scribing" a small piece off of the wafer, placing 4 In solder "blobs" on the edges of the chip, connecting Au wires to the blobs, attaching the chip to a DIP (dual inline pin) header, and dipping the sample in liquid helium. If the sample displays a low *two-terminal* resistance (R $\leq$ 10 kΩ) between any two contacts, then the enumerated procedure described below can be followed to make an actual device. If this test does not work, i.e. the two-terminal resistances are very high (R $\geq$ 1 MΩ), then obtaining a new sample is in order, rather than going through the laborious process of fabrication only to find, in the end, that the device does not work!

Here, then, is a step-by-step algorithm for producing a Hall bar device suitable for measurement.

1. Soak wafer in concentrated HCl to remove any residual "scum" from previous handling ($\geq$ 2 hours).

2. Dice wafer into approximately 5 mm x 5 mm pieces for use in actual device fabrication. The DIP header on which completed devices were mounted has

a width of $\sim$7 mm, therefore the dies used must be smaller than this.

3. Non-chlorinated (NC) solvent clean. In order, the chip is sprayed with acetone, methanol, and isopropanol alcohols, then "blow-dried" with N_2 gas.

4. Spin on resist. Typically Futurrex NR7 1500 P *negative* resist was used. The resist was spun at 5000 rpm for 1 minute.

5. Bake sample in oven at T = 120 °C for 1 minute to perform initial "cure" of resist.

6. Perform electron beam lithography using the scanning electron microscope (SEM) on the resist to define a device pattern. The reason e-beam lithography was used is twofold. For one, it is very easy to make changes to a given pattern or design entirely new devices by using the NPGS software which controls the SEM. Photomasks lack this flexibility. Second, by using the SEM, annoying issues associated with photomasks are avoided, such as proper contact between the sample and mask or the sample sticking to the mask. In a nutshell, the use of e-beam lithography makes the fabrication process more reliable. For reference, a typical exposure dose was ~ 10 $\mu C/cm^2$.

7. Post-bake sample in oven at T = 120 °C for 1 minute for final "cure" of resist.

8. Develop resist in appropriate solvent (RD6 for Futurrex negative resists).

9. Dip in de-ionized (DI) water to remove solvent from exposed sample surface.

10. Etch device pattern into δ-doped sample using RIE (Reactive Ion Etch). An SF$_6$ plasma was used to etch the Si 20-30 nm *below* the δ-layer in order to expose an edge of the doping plane for subsequent electrical contact. A "mesa" structure results from this etch (see Figures 3.6 and 3.7).

11. Clean resist from sample by soaking in a "piranha" bath $\sim$30 minutes. The piranha bath consists of a mixture of H$_2$S0$_4$ and H$_2$O$_2$ in a 3:1 ratio.

12. Measure the mesa profile to ascertain how much Si the SF$_6$ etch removed. The δ-layer should nominally lie somewhere near the middle of the "wall" profile of the mesa. For example, if the chip were from the same wafer as the SIMS analysis of Figure 3.5, the wall should have a height of at least 60-75 nm.

13. Perform 0$_2$ plasma clean ("descum") in RIE to further remove residual resist (and possibly other) contaminants.

14. Dip sample in concentrated HF solution to remove the SiO$_2$ produced by the O$_2$ plasma of the previous step.

15. Clean "polymer scum" (CF$_x$, Si-C, Si-F, etc.) off of sample surface left as a result of the SF$_6$ etch. This is done by placing the sample in a bath of the "barracuda" clean, a mixture of NH$_4$OH, H$_2$0$_2$, and H$_2$0 in the ratio 1:1:5 for $\sim$ 30 minutes [67]. This barracuda cleaning step is crucial, since the polymer scum otherwise causes contacts to the δ-layer to become insulating at low temperatures, making electrical measurements impossible.

16. Dip sample in DI water, and perform NC solvent clean.

17. Spin and bake resist for second layer of lithography as in steps 4 & 5.

18. Perform optical lithography to define "δ-contact" pads (see Figure 3.7). The resist exposure is done with a photomask and ultraviolet light on a contact aligner.

19. Post-bake and develop resist as in steps 7 & 8.

20. Dip sample in HF:H_2O (1:100) solution to remove any oxide which has accumulated at the surface of the δ-layer.

21. Perform first metalization. In a thermal evaporator, deposit $\sim$ 2.5 nm of Cr, then enough of the Au-Sb (99:1) alloy to exceed the mesa wall height by 10-20%. The reason Au-Sb is used is to lower the *Schottky barrier* associated with the metal-semiconductor contact.

22. "Lift-off" resist and unused Au-Sb in RR2 solvent. For this step, the RR2 has T = 100 °C, and the sample is allowed to soak for $\sim$20 minutes.

23. If the RR2 lift-off still has not removed all of the unused Au-Sb, place the sample in a beaker of DI water and subject the beaker to ultrasonic treatment for 1 minute intervals until the lift-off is complete.

24. Anneal the sample in a rapid thermal annealer (RTA) for 5 minutes at T = 450 °C. The ambient atmosphere in the RTA is a combination of N_2 and H_2 gas. The purpose of the annealing is to diffuse the Au-Sb alloy into the

δ-doped region of the sample and further lower the Schottky barrier. This step is important for establishing an Ohmic electrical connection with the δ-layer (i.e. a connection which displays a *linear* I-V curve).

25. NC solvent clean.

26. Spin and bake resist for third and final layer of lithography.

27. Perform optical lithography (including development) to define "bonding pads" which overlap with the δ-contact pads (see Figure 3.7).

28. Perform second metalization. In a thermal evaporator, deposit ~ 2.5 nm Cr and ~ 100 nm Au.

29. Lift off using RR2 as in step 22.

30. NC solvent clean.

31. Connect Au wires to bonding pads with a wire bonder.

32. Fasten sample to DIP header using either GE varnish or vacuum grease.

33. Use silver paint to finally connect Au wires to DIP header contacts. The reason for using Ag paint is that the header pins cannot be directly wire bonded to, and the use of a solder such as In generally causes magnetic shielding due to the Meissner effect (to be discussed more fully in Chapter 4).

Generally speaking, this process yields high quality devices for measurement. Figures 3.6 and 3.7 show the evolution of the sample from
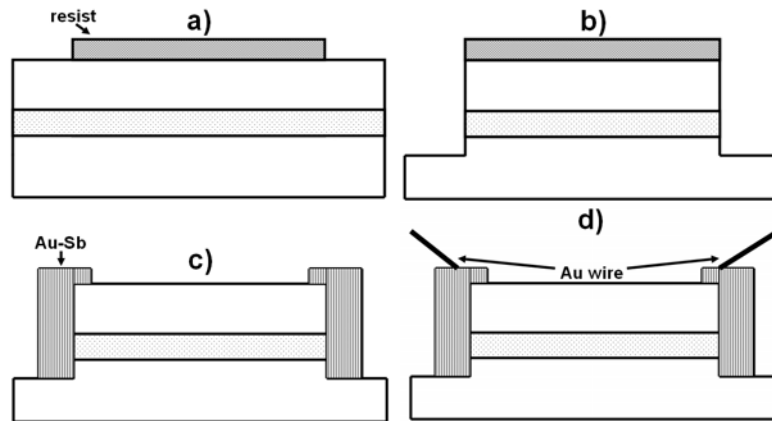
Figure 3.6: A "horizontal profile" of the device fabrication process flow. In a), the device's dimensions are defined by electron beam lithography. In b) the device pattern is etched into the δ-doped Si with an SF_6 etch. Electrical contacts are made via 2 metalizations as in c), and finally wires bonded are to the metal in d). At this point the device is ready to be mounted on a header and tested at T = 4.2 K.
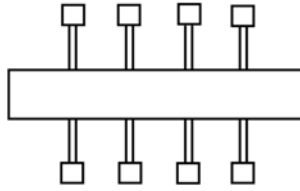
(a)
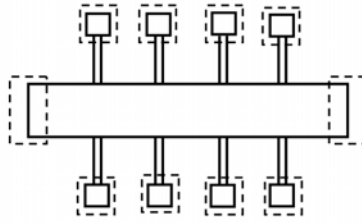
(b)
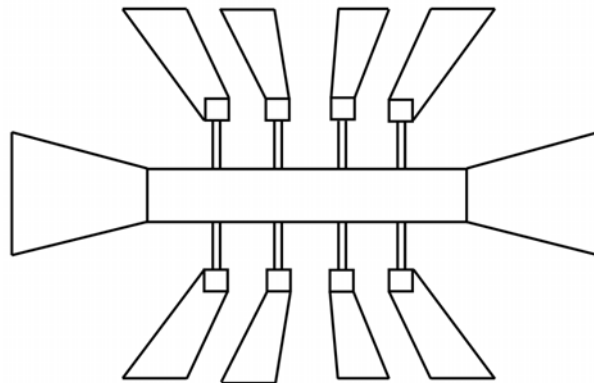
(c)

Figure 3.7: Approximate device evolution following process flow sequence of Figure 3.6. First the "mesa" is defined with electron beam lithography and a dry SF_6 etch, as in (a). Two metalizations follow to make electrical contacts with the δ-layer. The first evaporation is Au-Sb (b), for the actual "δ-contacts", the second (c) is pure

Au, which overlaps the Au-Sb contacts and provides a larger surface area ($\sim$ 250 μm x 250 μm) for wire bonding.

horizontal and vertical perspectives, to give the reader a visual feel for the major fabrication steps required.

3.4 Device Testing

Assuming the δ-doped wafer is suitable for use in device construction (i.e. conducts current at low temperatures, etc.), at this stage the sample could be mounted on the dilution refrigerator and cooled to base temperature for measurement. However, it is prudent to perform some final diagnostic tests to ensure that the device will behave as desired and be straightforward to measure.

The first such test is a simple "continuity" check at room temperature to verify that all probes on the sample are in fact electrically connected with one another. This is quickly and easily done with a hand-held DVM.

The second check is to "dip" the sample in a liquid helium dewar and then re-measure the contact resistances. If there are any open circuits at 4.2 K but not at room temperature, then it is necessary to evaluate what may have gone wrong in the processing to cause this. Depending on the intrinsic resistivity of the sample, the voltage probes should display a low resistance between each other, and the resistance measured between *adjacent* contacts around the sample should be very nearly equal.

The third test is to establish whether or not any conduction through the

substrate is taking place at 4.2 K. This is accomplished by the use of an ancillary contact, connected to the δ-doped device *only* through the substrate. The resistance between this "floating" contact and any probe on the sample should be infinite, or at least much higher than the resistance between any two probes on the device. Otherwise, the current in the sample is not confined to the lithographically defined device region, and resistance measurements become meaningless.

Finally, the sheet resistance (*resistivity*) can be checked with a four-wire measurement to get a rough idea of what the signals will be like at base temperature of the dilution refrigerator. This merely serves as a benchmark for the more accurate magnetoresistance measurements to be performed, which will be discussed in the next chapter.

Chapter 4

Measurement

In this chapter I will discuss how four-wire conductance measurements on δ-doped devices were performed. The necessary background is developed by discussing the conductivity tensor for two-dimensional systems, the instrumentation used in making the measurements, the particular techniques employed for obtaining data, and the systematic errors involved in these experiments.

4.1 Background

A proper 4-wire measurement [68] of a resistance R_s is depicted in Figure 4.1 (a). The device is biased with a known current I using one pair of wires, and the voltage V induced by the current is measured with a second pair of wires. R_s is given by Ohm's law, i.e. by forming the ratio $R_s = V/I$.

Typically the current source is realized by placing a large, known resistance R_L in front of a known voltage source V_0. The much smaller resistance of R_s is then placed in series with this arrangement, as shown in Figure 4.1 (b). Since R_L dominates the circuit impedance ($R_L \gg R_s$), the current I is effectively given by $I = V_0/R_L$. Voltage measurements across R_s are generally made using the combination of a differential preamplifier and a digital voltage meter (DVM). This high input impedance arrangement limits "shunting" of current from the device, which would otherwise corrupt the measurement. Obviously, the more accurately V and I are known, the better the measurement.

As straightforward as this 4-wire technique is, it is also incredibly powerful. Since the resistance of a device depends on numerous parameters of physical interest, such measurements can be used to extract useful information about a particular electronic system. For example, the conductance measurements on δ-doped devices discussed in this thesis depend on "external" variables such as the sample dimensions, temperature T, magnetic field $\mathbf{H}$, current density $\mathbf{J}$, and applied electric field $\mathbf{E}$, as well as the frequency of these fields, ω_i. Quantities "internal" to the δ-layer, such as the carrier density n, mean free path ℓ_e, dephasing length ℓ_ϕ, effective mass m*, and, of course, the δ-layer thickness $\mathcal{T}$, can be deduced through the application of appropriate theoretical models to properly carried out resistance measurements. It should also be noted that *resistivity* (ρ) refers
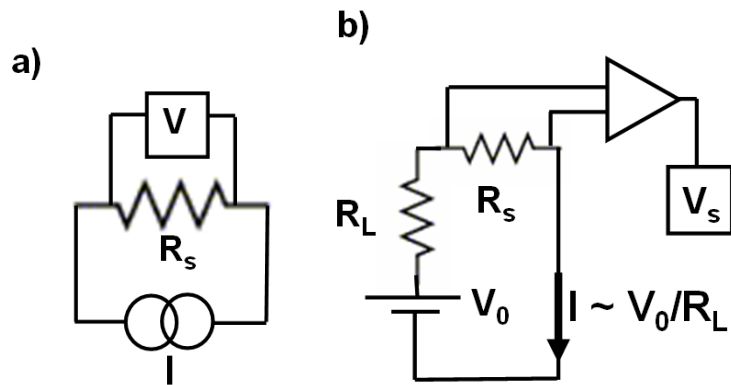
Figure 4.1: 4-wire measurement schematic. In (a), a current bias, I, is passed through the device, and a voltage V is measured. (b) shows a practical realization of this, which incorporates a voltage source V_0 in series with a large resistance R_L to serve as the current source. The resistance of the sample, R_s, is deduced by measuring the voltage V_s across the sample with a differential preamplifier and DVM, then forming the ratio $R_s = V_s/I$.

to the *intrinsic* electrical characteristics of the material system under study. Given ρ and the geometry of a given device, one should be able to predict what *resistances* will be measured under a given set of conditions. I shall discuss this in more detail later.

An elaborate theory of conductance measurements and their symmetry properties has been developed over time. We cannot go into this in any detail here, but merely cite a few results pertinent to this thesis. Since this work concerns magnetoconductance measurements of c-Si, Onsager's result [69] that the *local* resistivity tensor of a cubic crystal obeys the symmetry relation $\rho_{ij}(\mathbf{H}) = \rho_{ji}(\text{-}\mathbf{H})$ suggests that an analogous (though not identical) expression should hold here. Landauer's many contributions to the modern understanding of conduction processes include quantifying how local variations of $\mathbf{E}$ in the conductor due to scatterers influence transport [70], modeling conduction using the basic quantum mechanical notions of reflection (R) and transmission (T) coefficients, and generalizing these notions to real, multichannel conductors [71]. van der Pauw's result [72], showing that the resistivity of an *arbitrarily* shaped conductor could be found through a conformal mapping, further established the power of 4-wire measurements, and will be used extensively in Chapter 5. Finally, Büttiker's reciprocity theorem [73] regarding 4-wire measurements in the presence of a magnetic field $\mathbf{H}$ leads to the *global* symmetry relation $\mathrm{R}_{ij,kl}(\mathbf{H}) = \mathrm{R}_{kl,ij}(\text{-}\mathbf{H})$. In this expression, the first pair of indices refers to the current

leads, the second to the voltage leads. Thus a perfect conduction symmetry is observed in a device under magnetic field reversal, if, in addition, the current and voltage leads are also exchanged with one another. I shall discuss this further in Chapter 5 as well.

4.2   The Two-Dimensional Conductivity Tensor

Since the electron system associated with a δ-layer is inherently two-dimensional, in general a *tensorial* relationship will exist between the electric field $\mathbf{E}$ (related to the measured voltage V by V = -$\int \mathbf{E} \cdot \mathbf{dl}$) and the current density $\mathbf{J}$ in such a device. It is immediately apparent that the units of $\mathbf{J}$ in two dimensions are (amperes/meter) instead of the usual (amperes/meter^2), as it is for three-dimensional conductors. I shall elaborate on this shortly.

In this work, R = V/I is a function of both magnetic field $\mathbf{H}$ and temperature T:

$$R(\mathbf{H}, T) = \frac{V(\mathbf{H}, T)}{I(\mathbf{H}, T)}. \qquad (4.1)$$

Such an expression makes the use of the term *magnetoresistance* obvious, and is really the "scalar" version of the aforementioned tensorial relation. In order for this expression to be meaningful, a *linear response* must be observed between $\mathbf{E}$ and $\mathbf{J}$, and therefore a more precise definition would be

R = dV/dI. This linear dependence was observed in all of the samples discussed here.

Depending on the causal point of view one wishes to take, one can consider either the resistivity ρ or the conductivity σ. In the first case the application of **E** "causes" **J** to flow in the device, and Ohm's law takes the form

$$\mathbf{J} = \sigma \mathbf{E}. \tag{4.2}$$

One can also take the "inverse" approach, and write

$$\mathbf{E} = \rho \mathbf{J}. \tag{4.3}$$

Accordingly, $\sigma \rho = \mathbf{1}$, where $\mathbf{1}$ is the 2x2 identity matrix.

For a Cartesian two-dimensional system, equation (4.3) is expressed in matrix notation as:

$$\begin{pmatrix} E_x \\ E_y \end{pmatrix} = \begin{pmatrix} \rho_{xx}(\mathbf{H}, T) & \rho_{xy}(\mathbf{H}, T) \\ \rho_{yx}(\mathbf{H}, T) & \rho_{yy}(\mathbf{H}, T) \end{pmatrix} \begin{pmatrix} J_x \\ J_y \end{pmatrix}. \tag{4.4}$$

This can be further simplified for the devices investigated here, since not all of the components ρ_{ij} were found to be independent. The diagonal elements, ρ_{xx} and ρ_{yy} equal one another: $\rho_{xx} = \rho_{yy} \equiv \rho$. This is easily understood due to the fact that the samples were fabricated from (100) Si, and all <100> directions in Si are equivalent [20]. Furthermore, the off-diagonal components were found to be *antisymmetric*: $\rho_{xy} = \text{-}\rho_{yx}$. This is also easy to interpret, by considering how the Lorentz force ($\mathbf{F} = q\mathbf{v} \times \mathbf{H}$) acts on a charge q moving with velocity **v**. If we assume q > 0 and motion along the

$+\hat{\mathbf{x}}$ direction, the Lorentz force deflects q towards $-\hat{\mathbf{y}}$, in effect experiencing an *effective* electric field in that direction. On the other hand, for motion along $+\hat{\mathbf{y}}$, the deflection (and corresponding effective electric field) is in the $+\hat{\mathbf{x}}$ direction. Thus I arrive at the final form of the resistivity tensor for δ-doped silicon:

$$
\begin{pmatrix} E_x \\ E_y \end{pmatrix} = \begin{pmatrix} \rho_{xx}(\mathbf{H}, T) & \rho_{xy}(\mathbf{H}, T) \\ -\rho_{xy}(\mathbf{H}, T) & \rho_{xx}(\mathbf{H}, T) \end{pmatrix} \begin{pmatrix} J_x \\ J_y \end{pmatrix}.
\tag{4.5}
$$

Thus there are only *two* independent components of the resistivity (conductivity) tensor for δ-layers in Si.

4.2.1 Hall Bar Devices

To see how these notions apply to actual device geometries, consider Figure 4.2, which shows a schematic of a typical Hall bar device constructed for use in δ-layer transport studies. The "current channel" has a width W, and the voltage contacts are spaced a distance L apart. There are essentially only two independent resistance measurements one can perform on such a device. One is the "longitudinal" resistance, when the induced voltage V_{WL} (for "weak localization voltage") is measured between two adjacent contacts on the same side of the device (i.e. *parallel* to the current bias). The other is the "transverse" resistance where the induced voltage V_H ("Hall voltage") is measured between contacts directly across the sample from one another (*perpendicular* to the current bias). Other resistances on the sample will be
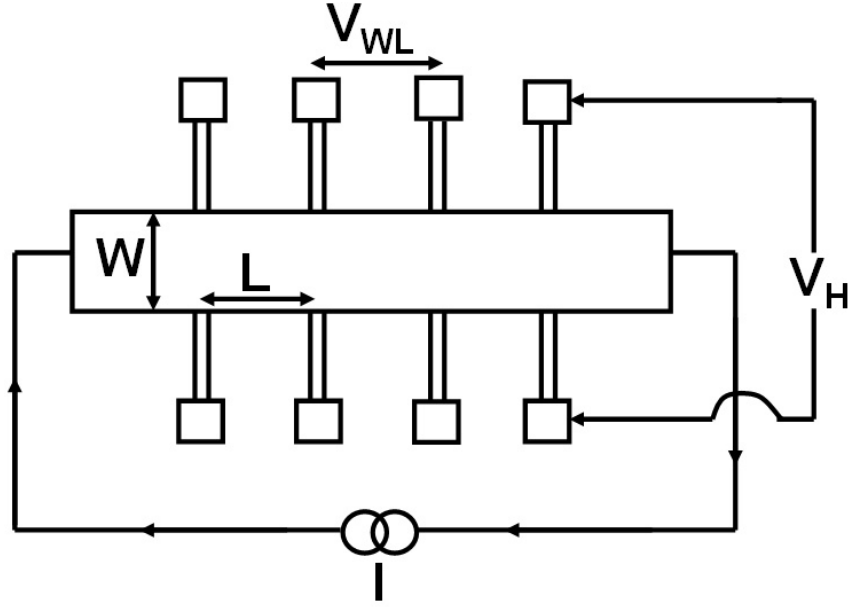
Figure 4.2: Hall bar measurement schematic. A current bias, I, is passed through the device, and two voltages are measured, as discussed in the text. The weak localization voltage, V_{WL}, is measured *parallel* to I, the Hall voltage, V_H, *perpendicular* to I. When the voltage contact spacing, L, is equal to the sample's width, W, the measured longitudinal resistance is the device's intrinsic *resistivity* in units of $\Omega/\square$.

linear combinations of these "basis" measurements.

It should be clear from the figure that V_{WL} scales like $V_{WL} \sim (L/W)I$, whereas V_H is independent of L and W (see Appendix A for a derivation). Thus the significant resistances of the device given a *rectangular* geometry are $R_{WL} = (W/L)(V_{WL}/I)$, and $R_H = V_H/I$. If the current channel width W equals the voltage contact spacing L, $W/L = 1$, and the measured longitudinal resistance is *by definition* the two-dimensional resistivity: R_{WL}

$= \rho$. This two-dimensional ρ is often referred to as the sheet resistivity, symbolized by $R_\square$, and has dimensions of $\Omega/\square$ ("ohms per square"), as opposed to $\Omega\cdot$cm for three dimensional samples. The set of equalities $R_{WL} = \rho = R_\square$ will be used interchangeably throughout the remainder of this dissertation. Given this two-dimensional definition of resistivity, we now see that in order to be dimensionally consistent, the current density $\mathbf{J}$ must have units of (amperes/meter), as mentioned earlier.

4.2.2 van der Pauw Devices

Not all of the samples fabricated in the course of this work used the rectangular geometry of Figure 4.2. Such devices, with arbitrary geometries, are collectively referred to as *van der Pauw devices*. A general van der Pauw sample is shown in Figure 4.3, and is simply a device with 4 contacts (labeled A, B, C, D) placed on its *perimeter*. Given a device with such an arbitrary geometry, it is clear that if a current is passed between any two electrodes, the current density will be non-uniform throughout the sample. This is very different from a Hall bar, and given such non-uniformity, one might at first assume that being able to determine the samples conductivity tensor would be a difficult task. Fortunately, this is not the case, and a *conformal mapping* exists which translates the resistances measured on these arbitrarily shaped samples to that of ρ_{xx} and ρ_{xy} as measured on the standard Hall bar device of Figure 4.2. This result, mentioned earlier, was established by L.J. van der
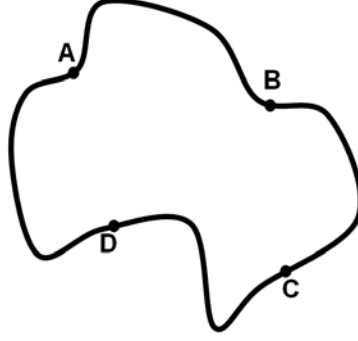
Figure 4.3: Arbitrarily shaped van der Pauw device. The electrodes A, B, C, D must be placed on the devices perimeter to apply van der Pauw's theorem.

Pauw in 1958 [72], and has proved extremely useful in this work.

To extract ρ from such a sample such as the one shown in Figure 4.3 one must measure *two* appropriate resistances, labeled $R_{AB,CD}$ and $R_{AD,BC}$, then numerically solve the following equation for ρ:

$$exp(\frac{-\pi R_{AB,CD}}{\rho}) + exp(\frac{-\pi R_{AD,BC}}{\rho}) = 1. \tag{4.6}$$

The notation here is such that $R_{AB,CD}$ refers to a resistance measurement where current is sourced and drained in leads A and B, while voltage is measured between contacts C and D (similarly for $R_{AD,BC}$). The key point is that if one is interested in measuring ρ_{xx}, the current contacts in both $R_{AB,CD}$ and $R_{AD,BC}$ must be *adjacent* to one another. To perform a Hall measurement, the current contacts lie "across" from one another, and the usual relationship between magnetic field **H** and carrier density n is obtained, i.e. $\rho_{xy} = R_{AC,BD} = $ IH/ne [74].

98

One set of experiments I will discuss in Chapter 5 used square van der Pauw samples, with the contacts placed at the vertices of the square. The appropriate measurement configurations are shown in Figure 4.4. Obviously, such a perfectly symmetrical device should yield very nearly the same resistance for all ρ_{xx} measurements, and the same *slope* for ρ_{xy} measurements. Letting $R_{12,34} = R_{13,24} = R$ and substituting into equation (4.6) yields $\rho = \pi R/\ln(2) \simeq 4.532R$.

Now that the basic notions of 2DEG transport measurements have been established, I shall discuss the systematic details of a typical magnetoconductance investigation.

4.3   Measurement

Ultimately, the results of this thesis can be reduced to establishing the interrelationships between four physical quantities: an electric field, **E**, a magnetic field, **H**, a current density, **J**, and a temperature, T. In abstract terms these quantities define the appropriate "phase-space" for modeling electronic transport in δ-layers, and this work, in a loose sense, establishes the appropriate "metric" on this $(\mathbf{E}, \mathbf{H}, \mathbf{J}, T)$ space. In what follows I shall frequently refer to this idea. First, I will discuss the various instruments and apparatus which were used in my experiments.
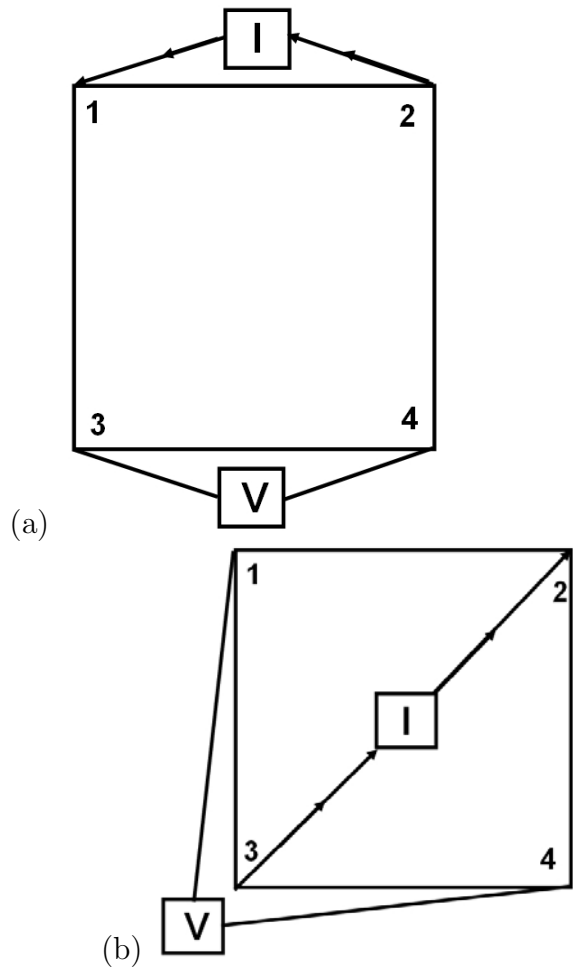
Figure 4.4: Square van der Pauw device and appropriate configurations for measurement of the weak localization (a) and Hall (b) signals. In a perfectly symmetric device, all the measured weak localization signals will have the same magnitude, and the resistivity is related to these measured resistances $(R = V/I)$ by the relation $\rho = \pi R/\ln(2) \simeq 4.532R$.

4.3.1 Instrumentation

Resistance measurements were performed in an Oxford Kelvinox 25 dilution refrigerator which cooled the devices to the low temperatures necessary to observe weak localization. After extensive repairs and modifications (discussed in Appendix C), the lowest achievable temperature of this instrument was $T \simeq 130$ mK. The temperatures of the 1 Kelvin pot, mixing chamber and still were determined via 4-wire measurements on ruthenium oxide (RuO_2) thermometers (produced by Lakeshore cryotronics). These measurements were performed continuously by a Neocera LTC-21 temperature controller, using the calibration curve (resistance vs. temperature) supplied by Lakeshore. Although no definitive measure of the instrument's cooling power at base temperature was made, it seems reasonable to assume it was at least as large as the 50 μW specified by Oxford for operation at $T = 50$ mK.

The devices were mounted on a tilting stage in the refrigerator whose orientation was controlled mechanically via a hermetically sealed feedthrough. By rotating this stage, the angle θ between $\mathbf{J}$ and $\mathbf{H}$ could be placed at an arbitrary angle between $0°$ and $90°$, as depicted in Figure 4.5. The precise value of θ was determined using the Hall effect and the relation for the Hall voltage, $V_H = IH\sin(\theta)/ne$, derived in Appendix A.

Electrical connections to the samples were made with coaxial cables via a "breakout box" at room temperature equipped with 20 BNC connectors.
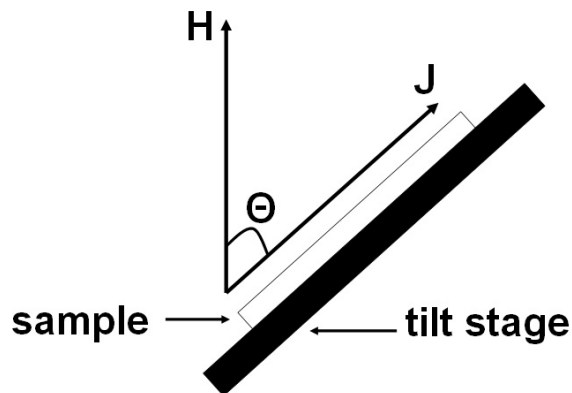
Figure 4.5: Tilting stage diagram. The current density $\mathbf{J}$ (proportional to the bias current I) lies in the plane of the sample, and the magnetic field $\mathbf{H}$ is fixed along the z-axis. The stage orientation is controlled mechanically via a hermetically sealed feedthrough, and the angle θ is determined through a measurement of the Hall resistance: $R_H = H\sin(\theta)/ne$.

Each of these 20 measurement lines was filtered in two stages, as depicted in Figure 4.6. At room temperature, a "π" section filter with a cutoff frequency of 1 MHz was used. Following this, RC filters with a cutoff frequency of 10 kHz were implemented at the 1 Kelvin pot.

Contained in the same dewar as the dilution refrigerator was an Oxford cryomagnetic system. The maximum field this magnet was capable of reaching when immersed in liquid helium (T = 4.2 K) was $\mathbf{H} = 12$ T. The homogeneity of the field (as specified by Oxford) was 1 part in 1000 over a 1 cm^3 spherical volume, at the center of the magnet bore. The power supply controlling the applied field $\mathbf{H}$ was equipped with an analog output voltage
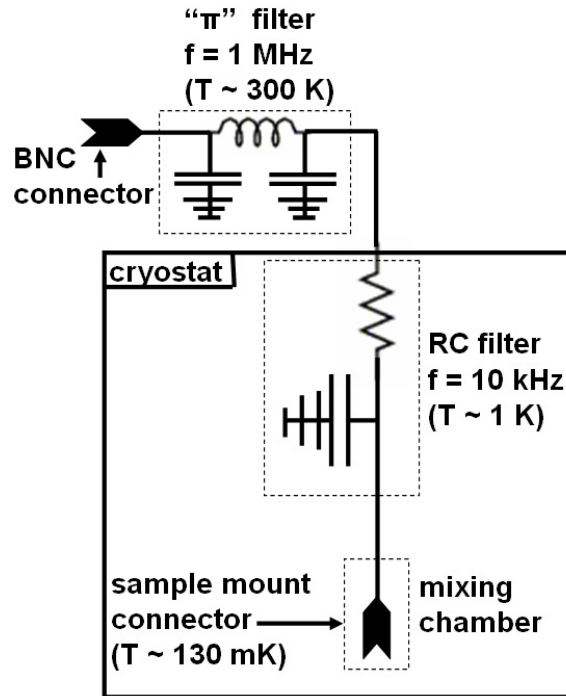
Figure 4.6: Filtering schematic. Two stages of electronic filtering were incorporated to isolate the devices from high frequency noise. At room temperature (T $\simeq$ 300 K) a low-pass "π" section filter was used, with a cutoff frequency of 1 MHz. At T $\simeq$ 1 Kelvin, a low-pass RC filter was used, with a cutoff frequency of 10 KHz. Twenty such lines comprise the total number of leads available for device measurement at base temperature, T $\simeq$ 130 mK.

connection, whose output signal was proportional to **H**. As **H** was varied (usually "swept" at a constant rate $\dot{\text{H}}$), this output voltage was recorded with a DVM to determine the field applied to the sample.

In order to determine a suitable (low-noise) test frequency and investigate whether any anomalous signals were present in the experiment, a Stanford SR785 dynamic signal analyzer was used to measure the spectral density of voltage noise in the measurement configuration. Depending on the voltage signal levels induced in the devices due to current bias and magnetic field configuration (recall that $\sigma(\mathbf{H}_\parallel)$ is always less than $\sigma(\mathbf{H}_\perp)$ in a given device), the signals were often preamplified and further filtered using battery-powered Stanford SR560 differential preamplifiers, with their bandwidth limited to $\sim$ 300 Hz. Figure 4.7 shows a typical noise spectrum, obtained by connecting two weak localization voltage contacts to the A and B inputs of the preamp, and feeding the ouput signal into the spectrum analyzer. No appreciable difference was observed between this spectrum and one taken with the A and B inputs shorted together. Consequently the noise shown in Figure 4.7 is actually the input referred voltage noise of the preamp itself.

The voltages V_{WL} and V_H, as well as the bias current I, were measured using Perkin-Elmer digital signal processing (DSP) 7280 lock-in amplifiers. The principal advantage of using lock-in detection for conductance measurements lies in the ability to reduce the noise bandwidth of the measurement, as well rejecting out of band noise, by increasing the
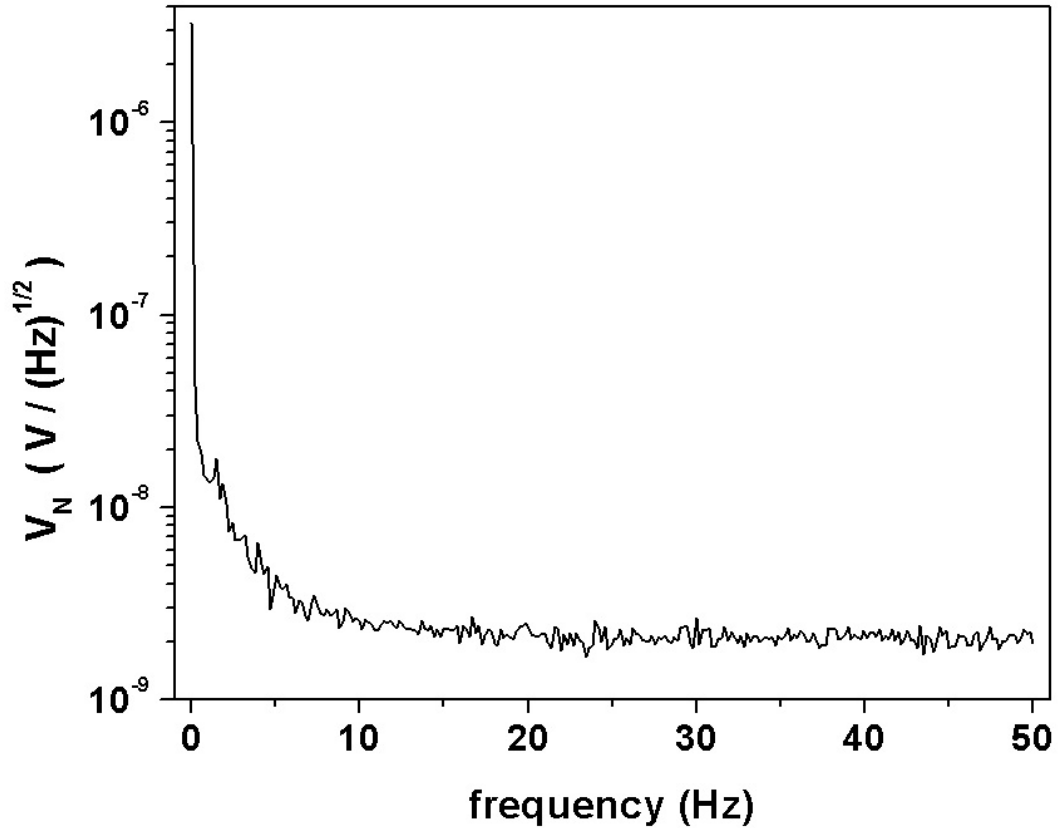
Figure 4.7: Noise spectrum from a δ-doped sample. The spectrum shows the voltage noise V_N (in units of $V/\sqrt{Hz}$) as a function of frequency present in the measurement configuration. A typical test frequency used was f $= 2\pi$e Hz $\sim$ 17.08 Hz, which was sufficiently far from the low-frequency (1/f) portion of the spectrum to allow measurements with good signal-to-noise ratio (SNR).

measurement time constant, τ, and thus increasing the signal-to-noise ratio (SNR) in the experiment. Also equipped with an analog output voltage which was proportional to the signal level at the input of the lock-in, the data from these instruments were also recorded using a DVM. The coaxial cables connecting the device (BNC) contacts to the measurement instruments were configured using the standard "twisted pair" configuration to minimize noise pickup due to time-varying magnetic fluxes, especially at 60 Hz. The DVMs used were Agilent 34401A 6-1/2 digit multimeters.

To record a typical magnetoconductance spectrum, automated data acquisition was performed using a personal computer (PC) with LabView (version 5.1) software. The particular "VI" ("virtual instrument") used for recording data was rather simple in that it merely queried the DVMs and temperature controller for their readings at a user-specified frequency. I typically used an acquisition rate of 1 data point every 5 seconds. At a minimum, each data point consisted of four numbers, corresponding to the $(\mathbf{E}, \mathbf{H}, \mathbf{J}, \mathrm{T})$ parameters discussed earlier. The PC was connected by a GPIB cable to an IOtech 488/F bus extender, which converted the GPIB commands (voltage pulse sequences) into photonic signals (light pulses). These photonic commands were then transmitted via fiber optic cable to a second IOtech extender, which was in turn connected to the measurement DVMs via GPIB cables. A schematic of this situation is shown in Figure 4.8.
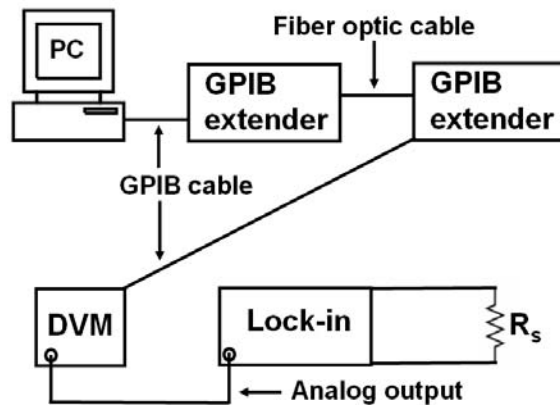
Figure 4.8: Data acquisition schematic. The lock-in amplifier measures the voltage across a resistance, and the analog output of the lock-in is measured by a DVM. GPIB commands from the PC, which controlled the data acquisition, were converted to light pulse signals with the IOtech extender, transmitted via fiber optic cable to another extender, and converted back to GPIB commands to read the DVMs. This arrangement eliminated all electrical connections between the computer and measurement instruments.

4.3.2 Grounding

Given the electrical noise generated by the PC, the fiber optic cable was used to break all electrical connections with this instrument, eliminating high-frequency noise, cross-talk, ground loops, etc. In addition, several other steps were taken to further isolate the measurement system from unwanted noise sources.

Each pumping line connected to the dilution refrigerator was clamped with non-metallic (insulating) centering rings and clamps, which eliminated electrical connections with the pumps associated with the 1 Kelvin pot and the ^{3}He:^{4}He mixture. All instruments were powered through a single "mains" 120 V AC power line, which was first fed through a Topaz ultra-isolation transformer. The "earth ground" connection of this transformer was removed, and it's case "hard wired" to the earth ground of the magnet power supply. This served as the single point ground for the entire experiment, including the cryostat dewar. To prevent ground loop currents from flowing through the BNC shells of the lock-in input BNCs, the coupling inputs were operated in "float" mode, which connected the shells of the BNCs to the chassis ground of the lock-ins via 1 kΩ resistors, establishing a fairly high impedance path to ground. This high impedance would help to minimize any residual issues with ground loops not dealt with by the previous methods. While measurements were being recorded, every effort was made to power down all unnecessary instruments (level meters, magnet thermometers,

high-powered lasers in the neighboring lab, etc.) in order to operate in as quiet an environment as possible. Although these efforts were largely successful, I am certain that the system could be further optimized.

I now turn to the experimental procedures followed in acquiring magnetoconductance data.

4.3.3 Experimental Procedure

The following steps comprise a fairly typical sequence of measurements I performed on δ-doped devices in my work.

After the sample was mounted on the tilt stage in the dilution refrigerator and cooled to base temperature, a noise spectrum was recorded to determine a suitable measurement frequency. A typical example of such a measurement is shown in Figure 4.7. As mentioned previously, the noise shown in Figure 4.7 is actually the input referred noise of the amplifier itself (we shall see later that the noise produced by the samples was generally less than this). For whimsical reasons, the test frequency was often chosen to be $2\pi e$ Hz ($\simeq$ 17.08 Hz). This frequency is sufficiently low that the measurements in this thesis can in essence be considered as DC resistance measurements.

After this, the bias current was varied (from approximately 10 nA to 1 μA) to determine whether or not the V_{WL} vs. I curve was linear (i.e. whether or not the device was *ohmic*). If the device displayed ohmic behavior, a linear fit to the data was performed, and from the slope of this

fit, the $\mathbf{H} = 0$ resistivity of the device was determined. An example of this is shown in figure 4.9. If the curve was nonlinear, the sample generally was not investigated further, due to the difficulty of interpreting such data using the theory of weak localization. Assuming a linear response *was* observed, the bias current was chosen to be as large as possible in order to maximize the SNR, but still low enough such that no heating was apparent (as observed on the mixing chamber thermometer). Oftentimes I = 1 μA was found to be a suitable bias current, with heating usually becoming evident in the neighborhood of I $\simeq$ 5 μA.

Next, a large magnetic field ($|\mathbf{H}| \simeq 5$ T) was applied to the sample in order to establish the $\mathbf{H} = \mathbf{H}_\perp$ configuration. Since the Hall voltage V_H in a field $\mathbf{H}$ is given by $V_H = \text{IH}\sin(\theta)/\text{ne}$, it is clear from this expression that V_H attains it's maximum value when $\theta = 90°$, i.e. when I and H are *perpendicular*. By gradually rotating the tilt stage and tracking the dependence of V_H on the stage position, $\mathbf{H} = H_\perp$ was easily established.

At this point meaningful magnetoconductance data for $\mathbf{H} = \mathbf{H}_\perp$ could be acquired. The usual way this was done was to first set $\mathbf{H} = -1$ T, sweep the field down to $\mathbf{H} = 0$ while recording data, then set $\mathbf{H} = +1$ T and sweep to 0 again. Thus positive field data and negative field data were recorded as separate files. The reason for "partitioning" the field in this way was due to the unfortunate fact that the magnet power supply was really a "unipolar" current source. In other words, $\mathbf{H}$ could not be *continuously* swept through
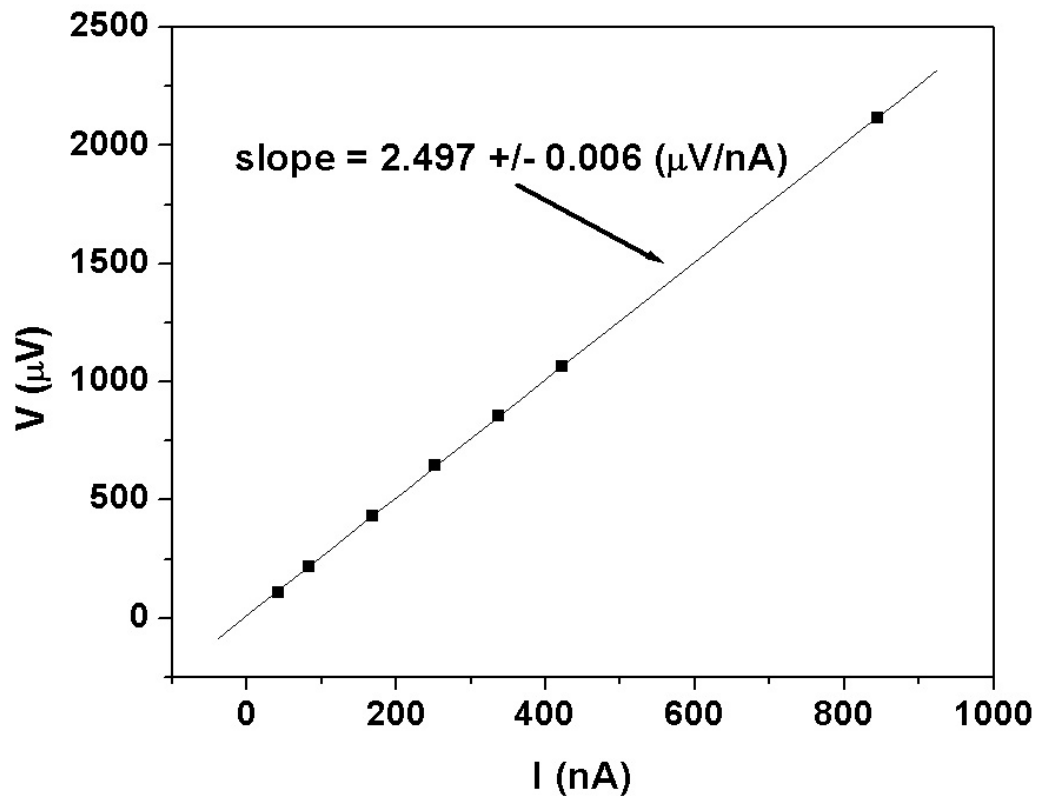
Figure 4.9: Data showing ohmic behavior in an Si:B δ-doped sample. The slope of

the line through these data points gives the resistivity of the device, in this case $R_\square$

$\simeq 2.5$ k$\Omega/\square$.
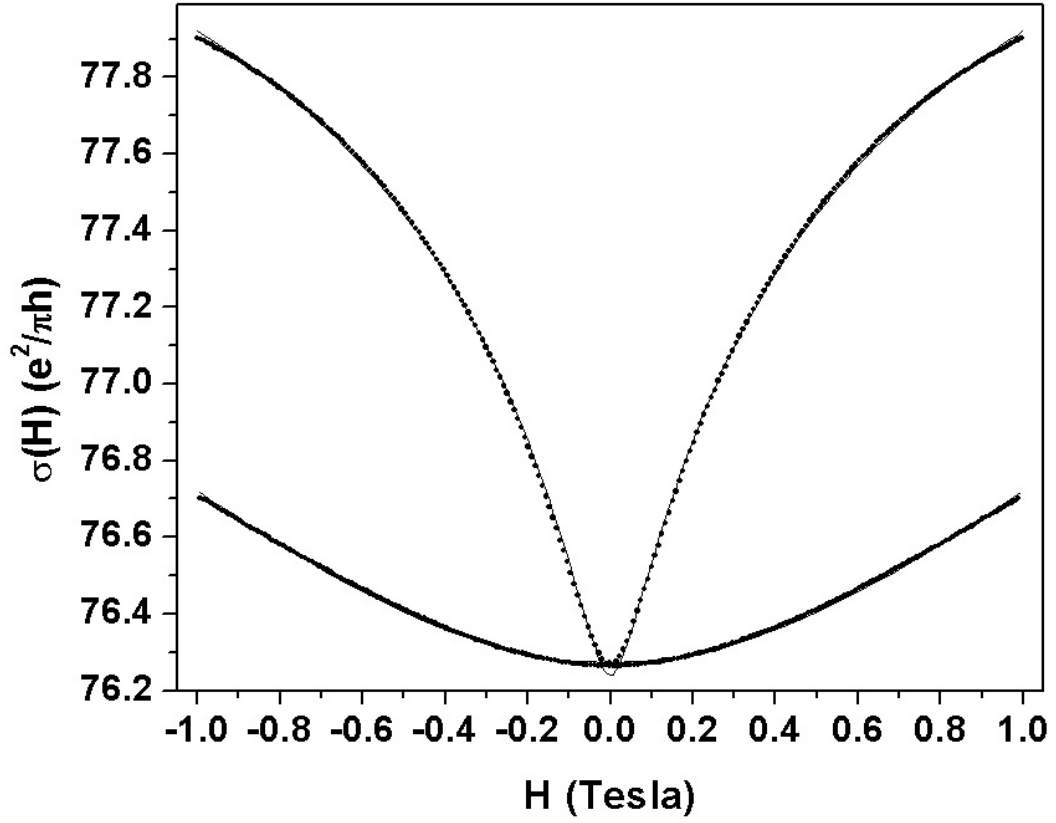
Figure 4.10: Typical magnetoconductance weak localization data (points) with theoretical fits (lines) for Si:P δ-layers. The upper curve corresponds to $\mathbf{H}_\perp$ measurements, the lower to $\mathbf{H}_\parallel$.

zero. If one attempted to do so, when changing field polarities an audible "clunk" could be heard as the power supply mechanically switched the polarity of the magnet leads. This wreaked havoc with the measurements, producing unseemly spikes in the data. This probelm was eliminated by taking the two sets of data separately, and the full magnetoconductance spectra shown throughout this thesis were constructed by "sewing together" the data for $\mathbf{H} \leq 0$, and $\mathbf{H} \geq 0$.

The sweep rate of the magnetic field ($\dot{\mathrm{H}}$) was varied to find a rate slow enough to render any heating effects (due Faraday induced eddy currents) negligible, but fast enough to allow a quick turnaround in data acquisition. In addition, depending on the time constant (τ) of the lock-in used in a given measurement, the sweep rate needed to be sufficiently slow to allow the lock-in to "track" the voltage signals. Good data was obtained using $\dot{\mathrm{H}} = 0.025$ Tesla/minute, $\tau = 5$ seconds, and was found to be compatible with results for measurements taken with smaller values of $\dot{\mathrm{H}}$. The noise levels in the system were sufficiently low that values of τ greater than 5 seconds were seldom necessary. Typical data for $\sigma(\mathbf{H}_\perp)$ and $\sigma(\mathbf{H}_\parallel)$ with $|\mathbf{H}| \in [-1,+1]$ Tesla are shown in Figure 4.10.

After the $\mathbf{H}_\perp$ data had been recorded, the tilt stage was gradually turned until the $\mathbf{H} = \mathbf{H}_\parallel$ configuration was obtained. Again the Hall effect ($V_H = \mathrm{IH}\sin(\theta)/\mathrm{ne}$) made this determination possible. Now, instead of maximizing V_H, the *slope* of the R_H vs. $\mathbf{H}$ was used to find the angle θ between I and $\mathbf{H}$.

Explicitly, we have

$$R_H = \frac{H sin(\theta)}{ne}. \tag{4.7}$$

Taking the derivative of this expression with respect to H we obtain

$$\frac{dR_H}{dH} = \frac{sin(\theta)}{ne} \tag{4.8}$$

which is (by definition) the slope of the $R_H(\mathbf{H})$ curve. For $\mathbf{H} = \mathbf{H}_\perp$, $sin(\theta) = 1$, and I denote the slope in this configuration by s_0 (i.e. $s_0 = 1/ne$). Obviously, we learn the value of the carrier density, n, from this measurement. Upon rotating to a non-perpendicular orientation, the slope of the Hall curve will be *reduced* because $sin(\theta)$ is now less than 1. Let this new value of the slope be s_1. It is clear that the two slopes are related to one another by the equality $s_1 = s_0 sin(\theta)$. Dividing through by s_0 and taking the inverse sine of the ratio s_1/s_0, we obtain the desired expression for the stage orientation θ:

$$\theta = sin^{-1}\left(\frac{s_1}{s_0}\right). \tag{4.9}$$

This analysis should make it clear that when the sample is in the $\mathbf{H} = \mathbf{H}_\parallel$ configuration, the slope of $R_H(\mathbf{H})$ is *zero*. Figure 4.11 shows several Hall traces taken as the stage was turned to $\mathbf{H} = \mathbf{H}_\parallel$, along with the appropriate θ extracted from (4.9) for each trace. It is worth noting here that no evidence for the stage "drifting" over time was observed, so that once it was rotated to a particular position, it stayed there.

$\sigma(\mathbf{H}_\parallel)$ data was taken in precisely the same fashion as $\sigma(\mathbf{H}_\perp)$, as previously described. A complete data set for both configurations was shown

114
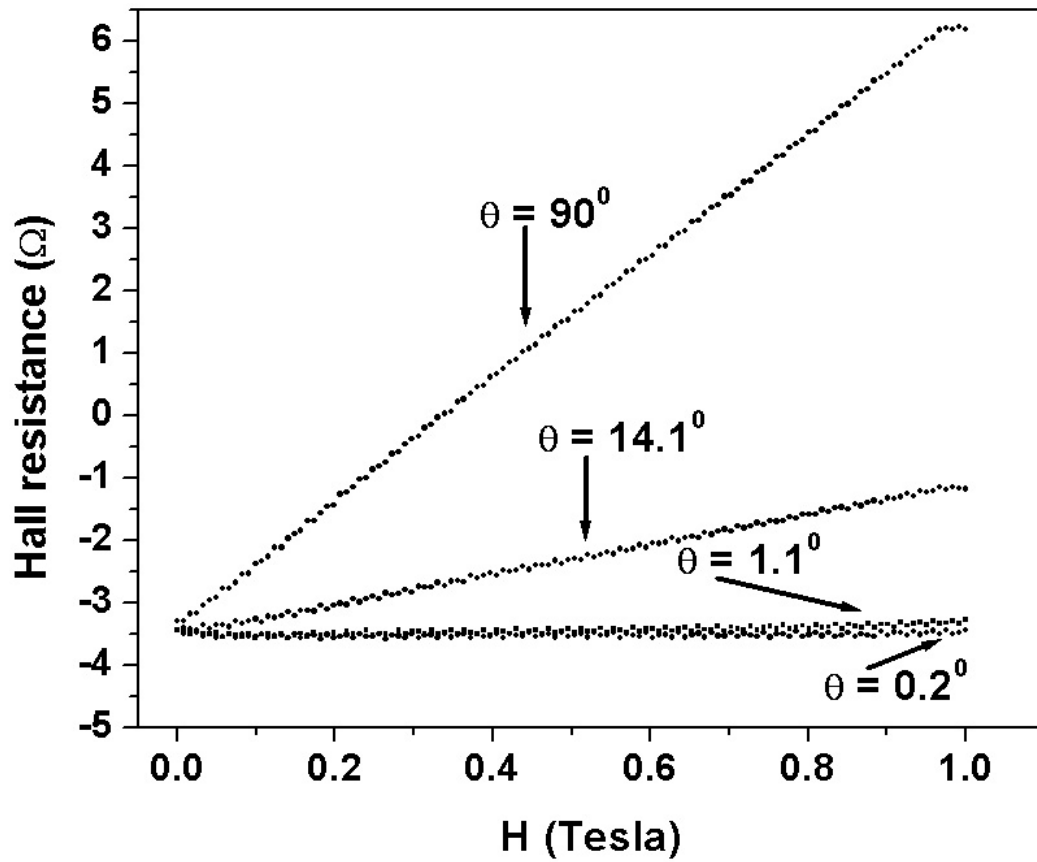
Figure 4.11: Hall data showing the angle θ between **J** and **H**, as determined by equation (4.9). For $\theta = 0$, a horizontal line is produced.

in Figure 4.10.

Once the $\sigma(\mathbf{H}_\perp)$ and $\sigma(\mathbf{H}_\parallel)$ data sets had been recorded, some final temperature-dependent measurements were performed to investigate the influence of the electron-electron interaction in the samples. By applying the maximum amount of power to both the mixing chamber (20 mW) and the still (50 mW), the mixture was removed from the dilution refrigerator and the unit "warmed up" to slightly above T = 4.2 K. At this point, the powers were reduced to their typical base temperature operating levels (0 for the mixing chamber, $\sim$ 1.5 mW for the still), and a fairly low value of τ set on the lock-ins ($\tau \sim$ 1-2 seconds). Data acquisition was begun with T $\geq$ 4.2 K, and the refrigerator was cooled in the usual fashion to base temperature. Once base temperature was reached, data taking was stopped, and the process was repeated if additional measurements were desired. An example of such temperature-dependent resistance data is shown in Figure 4.12. The (logarithmic) resistance increase as the temperature is lowered is another characteristic of weak localization, as it is for the electron-electron interaction. Taking such data in the presence of a magnetic field (also shown in the figure) enables one to distinguish between these two phenomena, as I discuss in Chapter 5.

One final detail in regard to the resistance measurements discussed in this dissertation will now be made. Although the configurations shown in Figure 4.1 were used to perform measurements, at times the limitations of
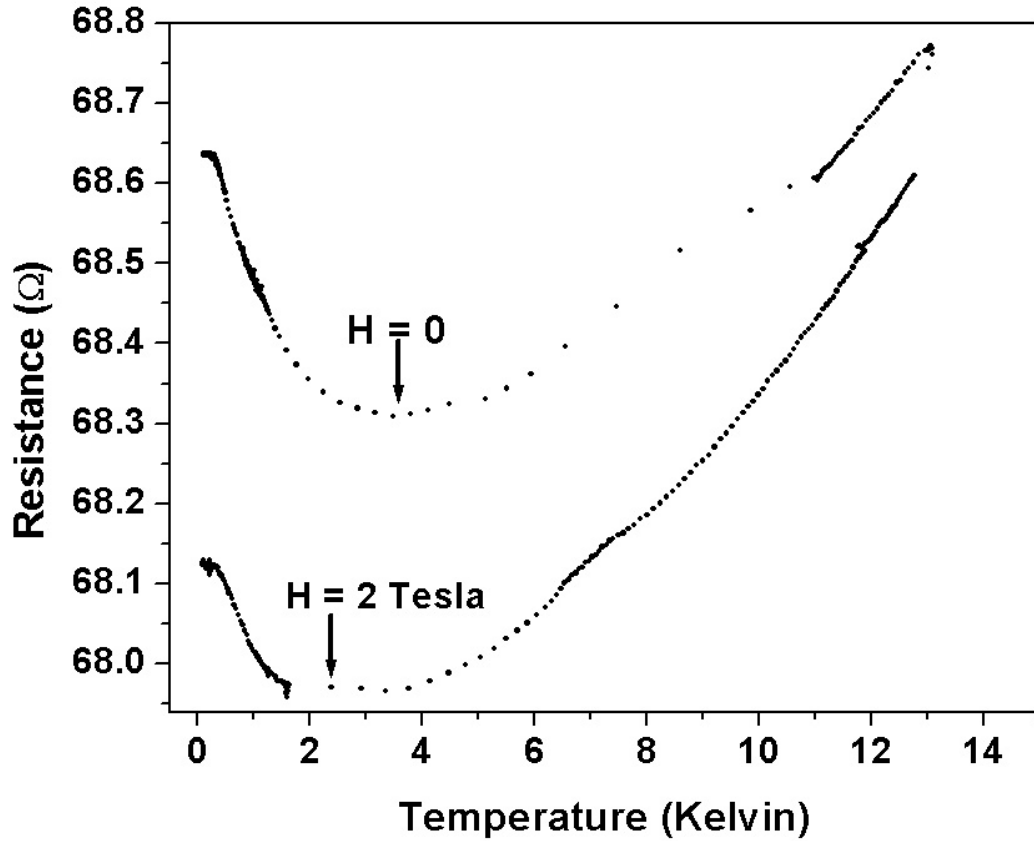
Figure 4.12: Temperature-dependent resistance data, taken in both zero and non-zero magnetic fields. Analysis of such curves quantifies the magnitude of the electron-electron interaction in the device.
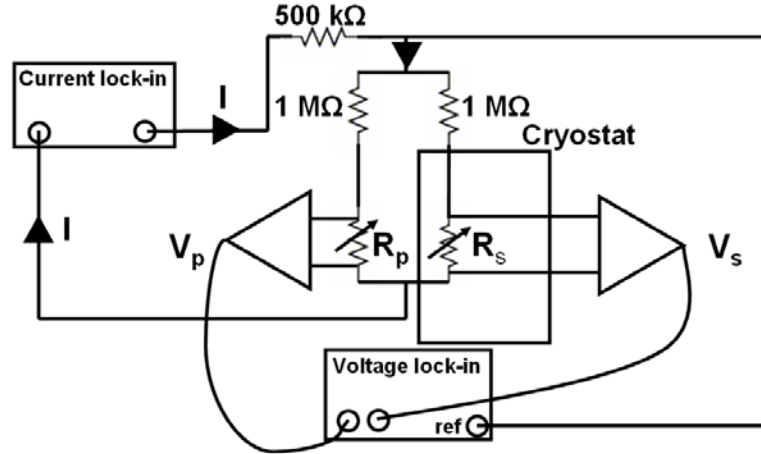
Figure 4.13: Resistance bridge schematic. A room temperature potentiometer, R_p was adjusted to balance the magnetoresistance of the sample R_s at $\mathbf{H} = 0$. The application of an $\mathbf{H} \neq 0$ throws the bridge off balance, inducing a voltage ΔV in the voltage lock-in. A second lock-in measures the current I through the bridge.

the instruments became apparent. In particular, since a DSP lock-in amplifier was used, the finite resolution of the digital-to-analog converters (DACs) on these instruments would occasionally reveal the need for greater measurement sensitivity. (An example of this in a *current* measurement is shown in Figure 4.16.) The finite resolution of the DACs was especially apparent in samples with low values of $R_\square$ in parallel fields, when the induced change in the resistance was exceedingly small. To overcome this deficiency, a custom-made resistance bridge was designed and constructed to improve the measurements.

A schematic of this bridge is shown in Figure 4.13. The current source for

the bridge was supplied by driving an AC voltage from the "current lock-in" through a 500 kΩ resistor, which was then split along the two branches of the bridge before being recombined and "drained" (measured) at the lock-in input. At the top of each branch was a 1 % precision 1 MΩ resistor. Along one branch (in the cryostat) was the sample resistance R_s, and along the other was the balancing element of the bridge, a variable resistance in the form of a room temperature potentiometer, R_p. The idea behind this arrangement was that the 1 MΩ resistors at the top of the bridge would balance the current through each branch to almost exactly equal I/2. The voltages across R_s and R_p (V_s and V_p, respectively) were preamplified and measured with the "voltage lock-in", which was operated in $differential$ $mode$. The choice of lock-in inputs (A and B) was chosen such that the voltage difference between the two signals, ΔV, was given by $\Delta V = V_p$ - V_s = (I/2)(R_p - R_s). At $\mathbf{H}$ = 0, R_p was adjusted until ΔV = 0 was obtained, i.e., until the bridge was $balanced$. Turning on a magnetic field of course causes R_s to decrease (due to the negative magnetoresistance associated with weak localization), throwing the bridge out of balance. Since R_p is independent of $\mathbf{H}$, for $\mathbf{H} \neq 0$, the signal difference always satisfied $\Delta V \geq 0$. Although only $changes$ in the magnetoresistance are relevant for fitting weak localization data, for reference the total magnetoresistance of R_s in a field $\mathbf{H}$ is given by $R_s(\mathbf{H})$ = R_p - 2(ΔV/I).

After a particular experimental run had been concluded, the mixture was

again extracted from the refrigerator, and the dilution unit was allowed to warm up to room temperature. The next step in the experimental investigation involves data reduction and error analysis. Before presenting these results, however, a brief discussion of the errors in the measurements themselves is warranted.

4.4   Measurement Errors

This section is motivated by the question, "What could *systematically* go wrong with these measurements?". It is important to distinguish this concern from other types of errors affecting these experiments, including random errors, such someone (Kenton) bumping the cables during measurements, device-specific anomalies (some of which will be discussed here), or theoretical errors in interpreting the data. Two broad ways of discussing this question are in terms of measurement *accuracy* (i.e. how close to the "true" value was the recorded data?), and *precision* (how reproducible was a given result?). Since each recorded data point corresponds to the specification of a point in the $(\mathbf{E}, \mathbf{H}, \mathbf{J}, \mathrm{T})$ phase space, errors associated with quantifying these physical parameters shall be considered separately.

4.4.1 E

To begin with **E**, it is perhaps more convenient to discuss the corresponding *voltage*, defined by $V = -\int \mathbf{E} \cdot d\mathbf{l}$, since this is what was actually measured. For the Hall bar device in Figure 4.2, $V_{WL} = |\mathbf{E}_\parallel| L$, and $V_H = |\mathbf{E}_\perp| W$, where $\mathbf{E}_\parallel$ and $\mathbf{E}_\perp$ are the components of **E** parallel and perpendicular to the current bias. L and W were lithographically defined according to the relation $L/W = 1$, and measurements of these quantities with tools such scanning electron microscopes (SEM) and atomic force microscopes (AFM) revealed that the feature sizes were generally within 5% of their designed dimensions. Consequently, geometric issues associated with a given sample are *not* a source of error in a voltage measurement. In addition, even if L/W varied substantially from 1 between different devices, for measurements on a *particular* device this ratio would be a *constant*. Thus by determining the actual value of L/W with an SEM or AFM, the data could accordingly be rescaled.

To further discuss voltage measurement errors, I shall consider the recorded signal V to be composed of two parts: the signal of interest, V_S, and an error signal ("noise") ΔV. Mathematically, $V = V_S + \Delta V$, where ΔV can be negative or positive. The SNR is defined as

$$SNR = \left| \frac{V_S}{\Delta V} \right|^2 \tag{4.10}$$

whence it is clear that the higher the SNR, the "better" the measurement. Since we are concerned with resistance measurements, V_S can be controlled

by simply adjusting the device's current bias. ΔV is not as easily manipulated, and several noise sources contribute to its magnitude. These include the Johnson (Nyquist) noise of the device itself, amplifier noise (including *digitization* errors), offset signals due to ground loops or a poor common mode rejection ratio (CMRR), instrumentation drifts induced by gradual changes in the room temperature or humidity, etc. The remainder of this section will demonstrate that the SNR in these experiments was so large as to be essentially irrelevant to the conclusions which were drawn from this work. As an experimentalist, this is a nice situation to be in.

Consider first the voltage error ΔV_T due to the thermal noise of the device itself. The largest values of $R_\square$ measured in the course of this work were $R_\square \simeq 3$ k$\Omega/\square$. The spectral density of the noise produced by such a resistance is given by the well-known Nyquist expression $\sqrt{4k_BTR_\square}$, and assuming V_T was measured with $\tau = 1$ second at T = 4.2 K, we have $\Delta V_T \simeq 1$ nV. This would of course be lower at the base temperature of the refrigerator, and for lower resistance samples.

Next, I consider Figure 4.7 to estimate the voltage error, ΔV_A, due to the preamplifier. From Figure 4.7, I estimate the spectral density of the amplifier noise to be $\simeq 3$ nV/$\sqrt{Hz}$ for the typical test frequencies I used of 10 - 20 Hz. Again using $\tau = 1$ second for the lock-in time constant, I find $\Delta V_A = 3$ nV.

The final voltage error I consider is that due to the finite CMRR of the amplifier, ΔV_C. To estimate ΔV_C, I use the specified value of CMRR = 100

dB for the 7280 lock-in amplifier. Assuming a 1 μA current bias through a total common mode resistance of 2kΩ (including the RC filter resistance of Figure 4.6), the voltage signal applied to *both* inputs of the lock-in is $V_0 = 2$ mV. Since the common mode error signal is defined [75] by CMRR = $20\log_{10}(V_0/\Delta V_C) = 100$, we obtain $V_C = 20$ nV.

The total voltage error in these measurements, ΔV, is given by summing the separate contributions in quadrature, since they are indendent of one another. That is,

$$\Delta V = \sqrt{(\Delta V_T)^2 + (\Delta V_A)^2 + (\Delta V_C)^2} \qquad (4.11)$$

which yields $\Delta V \simeq 21$ nV. Thus we see that the finite value of the amplifer's CMRR dominates the volatge errors in these measurements. Nevertheless, this noise level is extremely small when compared with actual signals. Even for the lowest resistance device measured in this work, $R_\square \simeq 250$ $\Omega/\square$, and a modest bias current of $I = 100$ nA, I obtain a SNR = $(25\ \mu V/21\ nV)^2 \simeq$ 1.4x10^6! Thus, the limitations of these experiments lie in interpreting the results, and not with the voltage measurements themselves.

Although this analysis is rather convincing, a variety of other cross-checks were performed to ensure the quality of these measurements. One check included examining the dependence of the measured resistance on the test frequency, f. By varying f from DC (f = 0) to f = 1 kHz, it became obvious that current leakage to ground was a real issue at higher frequencies, presumably due to the reduced impedance of the capacitance in the coaxial

cables and RC filters, which varies like 1/fC. This implies that low frequency measurements are easier to interpret, since there is only one signal channel to consider at DC, while there are two for $f \neq 0$ (the "in-phase" and "quadrature" signal components). The usual way of establishing the appropriate signal phase was to "autophase" the lock-in at $\mathbf{H} = 0$ to be in phase with the current through the device. Nonetheless, even at the low measurement frequencies used in these experiments, the quadrature signal showed non-zero response to the varying magnetic field. No effort was made to analyze this component of the signal.

Another step which was taken to enhance the quality of these measurements was to judiciously allocate the gain of the DSP lock-in to eliminate digitization errors. The 7280 had two stages of gain: AC gain (which amplified the signal *before* DSP), and demodulator gain (which amplified the signal using DSP). The largest possible value of AC gain was used to minimize such digitization errors, and it is worth mentioning that when using the bridge of Figure 4.13, no evidence of digitization was observed. With regard to the accuracy of the lock-in's gain, Perkin-Elmer claims the 7280 gain is accurate to 0.6%.

Finally, in order to investigate whether temperature or humidity drifts in the laboratory were an issue in these experiemnts, a long (17 hour) trace was taken of a sample with $\mathbf{H} = 0$, shown in Figure 4.14. This shows that, although some drifts were apparent, the variation of the resistance over this
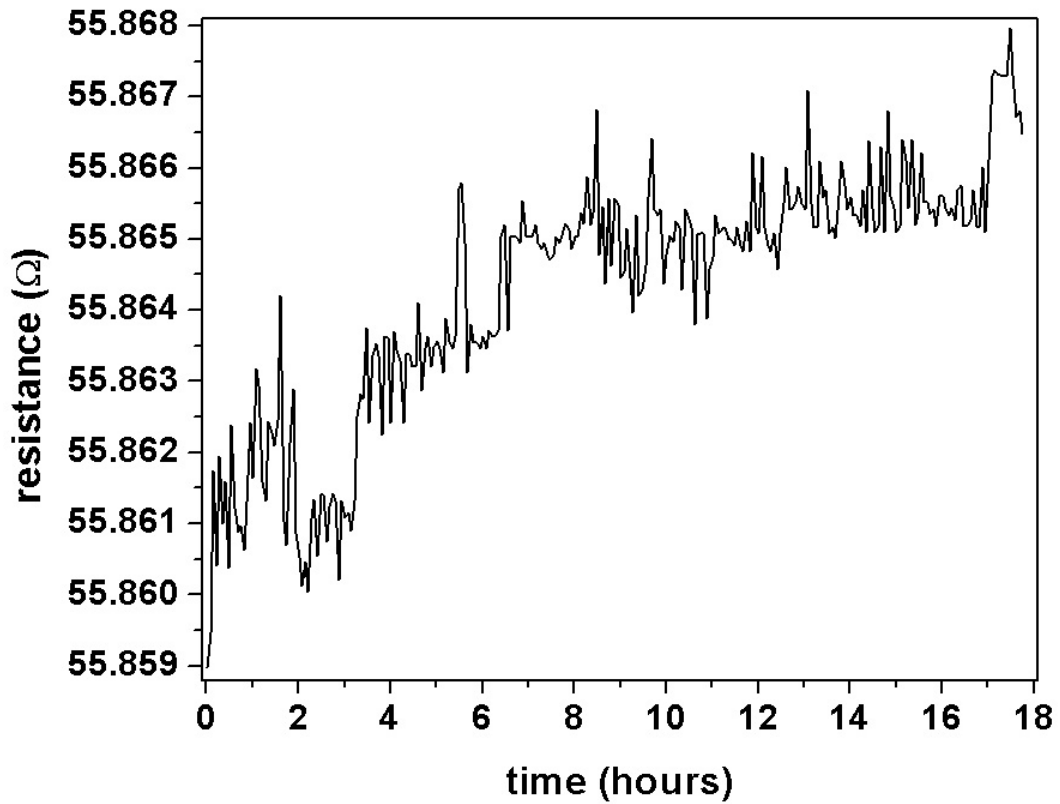
Figure 4.14: Measurement drift over time. Although the measured resistance does vary over time, and shows a slightly increasing trend, the variation is quite low. The maximum resistance over the 17 hour measurement period is $R_{max} = 55.868\ \Omega$, the minimum $R_{min} = 55.859\ \Omega$, and are therefore 99.98% consistent. Typical weak localization sweeps occurred on much shorter timescales (~ 1 hour) than this trace, and produced much larger signal variations, therefore such drifts are inconsequential to data analysis.

interval was extremely small (approximately 2 parts in 10^4), and, when compared with the changes induced by application of a magnetic field and the typical sweep times ($\sim$ 1 hour), are negligible.

4.4.2   H

In reality, a direct measurement of **H** was not performed. The reason for this is that the power supply would source a given current, and I assumed that the field-to-current ratio was accurate. For this system, the conversion factor was 0.1258 (Tesla/ampere). However, because of hysteresis effects inherent to all superconducting magnets [76], the field experienced by the sample was in general different from the intended value. To illustrate this point, consider the R(**H**) data shown in Figure 4.15. The abrupt discontinuity of R near **H** $\simeq$ 275 gauss can be traced to the presence of the superconductor indium (In) near the sample, which was used as a solder on this device. One of the basic properties of type I superconductors such as In is the existence of a critical magnetic field $\mathbf{H_c}$, below which the metal is superconducting, above which the metal is "normal" (non-superconducting). For In, $\mathbf{H_c}$ = 293 gauss [2], very close to the discontinuity in Figure 4.15. When **H** < $\mathbf{H_c}$, type I superconductors *completely expel* magnetic flux from their interior (the *Meissner effect*). On the other hand, weak localization measurements are extremely sensitive to the *vectorial* nature of the applied **H**.
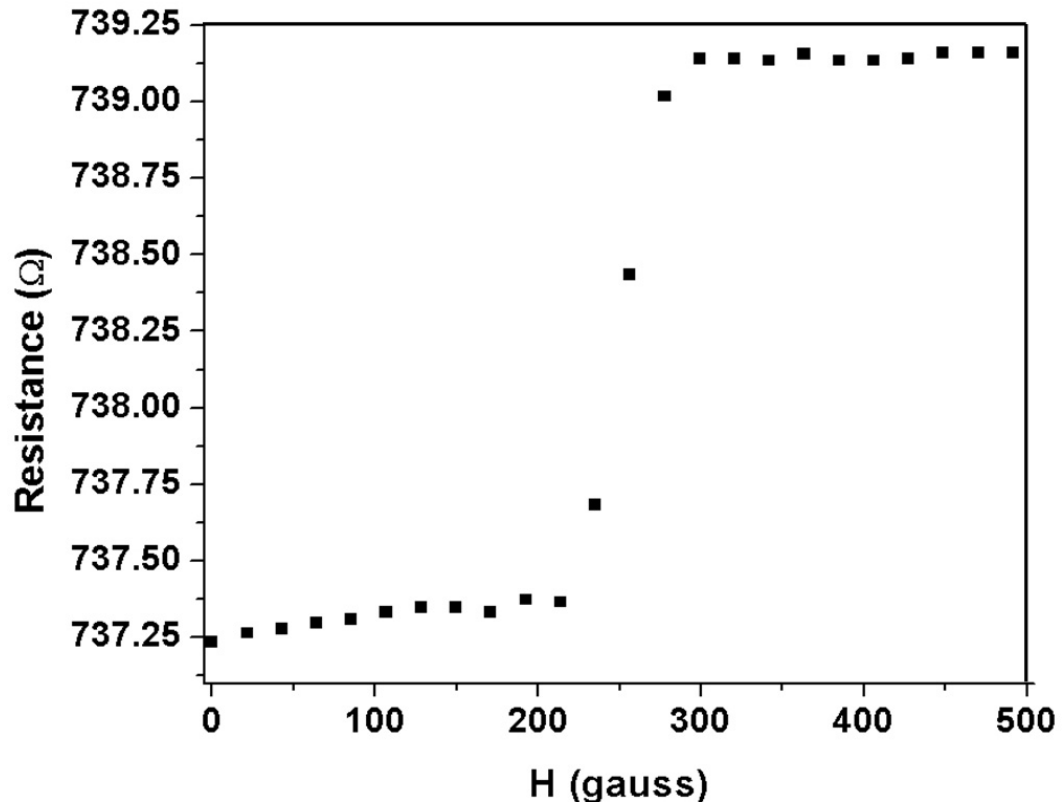
Figure 4.15: Impact of the Meissner effect on the magentoresistance due the use of In solder. The transition from the superconducting to normal state in In occurs at $H_c = 293$ gauss. This distorts the local magnetic field applied to the device, and consequently the measured resistance.

Given these two considerations, the explanation of the data in Figure 4.15 is that instead of the device experiencing a gradual change in flux bias, when sweeping through $\mathbf{H_c}$ the flux bias changes *discontinuously*. In effect, the magnetoresistance of the device acts as an independent magnetometer of the field $\mathbf{H}$. Clearly whether $\mathbf{H} < \mathbf{H_c}$ or $\mathbf{H} > \mathbf{H_c}$ has a profound impact on the *local* $\mathbf{H}$ applied to the sample, and consequently the measured resistance. Assuming that the In near the sample really did have $\mathbf{H_c} = 293$ gauss, then the onset of the transition region in Figure 4.15 gives an estimate of the actual $\mathbf{H}$ applied to the sample. Examining this figure shows that the discontinutiy occurs at roughly 275 gauss, and is therefore reasonably close to the expected value of 293 gauss. This difference is quite small when compared with the typical sweep ranges (+/- 1 Tesla). Incidentally, this analysis suggests that a convenient and highly accurate method of calibrating both $\mathbf{H}$ and T in a given low temperature apparatus is through 4-wire measurements on type I superconductors near their critical temperatures and magnetic fields.

The *homogeneity* of the field is another concern in my measurements. Because the magnetoresistance is highly anisotropic, stray perpendicular fields would lead to a larger response than for $\mathbf{H}$ strictly parallel to the 2DEG plane. Given that $\nabla \cdot \mathbf{B} = 0$ *always*, magnetic field lines are never truly straight: they always have a slight curvature. As mentioned earlier, Oxford claims that the homogeneity at the center of the magnet bore was

good to 1 in 1000 over a 1 cm^3 spherical volume. Therefore one way of estimating the influence of this effect is to "scale down" this figure to a typical device size of 50 μm x 50 μm. Doing this yields a field homogeneity of $(10^{-3})^{2/3} = 0.01$ per cm^2, and since the device area was $(50\mu\text{m})^2 = 2.5\text{x}10^{-5}$ cm^2, this suggests that the field was homogeneous to better than 3 parts in 10^7 across each square of the device! This analysis is probably "too good to be true", and thus I take the following approach.

The superconducting solenoid which was used in these experiments had a length L of approximately 35 cm, and a bore diameter of 52 mm, hence a radius a of 2.6 cm. Given the field/current ratio of 0.1258 T/A of this solenoid, we can find the approximate number of turns per unit length, N, from the equation [78]

$$N = \frac{H}{\mu_0 I} = \frac{0.1258(\frac{T}{A})}{\mu_0}. \tag{4.12}$$

Since $\mu_0 = 4\pi\text{x}10^{-7}$ N/A^2, this yields N $\simeq 10^5$ turns/meter.

The issue of the field inhomogeneity near the center of a solenoid is treated in chapter 5 of [46], where the following result is obtained for the radial component H$_r$ of **H**, an on-axis distance z and radial distance r from the geometric center of the solenoid:

$$H_r = \frac{24\mu_0 N I a^2 r z}{L^4}. \tag{4.13}$$

Inserting the values above, and a current corresponding to 1 T (7.949 A), I find H$_r \simeq 2$ gauss. Since the radial field is proportional to the magnet current I, H$_r$ will generally be even less than this. When compared with the

axial field (1 T), we see that field inhomogeneities were not a concern in these measurements.

4.4.3   J

The current density $\mathbf{J}$ was determined by the lithographically defined width of the samples, W, and measurement of the current bias, I, with the 7280 lock-in operated as a current amplifier. As mentioned earlier, the dimensions of the sample are relatively unimportant, since their precise values can be independently determined with SEMs or AFMs. Therefore I was primarily concerned with determining I.

A measurement of I for $|\mathbf{H}|\in[0,+1]$ T is shown in Figure 4.16. The resolution limitations of the DACs are strikingly apparent, and the discrete nature of the recorded data points is obviously unphysical. This measurement was performed in a manner analogous to that shown in Figure 4.1, with a 1 MΩ resistor placed in front of the 1 Volt AC source of the lock-in serving as the current source. The behavior displayed by this graph is easily understood by considering the fact that the entire sample, including the contact wires, etc., display weakly localized behavior. The *entire sample* has a resistance maximum at $\mathbf{H} = 0$, and as the field is increased, the entire sample becomes less resistive, therefore a larger current flows through the device. To overcome this, one might be tempted to construct a "current bridge", analogous to the resistance bridge of
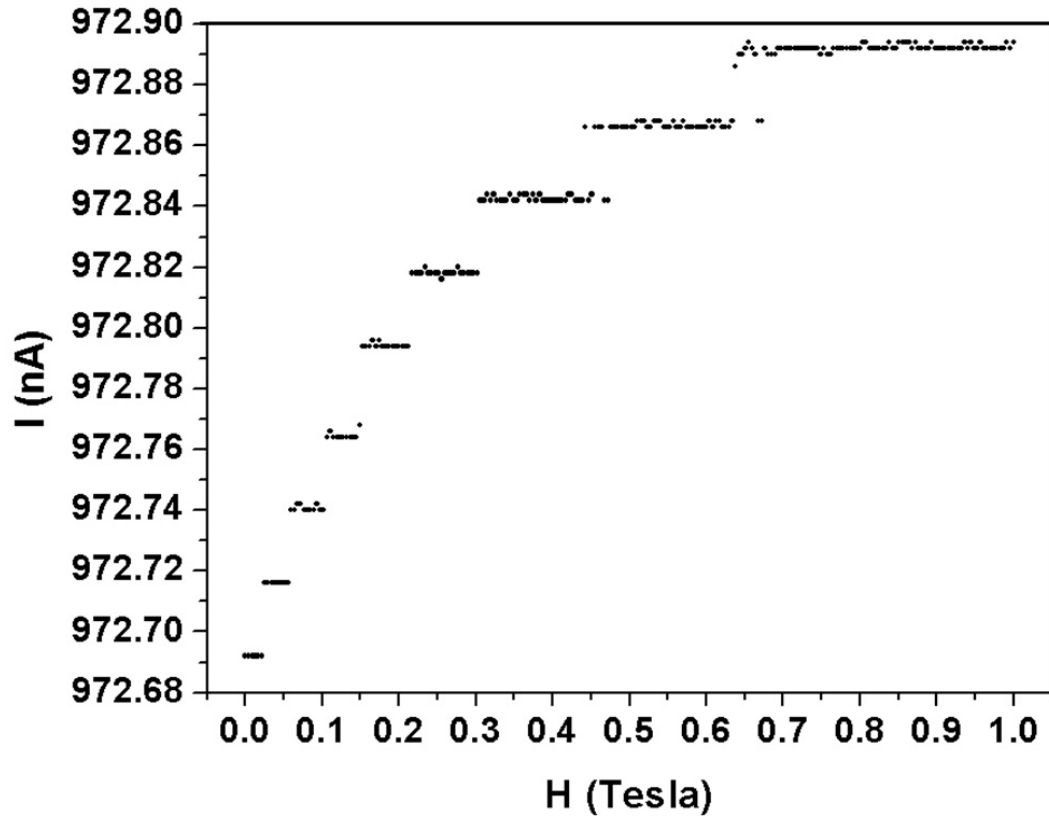
Figure 4.16: Finite resolution of DAC in a bias current measurement. Despite the limitations of this measurement, the current over the full magnetic field range is still constant to 2 parts in 10^4.

Figure 4.13, but such an effort is unnecessary, since I is constant to roughly 2 parts in 10^4. Thus we see that determination of the bias current was not a significant limitation of these measurements.

4.4.4   T

The most uncertain quantity in these experiments was T, the
temperature of the device. Several studies (see [77] and references therein)
have demonstrated that, in general, the electronic temperature T_e and the
phonon (lattice) temperature T_p are unequal. In the experiments discussed
here, the sample and thermometer were physically separated by ~ 2 cm.
Therefore assuming that T_e was equal to the phonon (mixing chamber)
temperature T_p is inaccurate. However, this is insignificant for most of the
considerations discussed in this thesis. The reason for this is that, for the
most part, experiments were performed only at *constant* temperatures (T =
4.2 K and the base temperature of the refrigerator, T $\simeq$ 130 mK). The only
time the sample temperature was *absolutely* certain was at T = 4.2 K, when
the inner vacuum chamber of the dilution refrigerator was filled with ^{3}He
exchange gas and the cryostat was filled with liquid ^{4}He. T_e was certainly
colder at base temperature, and looking closely at the data in Figure 4.12, it
is apparent that the resistance *saturates* in Si:P devices below T $\simeq$ 200 mK.
I also observed such saturation in Si:B devices, but in these samples the
onset occurred at much higher temperatures: T $\simeq$ 800 mK. The physical
origin of this behavior will be discussed in Chapter 5, but Figure 4.12
suggests that despite T_e being unknown at base temperature, the observed
saturation makes it plausible that T_e was *constant* during the
measurements. Therefore, imprecise knowledge of T was not a significant

source of additional (propagated) error in these experiments: the samples were pretty cold regardless.

4.4.5 θ

Although I have now discussed the errors associated with the physical variables $(\mathbf{E}, \mathbf{H}, \mathbf{J}, \mathrm{T})$, an additional parameter which is important to the conclusions drawn from these measurements is the angle θ between $\mathbf{H}$ and $\mathbf{J}$. At this point it is reasonable to ask how sensitive the stage orientation technique was, or what angular resolution, $\Delta\theta$, was achievable? The answer to this is straightforward.

Since θ is determined through a measurement of V_H, a *voltage signal*, the voltage noise in the measurement system, V_N, will ultimately limit the determination of $\theta = 0$. A lock-in amplifier operated with a time constant τ will, on average, lead to an uncertainty $\delta\mathrm{V}$ in a voltage measurement given by $\delta\mathrm{V} = \mathrm{V}_N/\sqrt{\tau}$. Intuitively, this makes sense, since one would expect that by averaging a given signal for a longer time a more precise measurement would be produced. Once again, I use $\mathrm{V}_H = \mathrm{IHsin}(\theta)/ne$ to derive an expression for $\Delta\theta$ given $\delta\mathrm{V}$.

Since in parallel fields we are concerned with very small angles between I and $\mathbf{H}$ ($\theta \ll 1$), we can expand $\sin(\theta)$ to lowest order in a Taylor series and use the approximation $\sin(\theta) \simeq \theta$. I equate this small angle θ with the resolution limit $\Delta\theta$. When I and $\mathbf{H}$ are as parallel as possible, the ability to

distinguish V_H from δV is lost, or the equality

$$\delta V = \frac{IH\Delta\theta}{ne} \qquad (4.14)$$

holds. Solving this equation for $\Delta\theta$, I obtain the desired expression for the angular resolution limit:

$$\Delta\theta = \frac{ne\delta V}{IH} = \frac{neV_N}{IH\sqrt{\tau}}. \qquad (4.15)$$

What is interesting here is that the numerator consists of quantities over which the experimentalist has no (or at best, little) control, whereas the denominator is under complete control. Thus, in order to improve (reduce) $\Delta\theta$, one should work with a large bias current I in a large magnetic field $\mathbf{H}$, and average the Hall signal for a long time τ. Using $\delta V = 5$ nV, n = $10^{14}/\text{cm}^2$, I = 1μA, and H = 1 T, leads to $\Delta\theta = 8\text{x}10^{-4}$ radians ($\simeq 0.05°$).

Now that the measurement details of this research have been established, I turn to Chapter 5, and a discussion of my experimental results.

Chapter 5

Results

The results of my low temperature magnetoconductance measurements on δ-doped Si are presented in this chapter. Although the primary focus will be upon Si:P δ-layers, a limited study of Si:B δ-layers is also presented. The theory of weak localization developed in Chapter 2 will serve as my primary tool for interpreting the data. In addition, I critically examine the various experimental and theoretical approaches incorporated throughout this work for their advantages and limitations.

5.1   Si:P δ-Layers

The principal motivation for a detailed study of Si:P δ-layers lies in the potential these structures have in device applications. Some particular examples were mentioned in the Introduction (Chapter 1), and will not be

discussed further here. Instead, I shall concentrate on two particular aspects of Si:P δ-layer physics. One study examines the impact a high temperature anneal has on the electronic characteristics of the samples. The other investigates the dependence of the magnetoconductance signals on n, the sample carrier density. I also establish several limitations the present theory of weak localization has with respect to δ-doped Si:P systems.

5.1.1 Diffusivity Measurements

The desire to establish weak localization as a tool for measuring the thickness of δ-layers can be traced back to a paper of Mensz and Wheeler [80]. By performing weak localization measurements on Si MOSFETs in perpendicular and parallel magnetic fields, these workers estimated that the rms value of the 2DEG thickness in their samples was $\simeq 0.21$ nm, i.e. *less* than a Si monolayer. Being able to achieve this type of resolution in δ-doped samples would far exceed the limitations of other established methods for measuring $\mathcal{T}$, including capacitance-voltage (CV) profiling (chapter 9 of [1]), x-ray diffractometry [81], transmission electron microscopy (TEM) [34], and SIMS (Secondary Ion Mass Spectrometry) analysis. Each of these techniques has its own advantages and disadvantages, and those of SIMS, the most common approach, were discussed in Chapter 3. I now turn to my experiments using weak localization for measuring $\mathcal{T}$, reported in [79].

Experimental Procedure

For my measurements, four distinct 50 μm x 50 μm van der Pauw devices were fabricated, as described in Chapter 3. The wafer used for these devices corresponds to the point labeled "A" in Figure 2.10 ($n \simeq 10^{14}/cm^2$), and a SIMS analysis from a sample of this wafer is shown in Figure 5.1 (this is the same plot as Figure 3.5). The reason for going through the somewhat elaborate fitting procedure associated with van der Pauw devices is simple. For measurement of a Hall bar, 6 wires are needed (source, drain, and four voltage contacts), whereas with a van der Pauw device it is the bare minimum of 4. In addition, one lead per device was necessary as an ancillary contact to check for conduction through the substrate (Chapter 3), making 7 contacts necessary for a Hall bar device. As discussed in Chapter 4, the dilution refrigerator used in these experiments had 20 total experimental leads. Thus using Hall bars, realistically only two devices could be measured in a given experimental run (cooldown). In contrast, van der Pauw devices allowed four different samples to be measured in a single cooldown, in effect doubling the amount of data obtained. Since the work required to cycle a dilution refrigerator from room temperature to base temperature and back is time-consuming and non-trivial, the use of van der Pauw devices was an obvious choice.

After defining the device "mesa" and cleaning off the resist mask as described in the device processing recipe of Chapter 3 (steps 10 through 15),
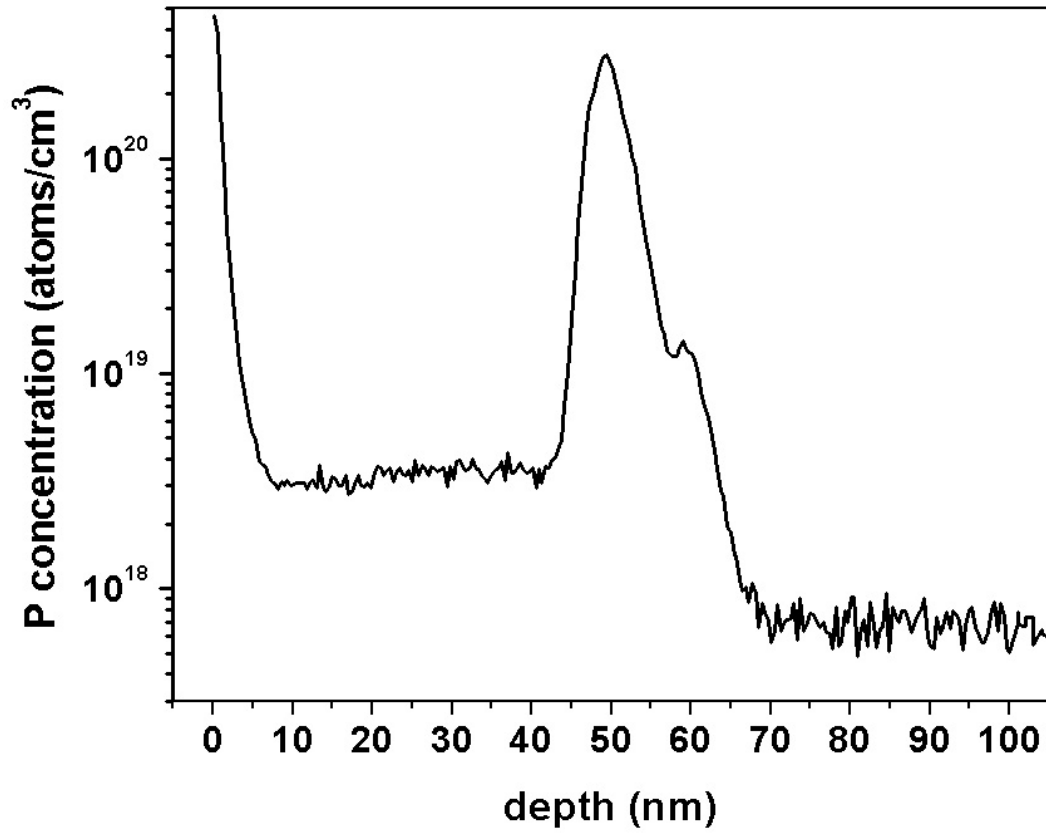
Figure 5.1: SIMS data from a sample of wafer A, with n $\simeq 10^{14}/\text{cm}^2$. All of the devices used in the diffusivity study were fabricated from this wafer. This SIMS profile corresponds to the cook 0 (unannealed) device, and is the same as shown in Figure 3.5.

three of the four samples were subjected to an 850 °C anneal in a nitrogen atmosphere, performed in a Barnstead Thermaline 79300 tube furnace (*not* a rapid thermal annealer). The annealing times were for 5, 10 and 15 minutes, and henceforth these devices will be referred to by the time each was annealed as cook 0, cook 5, cook 10 and cook 15. Two considerations led to this choice of annealing times. First, prior experience had shown that if the devices were annealed for too long (40+ minutes), $\mathcal{T}$ in these devices would "saturate" and become indistinguishable from one another. This leads to the second rationale for the chosen annealing times, which was to explore precisely how sensitive this weak localization approach is for measuring $\mathcal{T}$. As will be shown, with an appropriate (and as yet undeveloped) theoretical footing, this technique should prove to be the most precise method of measuring δ-layer thicknesses yet demonstrated.

Following the anneals, the fabrication process was completed in a parallel fashion for all of the devices (resuming at step 16, Chapter 3), the only difference being I used In solder instead of wire bonds (step 31) to connect wires to the Au contact pads. Thus, aside from statistical variations in the wafer itself, the *only* difference between the devices was annealing time. The samples were then mounted in the dilution refrigerator and measured as described in Chapter 4.

Results

Before fitting data to the appropriate expressions, a standard

symmetrization procedure was followed with weak localization data. This

consisted of transforming the data according to:

$$R_{WL}(+/-\mathbf{H}) = \frac{R_{WL}(+\mathbf{H}) + R_{WL}(-\mathbf{H})}{2}. \qquad (5.1)$$

The effect of this was to remove any of the residual asymmetries which are

present in all 4-wire magnetoresistance measurements [82] , and fit data only

to the symmetric component of the conductivity tensor. This technique is

both experimentally and theoretically well-founded, and has been discussed

extensively elsewhere [68]. Figure 5.2 shows a plot of typical

magnetoresistance data in both "raw" (unsymmetrized) and symmetrized

forms. Clearly, the data is highly symmetric to begin with, and this

procedure has a negligible effect on the interpretation. Henceforth, *all* weak

localization data presented in this thesis will be in symmetrized form. The

reader should thus bear in mind that the plots I present are somewhat

redundant, since by symmetrizing I am displaying how the data depends on

the magnitude of $\mathbf{H}$, not it's sign.

For completeness, I re-state the equations cited in Chapter 2 which I used

for fitting data and calculating $\mathcal{T}$. First, in perpendicular fields, the change

in the magnetoconductance, $\delta\sigma(\mathbf{H}_\perp)$, is expected to take the form

$$\delta\sigma(H_\perp) = (\frac{e^2}{2\pi^2\hbar})[\Psi(\frac{1}{2} + \frac{\hbar}{4eH_\perp\ell_\phi{}^2}) - \Psi(\frac{1}{2} + \frac{\hbar}{2eH_\perp\ell_e{}^2}) + \ln(2(\frac{\ell_\phi}{\ell_e})^2)] \quad (5.2)$$
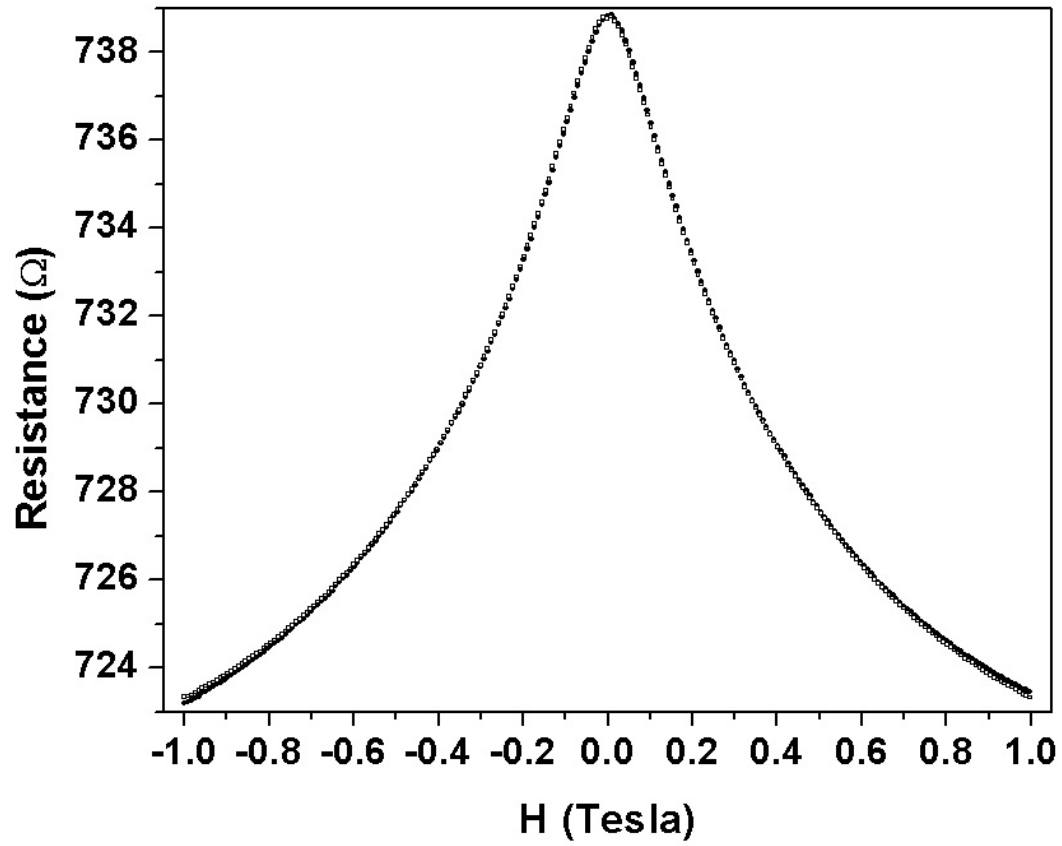
Figure 5.2: Raw (unsymmetrized) weak localization data (solid points) and symmetrized data (open squares). The measurements are highly symmetric before applying equation (5.1), and hence this procedure has a negligible effect on data analysis.

where Ψ is the digamma function, ℓ_e the mean free path, and ℓ_ϕ the dephasing length.

In parallel fields, $\delta\sigma(\mathbf{H}_\parallel)$ is given by

$$\delta\sigma(H_\parallel) = (\frac{e^2}{2\pi^2\hbar}) \ln(1 + \gamma H_\parallel^2) \qquad (5.3)$$

requiring the single parameter γ for fitting.

The model for $\mathcal{T}$ used in [79] assumes that the inequality $\ell_c \ll \ell_e \ll \ell_\phi$ was valid in all of the devices measured, which corresponds to the "homogeneous broadening" limit described in Chapter 2 and [62]:

$$\mathcal{T} = \left(\frac{1}{4\pi}\right)^{1/4} \left[\left(\frac{\hbar}{e\ell_\phi}\right)^2 \left(\frac{\gamma\ell_e}{\ell_c}\right)\right]^{1/2}. \qquad (5.4)$$

A "ball park" estimate of $\ell_c = 1/\sqrt{n}$ was used in [79]. I return to this point later when I discuss the systematic errors associated with my work.

The data and theoretical fits for my four devices are shown in Figures 5.3 through 5.6. The difference between the $\sigma(\mathbf{H}_\perp)$ (upper curves) and $\sigma(\mathbf{H}_\parallel)$ (lower curves) configurations is easily understood using the phenomenological "cross section" argument presented in Chapter 2. When $\mathbf{H} = \mathbf{H}_\parallel$, the effective cross section of the 2DEG is significantly smaller than for $\mathbf{H}_\perp$. Thus less flux penetrates the electron system, and less of a change in conductance is induced. Furthermore, we see that for $|\mathbf{H}| = 0.5$ T, the signal "contrast", $\Delta\sigma$, *decreases* with annealing time ($\Delta\sigma \equiv \sigma(\mathbf{H}_\perp)$ - $\sigma(\mathbf{H}_\parallel)$). Equivalently, the greater $\Delta\sigma$, the smaller is $\mathcal{T}$ of the 2DEG in the device, *independent* of the model used to interpret the data. I now turn to an
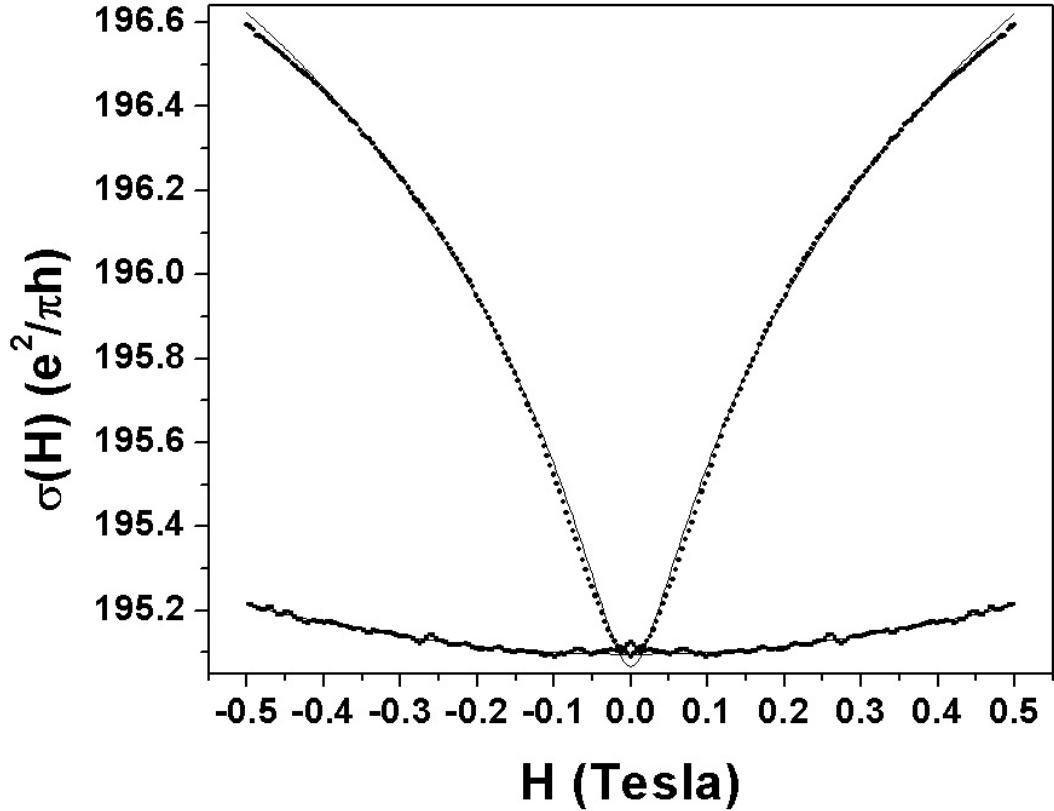
Figure 5.3: Cook 0 weak localization data. The best-fit parameters to equations (5.2) and (5.3) are $\ell_e = 30$ nm, $\ell_\phi = 101$ nm, and $\gamma = 0.49/\mathrm{T}^{-2}$. The signal contrast at $|\mathbf{H}| = +/- \, 0.5$ T is $\Delta\sigma \simeq 1.4$.

analysis of these results. Before doing so, however, I note that the fitting lines seem to systematically deviate from the data near $\mathbf{H} = 0$. My guess is that this comes from a combination of effects I discussed in Chapter 3, including some amount of In shielding (these devices *did* have In contacts!), being unable to sweep the field continuously through $\mathbf{H} = 0$, and field inhomogeneities across the DIP header effecting each device differently. In any case, my conclusions are independent of these discrepancies.

143
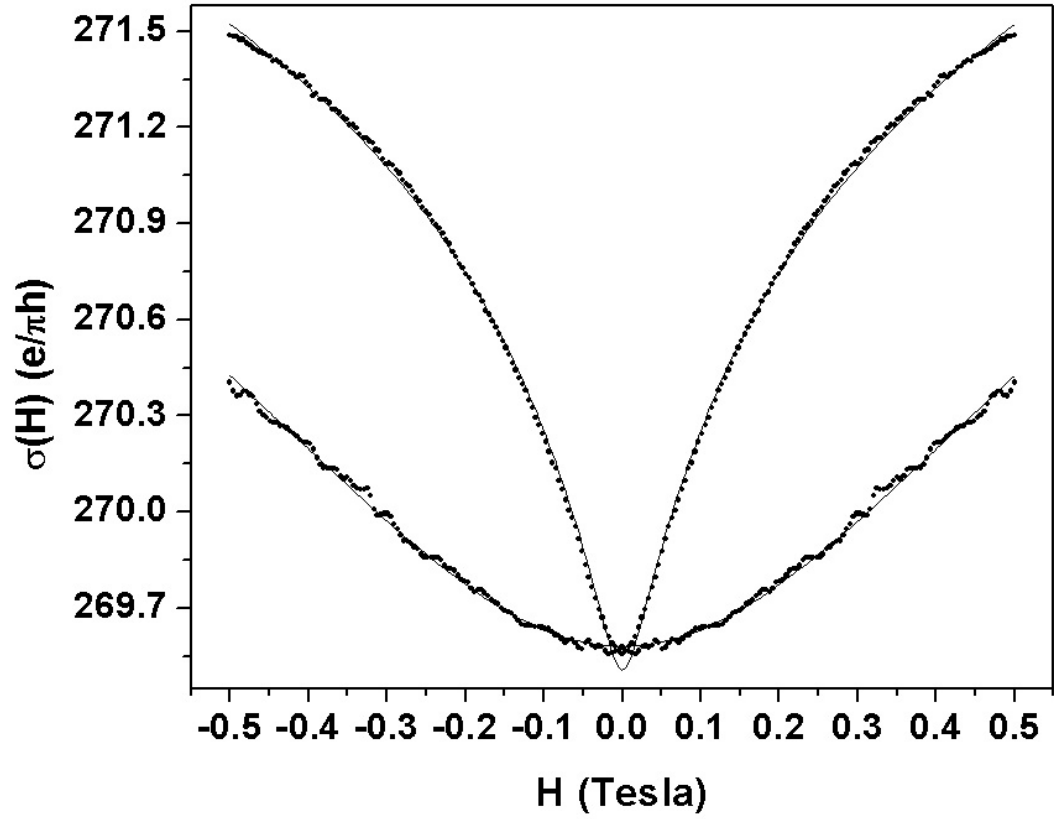
Figure 5.4: Cook 5 weak localization data. The best-fit parameters are $\ell_e = 33$ nm, $\ell_\phi = 117$ nm, and $\gamma = 5.31/\text{T}^{-2}$. The signal contrast $\Delta\sigma \simeq 1.1$.
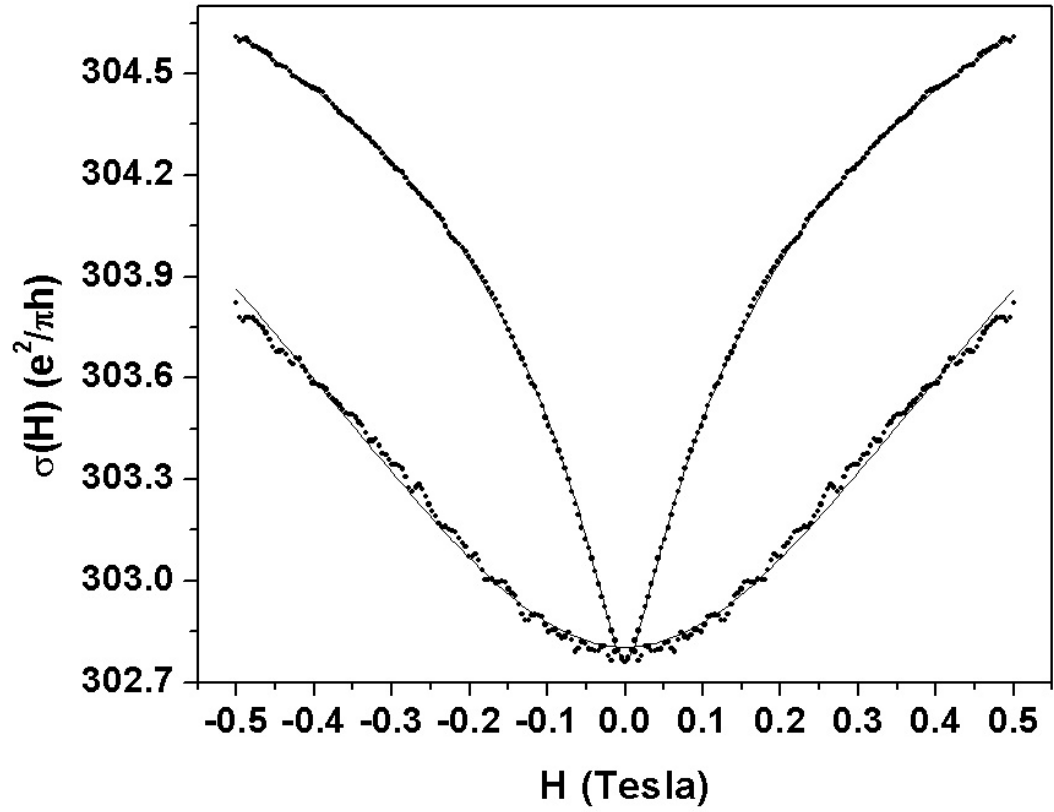
Figure 5.5: Cook 10 weak localization data. The best-fit parameters are $\ell_e = 37$ nm, $\ell_\phi = 124$ nm, and $\gamma = 7.54/\text{T}^{-2}$. The signal contrast $\Delta\sigma \simeq 0.8$.
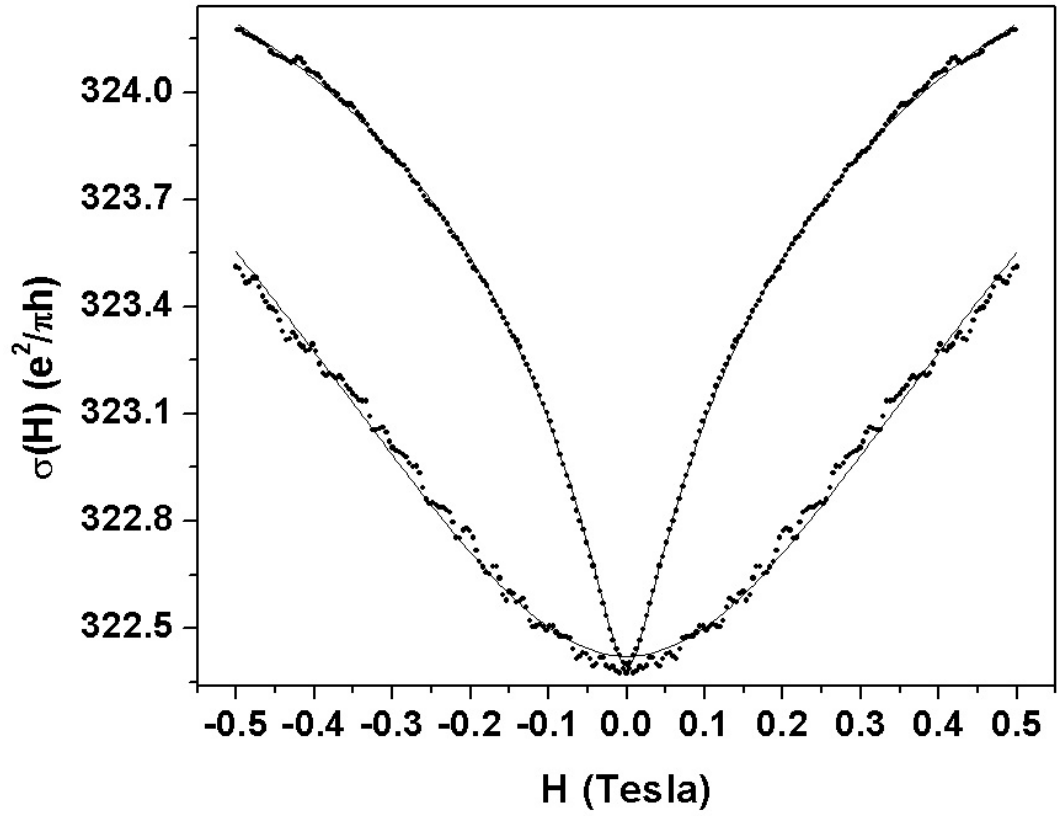
Figure 5.6: Cook 15 weak localization data. The best-fit parameters are $\ell_e = 38$ nm, $\ell_\phi = 127$ nm, and $\gamma = 11.25/\mathrm{T}^{-2}$. The signal contrast $\Delta\sigma \simeq 0.7$.

The best-fit parameters extracted from cook 0 through cook 15, along with their associated uncertainties, are shown in Table 5.1. Only the errors in ℓ_e and ℓ_ϕ (as determined by the corresponding fitting routines) are included, since these uncertainties dominate the corresponding error in $\mathcal{T}$. The mean square error in $\mathcal{T}$ was determined by "propagating" these errors in the usual way [83], given by

$$(\Delta \mathcal{T})^2 = \left(\frac{C^2}{4\ell_e \ell_\phi^2} \right)^2 (\Delta \ell_e)^2 + \left(\frac{C^2 \ell_e}{\ell_\phi^4} \right)^2 (\Delta \ell_\phi)^2 \tag{5.5}$$

where $C = (1/4\pi)^{1/4}(\hbar/e)\sqrt{\gamma/\ell_c}$.

Examination of Table 5.1 shows several trends, which I shall interpret by considering the effect the anneal had on the samples. I will primarily discuss lattice-type defects (e.g. vacancies and interstitials), since it is well-known that the quality of the Si crystal improves with annealing time, Δt, and therefore that these defects are reduced, or "cooked out", with annealing [20].

First, I note that ρ monotonically decreases with Δt. Since this number is formed by the ratio of two directly measurable physical quantities ($\rho \sim \mathrm{V/I}$), it does not hinge on any particular model for interpretation. The fact that ρ decreases with Δt is easily understood, since the scattering of electrons off defects is the origin of resistivity in the first place, and annealing removes defects. Similar considerations will be invoked when discussing the mean free path, ℓ_e.

No such monotonic trend is observed with n. However, if one arbitrarily (for the time being) ignores the cook 5 data point, n does become a

monotonically increasing function of Δt. The reason for pointing this out is that previous measurements, not presented in this thesis, demonstrated this effect very clearly, and it is in fact quite common; see [84], for example. Such behavior has to do with the notion of *electrical activation*, which essentially asserts that even if a P donor is placed in the crystal, it does not necessarily contribute an electron to the conduction band. This phenomenon may come about due to donors "clustering" about one another during epitaxial growth, with some type of molecular bonding acting to confine the electrons, or perhaps another cause related to defects "trapping" the electrons. Whatever the origin may be, these effects are small ($< 10\%$), which supports the assumption that the wafer was quite homogeneous.

The mean free path, ℓ_e, steadily increases with Δt. Essentially the same argument as was used for ρ applies here. As the density of defects is reduced, so are the number of scattering sites which disrupt an electronic trajectory as it propagates through the crystal. The average distance traveled by an electron between scattering events is ℓ_e, so again this result is intuitively appealing.

Perhaps the most interesting result in Table 5.1 is the trend the of the dephasing length, ℓ_ϕ, to increase with Δt. Recall that ℓ_ϕ is the mean distance an electron can travel through a sample before its phase coherence is destroyed, such as occurs during an inelastic scattering event. The previous arguments related to the defect density require a "renormalization",

Table 5.1: Experimental results for δ-layer devices annealed ("cooked") at 850 °C for intervals of 0 to 15 minutes. The parameters ℓ_e and ℓ_ϕ were extracted from fits to equation (5.2), γ from fits to equation (5.3). The mean-square thickness of a given δ-layer was estimated using equation (5.4), and is proportional to the parallel field parameter γ. The dominant contribution to the error in $\mathcal{T}$ comes from ℓ_e.

sample	resistivity ρ	electron density n	mean free path ℓ_e	dephasing length ℓ_ϕ	γ	rms thickness $\mathcal{T}$
	$\Omega/\square$	$10^{14}/cm^2$	nm	nm	Tesla^{-2}	nm
cook 0	428.6	1.40	30 +/- 13	101 +/- 3	0.49	14 +/- 3
cook 5	300.9	1.39	33 +/- 14	117 +/- 11	5.31	42 +/- 10
cook 10	267.9	1.42	37 +/- 13	124 +/- 3	7.54	51 +/- 9
cook 15	251.6	1.49	38 +/- 14	127 +/- 9	11.25	61 +/- 12

so to speak, since the static lattice defects I have been discussing do *not* alter the electron's energy in the course of a scattering event, only its momentum. Therefore understanding this result requires more elaborate considerations.

As mentioned in Chapter 2, the electron-electron interaction is expected to be the dominant dephasing mechanism in Si:P δ-doped samples (data supporting this assertion will be presented shortly). Theoretical work by various authors [39, 40] has shown that the electron-electron interaction is *enhanced* by disorder. In brief, the explanation for this enhancement is that defects disrupt the translational symmetry of the lattice, resulting in a reduction of conserved momentum. This in turn increases the rate of inelastic scattering, and thus the increase of ℓ_ϕ with Δt can be interpreted as a manifestation of this disorder enhanced effect at work. This observation could lead to an interesting series of experiments exploring such behavior, possibly incorporating crystallographic x-ray data to quantify the defect density.

The parallel field parameter, γ, also steadily increases with Δt. Given the relation between γ and the expression for $\mathcal{T}$ in equation (5.4), i.e. that $\mathcal{T} \sim \sqrt{\gamma}$, such behavior is anticipated. This leads us to consider the final column in Table 5.1, $\mathcal{T}$ itself.

As expected, $\mathcal{T}$ is a monotonically increasing function of Δt. This result is consistent with thermal diffusion of the δ-layer induced by the anneals. To check this, I employ a simple model of the data to estimate the diffusion

coefficient of Si:P at T = 850 °C. These are standard results, see Shewmon [85], for example.

Diffusion Model

From an atomistic point of view, as an Si:P sample is heated, each particle in the crystal acquires an rms thermal energy of order $k_B T$ (Boltzmann's constant $k_B = 1.38 \times 10^{-23}$ J/T). If the temperature is raised sufficiently high, the atoms become mobile, and perform three-dimensional "random walks" throughout the lattice. By considering the system's entropy it is clear that if diffusion is allowed to proceed indefinitely, the steady-state solution will be one of complete homogeneity. That is, if there are N_P phosphorous atoms in a sample of crystal with total volume V, then, after diffusing for a sufficiently long time, locating a small volume with a density appreciably different from N_P/V "almost never" happens (in the sense of Poincaré cycles and ergodic theory). So the δ-layer gets wider after annealing, with probability 1. Assuming isotropic diffusion (which is the case for P in Si [20]), these three-dimensional random walks can be factored into the product of three, one-dimensional random walks. Therefore, I now show how one-dimensional random walks can be used to model the results for $\mathcal{T}(\Delta t)$ in Table 5.1.

I start by considering a single P atom located at the origin (z = 0), and assume that it undergoes a one-dimensional random walk for a time Δt.

Then the probability that after this time the atom lies in the infinitesimal interval (z, z + dz) is given by P(z, Δt)dz, where P(z, Δt) is the Gaussian expression [86]

$$P(z, \Delta t) = \frac{exp(\frac{-z^2}{4D\Delta t})}{\sqrt{4\pi D\Delta t}}. \tag{5.6}$$

Here D is the *diffusion coefficient* characterizing the random walk. Note that P(z, Δt) is a normalized probability density ($\int_{-\infty}^{\infty}$P(z, Δt)dz = 1), and satisfies the one-dimensional diffusion equation [87]

$$\frac{\partial P(z, \Delta t)}{\partial t} = D\frac{\partial^2 P(z, \Delta t)}{\partial z^2} \tag{5.7}$$

both of which are essentially mathematical statements that the dopant atoms are conserved during the process of diffusion.

The mean square displacement, $<z^2>$, an atom undergoes from its original (z = 0) position is given by

$$< z^2 >= \int_{-\infty}^{\infty} z^2 P(z, \Delta t)dz \tag{5.8}$$

which yields $<z^2>$ = 2DΔt. This relationship will be used subsequently to define the diffusion length, L_D. If I assume a Gaussian-distributed δ-layer with initial *square* thickness $\mathcal{T}_0^2$, the effect of annealing is to simply add $<z^2>$ to the distribution (since these are two *independent* Gaussians [88]). Thus a new Gaussian δ-layer is produced, with square thickness $\mathcal{T}^2$ related to $\mathcal{T}_0$, D and Δt as

$$\mathcal{T}^2 = \mathcal{T}_0^2 + 2D\Delta t. \tag{5.9}$$

According to (5.9), if $\mathcal{T}^2$ is plotted versus Δt, a *linear relation* should be

152

observed, with slope 2D and intercept $\mathcal{T}_0^2$. Such a plot is shown in Figure 5.7, with the cook 0 data point omitted from the linear fit. The reason for the omission is that the initial rapid increase in $\mathcal{T}$ observed between cook 0 and cook 5 likely corresponds to an enhanced diffusion due to the defects, as mentioned earlier. As Δt is increased, the defects are cooked out, the curve "settles down" from this initial effect, and an accurate estimate of D can be obtained. Fitting a line to the *annealed* data points, I obtain a slope of 186 nm^2/min, which converts to $D = 3.1x10^{-14}$ cm^2/s in conventional diffusivity units.

A legitimate question at this point is to ask how well this data agrees with other measurements of D in Si:P? This is somewhat difficult to quantify, since diffusivity is heavily dependent on the techniques incorporated during sample preparation, and the interpretation of these weak localization results is of course model-dependent. A fairly recent treatment using SIMS analysis [89] claims $D = 4.14x10^{-16}$ cm^2/s, while values of D over two orders of magnitude higher than this are cited in [90]. Given this spread in values, it is clear that when quoting a measured value for D, more is required than simply specifying the temperature. Therefore I conclude that my work [79] is in accord with other published results, and that weak localization in parallel fields can be used for measurement of D.

Before I can unambiguously assert that this technique is better than SIMS for measuring $\mathcal{T}$ in δ-layers, however, a discussion of the systematic errors
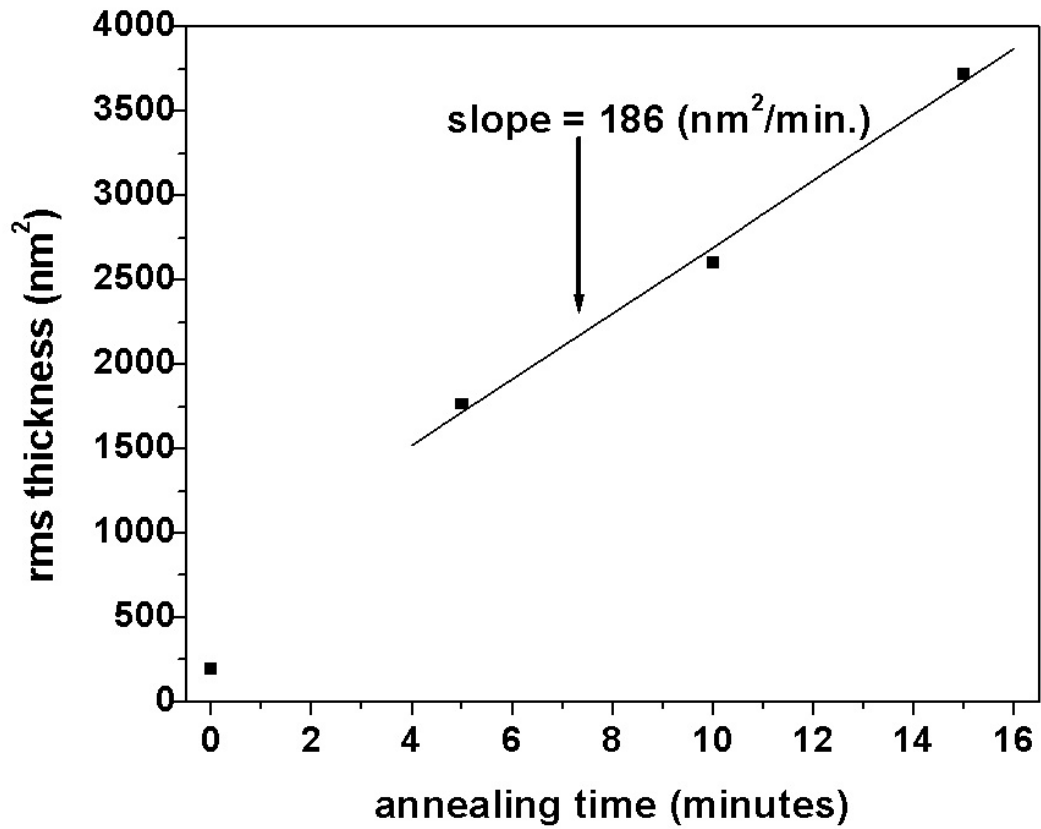
Figure 5.7: Diffusion coefficient data. The slope of the line yields D = 3.1×10^{-14} cm^2/s. Note that the intercept of the line lies well above the cook 0 data point, which has been omitted from the fit. This is consistent with transient enhanced diffusion in the annealed devices, as discussed in the text.

associated with this approach is necessary. The two categories I will explore are errors associated with the experimental techniques themselves, and those with the theoretical approach I have taken to interpreting the data.

Experimental Systematic Errors

Several issues with regard to the experimental procedures described previously require a more in-depth analysis to establish that this approach is on a sound footing. Since the systematic errors associated with the resistance measurements were discussed in Chapter 4, I will primarily concentrate on issues pertinent to the samples themselves. These include variances intrinsic to the wafer, non-uniformities in the devices due to unintended processing differences, and artifacts associated with the annealing procedure. Although this list is far from exhaustive, it seems likely that these issues dominate the systematic errors involved in this diffusivity study. At this point it should also be mentioned that the techniques associated with magnetic field application cited in [80] are probably better than those used in this work. The authors of [80] were able to apply $\mathbf{H}_\perp$ and $\mathbf{H}_\parallel$ independently and simultaneously, while I was only able to rotate the tilt stage to some fixed angle θ and then vary $|\mathbf{H}|$. Although the two approaches should be equivalent, the flexibilty of controlling two fields independently would have been preferable.

A thorough investigation into the uniformity of the wafer used for these

measurements was not carried out, but there are several reasons to discount this as a significant source of error. First, the pieces of the wafer used to construct the devices were taken from the same part of the wafer, near the center. As discussed in Chapter 3, the wafer is rotated during epitaxial growth in an effort to eliminate the type of non-uniformities I am considering here. Thus, one would expect that variance in the doping density would appear as a *radial* effect. Since the center of the wafer was essentially at rest during growth, this area should be the most uniform on the entire sample. Second, as shown in Table 5.1, even after the anneals, the density was found to vary by less than 10% from sample to sample. As discussed earlier, given the psuedo-trend of n increasing with Δt and the phenomenon of electrical activation, it seems quite likely that the variance in n was due to the anneals, not intrinsic anomalies in the wafer. Third, given that $\mathcal{T}$ increased from cook 0 through cook 15 precisely as expected, there is little reason for believing that this effect was from some bizarre coincidence in the wafer precisely corresponding to the annealing time of the device. In short, the data shown in Table 5.1, taken as a whole, essentially eliminates the possibilty that the observations presented here were due to non-uniformities in the wafer.

Undoubtedly, some part of the observed results were due to unequal processing techniques among the devices. Small differences in device features would lead to a corresponding change in the associated 4-wire measurements. A trivial example is that the farther apart two voltage contacts are spaced,

156

the larger is the resistance between them. Using the same device for the entire series of experiements would eliminate such issues, but was not the method followed here, for two reasons. One was prior experience with this "recycling" approach. To subject the same device to multiple anneals requires the electrical contacts to be removed and re-established each time. The way this was accomplished originally was by using In solder to make contact directly to the δ-layer, and removing the In by soaking the device in a room-temperature HCl bath. However, as discussed in Chapter 4, In, being a superconductor, expels magnetic flux from its interior when immersed in a field $|\mathbf{H}| < \mathbf{H}_c$. For In, $\mathbf{H}_c = 293$ gauss. This unwanted superconducting behavior would manifest itself by shielding portions of the device from the applied field for $|\mathbf{H}| < \mathbf{H}_c$, an example of which was shown in Figure 4.15. In light of this, one of the main experimental lessons of this work is that the use of superconductors should be assiduously avoided when performing weak localization measurements. The small amounts of In I used for wiring apparently had little to no effect.

No such "discontinuities" were observed when samples using Au-Sb contacts were measured. However, these contacts were "annealed in" (step 24, Chapter 3), and therefore essentially permanent. Furthermore, at T = 850 °C, it is a bad idea to anneal Au in Si, given gold's large diffusivity in Si and the associated trap states in the middle of the Si energy gap [91], which wreak havoc with proper measurements. The second reason for measuring

separate devices was mentioned earlier: working with a dilution refrigerator takes time, and instead of doing 4 cooldowns to obtain the data in [79], one (long) cooldown using van der Pauw devices was sufficient.

My own belief is that such device-dependent effects are *irrelevant* to the conclusions which I have drawn from these measurements. The reasons for this are twofold: the use of the symmetrization procedure and the van der Pauw theorem. As discussed in [68], all 4-wire measurements are a mixture of the symmetric and antisymmetric components of the conductivity tensor. By symmetrizing the data, one automatically obtains the symmetric component of the magnetoresistance, which is precisely what the weak localization correction to the conductivity, equation (5.2), is calculated for. In addition, no matter how convoluted a devices geometry, van der Pauw's theorem allows one to calculate the associated resistivity, again the pertinent quantity for the weak localization correction. That is, the theorem relates the resistance measured in a *given configuration* to the sample's intrinsic resistivity by a single number, appropriate to that particular device. Once the two appropriate, lead-switching van der Pauw measurements have been performed and ρ determined via equation (4.6), any other measured resistance is simply renormalized to equal ρ. Thus, for arbitrarily shaped samples the appropriate correction factor is easily calculated (as described in Chapter 4). Finally, since the data will ultimately be used with a least-squares fitting routine, this factor can be further optimized by making

it into a fitting parameter and finding the best fit. Since a single number multiplies all magnetoresistance data, the legitimacy of the procedure should be clear.

An issue I have glossed over in the above argument is the role the voltage probes play in the measurements. Probes will always be invasive, to some degree influencing the data. My guess is that as long as the contacts are sufficiently "point-like", the above arguments should hold. Point-like essentially means that the spatial extent of the probes should be small compared to the perimeter of the device (the effect of a contact with finite extent was discussed by van der Pauw [72]). Although potentially interesting and useful, a study of the effect of probe size on weak localization data was not carried out in this work. In any case, inspection of the lithographically defined devices throughout the fabrication process indicated samples which were highly uniform. Thus I assert that device-dependent differences are insignificant to the results in Table 5.1 when compared with the effect of annealing.

The systematics of the annealing procedure will be the final experimental errors I consider. Both the temperature and cooking times introduce errors into the results, and this is most likely the dominant error contribution to the estimate of the diffusivity.

For Si:P, the well-established relationship between the diffusion coefficient

and temperature takes the Arrhenius form [85, 89]

$$D(T) = D_0 exp\left(\frac{-\Phi}{k_B T}\right),\tag{5.10}$$

where D_0 is a constant (with diffusivity units of cm^2/s) and Φ is the activation energy (also constant). This exponential dependence on temperature is the primary culprit for the experimental systematic errors in my measurements. To see this, consider the plot in Figure 5.8, which depicts an idealized annealing process. After being loaded in the furnace, the sample temperature is "ramped up" linearly to the desired maximum temperature T_M (850 °C here), "dwells" at T_M for the desired time Δt, and is then symmetrically ramped back down to room temperature. However, diffusion happens not only during the cooking step proper (the rectangular area below T_M in Figure 5.8) but also as the temperature is ramped up and down (triangular areas). The obvious geometric picture is that the total (square) diffusion length induced by the annealing process is the sum of these three areas (really, a trapezoid), and therefore that the actual diffusion in the cooked devices is *larger* than quoted in [79], which neglected the contribution of the ramps. This dependence on the ramps will be represented by writing the total induced diffusion length as

$$L_D^2 = L_\square^2 + 2L_\triangle^2,\tag{5.11}$$

where $L_\square^2$ corresponds to the diffusion during the dwell time Δt, and $L_\triangle^2$ to the contribution of the ramps. Since the temperature profile is assumed to be symmetric, $2L_\triangle^2$ must be included in L_D^2.

160
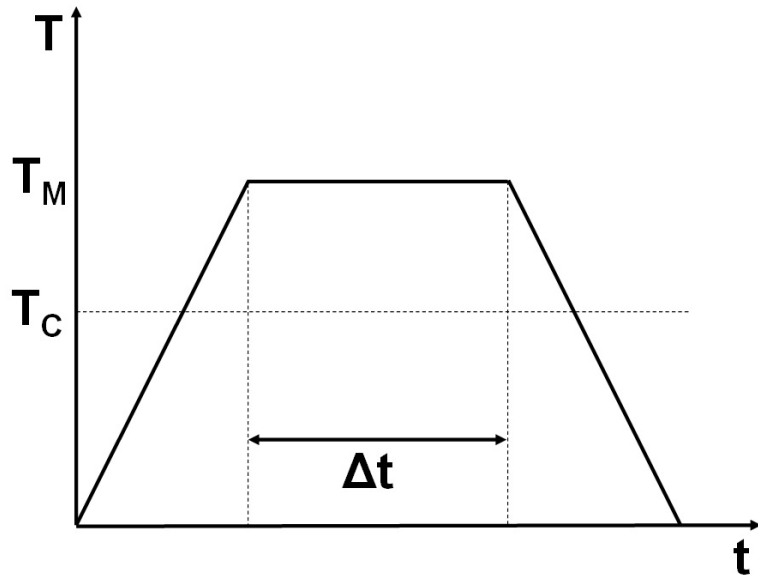
Figure 5.8: Model of annealing procedure. Although the diffusion was only intended to occur for the cooking time Δt at temperature T_M, diffusion actually occurs throughout the ramping process while $T \geq T_C$. The magnitude of this error is calculated in the text.

To estimate the magnitude of this accounting error, I will assume that whenever the sample's temperature is above a critical temperature T_C (arbitrarily defined), D obeys equation (5.10), while below T_C, D is identically 0. In order to calculate the relevant quantities of interest, Hadara's result that $D = (1.71 \text{x} 10^{-3}) \exp(-2.81 \text{ eV}/k_B T) \text{ cm}^2/\text{s}$ will be used [89], although it should be stressed that sample preparation methods are often as important as the annealing times and temperatures themselves, and the use of this D is only meant to give an estimate of the error. In fact, this probably sets a *lower bound* on the error, given the disparity between the estimates of D reported in [89] and [79]. Once again being somewhat arbitrary, I ignore values of D for which the diffusivity is less than 1/100 of D at 850 ° C, which leads to $T_C \simeq 700$ °C.

For a variable D, the diffusion length $L_\triangle^2$ must be weighted by an integral over the product of the diffusion coefficient and the infinitesimal time dt [85]:

$$L_\triangle^2 = 2 \int_0^\tau D(T) dt = 2 D_0 \int_0^\tau exp\left(\frac{-\Phi}{k_B T}\right) dt. \qquad (5.12)$$

τ is the time interval over which D varies. The exponential dependence on 1/T in this integral requires invoking the incomplete gamma function to obtain a closed form solution, and since this is expressed yet again in terms of an integral, provides little physical insight to the problem. Instead, I have calculated the integral numerically by partitioning the domain of integration into a finite number of subintervals, calculating the corresponding diffusion length for each of these elements, and summing the results to approximate

$L_\triangle^2$. Carrying out this computation with a 180 element partition (one for each second of the ramp between 700 and 850 °C), I obtain $L_\triangle^2 = 3.7$ nm^2. Therefore, assuming a symmetric ramp profile, the total contribution of the ramps to $L_\square^2$ is $2L_\triangle^2$, or 7.4 nm^2.

Since all of the devices studied used the same ramp profile but different dwell times, the error introduced by $L_\triangle^2$ is larger for shorter anneals. This is clear by forming the ratio $L_\triangle^2/L_\square^2$ for each device, for which one obtains 0.297 for cook 5, 0.149 for cook 10, and 0.099 for cook 15. Thus, the $L_\triangle^2$ error is clearly a non-trivial contribution, especially for cook 5, where the error is nearly 30 % of $L_\square^2$. To combat this effect, fast ramp profiles should be used, which would make the "annealing trapezoid" I have considered in this analysis more rectangular, and therefore closer to ideal. This also suggests that the resolution limits of the weak localization technique used here could be probed by subjecting the samples to very brief "heat pulses" (for example, in a rapid thermal annealer), whose duration is systematically reduced until the δ-layer broadening can no longer be resolved.

To consider the final aspects of the annealing process experimental errors, I take a much less quantitative approach than for the ramping effects. One issue is the fact that, in reality, the true temperature of the sample is *not* precisely known as it is cooked. No thermometer was near the sample to monitor the temperature, so effects such as "overshooting" T_M and fluctuating about T_M cannot be ruled out. The anneals were performed in a

Barnstead Thermaline 79300 tube furnace, whose total length was approximately 1 meter. Obviously there are substantial temperature gradients in such a processing tool, with the center presumably being hotter than the ends. Although every effort was made to place the samples in the exact center of the tube, this procedure was approximate at best, and thus one sample may have actually been annealed at a temperature slightly higher than 850 °C, another slightly below, etc. In addition, the ramp was not even symmetric, let alone trapezoidal in shape, since the ramp down from T_M always took longer than the ramp up. To stress the point one final time, since the diffusivity depends exponentially on $1/T$, these phenomena could have played a noticeable effect in the reported results, but a quantitative, systematic analysis of these points was not carried out.

Despite the considerations discussed here, the experimental results produced by these measurements, shown in Table 5.1 and discussed in detail subsequently, are quite convincing. In particular, the weak localization data in Figures 5.3 through 5.6, showing the signal contrast $\Delta\sigma$ in these samples monotonically decreasing with Δt, provides strong evidence that experimental systematic errors were *not* the primary limitation facing the interpretation of this data. The next section of this chapter is devoted to exploring the theoretical interpretation of this data, which we shall see *is* the limiting factor of this weak localization analysis.

Theoretical Systematic Errors

Although the weak localization data shown in Figures 5.3 through 5.6 was well fit by equations (5.2) and (5.3), alternatives to this are possible. For example, another common expression for $\delta\sigma(\mathbf{H}_\perp)$ which also produces good fits is [53]

$$\delta\sigma(H_\perp) = (\frac{e^2}{2\pi^2\hbar})[\Psi(\frac{1}{2} + \frac{\hbar}{4eH_\perp{\ell_\phi}^2}) - \ln(\frac{\hbar}{2eH_\perp\ell_e^2})] \qquad (5.13)$$

which can be obtained from equation (5.2) by replacing $\Psi(1/2 + \hbar/2\mathrm{eH}\ell_e^2)$ with its asymptotic form, the natural logarithm. More generally, one might want to take into account *all* types of scattering (electron-electron, electron-phonon, and electron spin interactions) and fit data using the full expression for the weak localization correction, equation (2.36), mentioned in Chapter 2. The point is that although there will be certain features common to all two-dimensional electron systems (such as the magnetoresistance being anisotropic), there will also be important differences particular to each, and a theory specific to weak localization in Si:P δ-layers including band structure effects, density dependence, etc., has yet to be developed. Because of this, the results shown in Table 5.1 have *theoretical* systematic errors associated with them, stemming from the use of imperfect modeling, and it is my assertion that these modeling limitations dominate the errors in this work.

I have identified several desiderata for a theoretical model of the weak localization correction $\delta\sigma(\mathbf{H})$ in Si:P δ-layers, which I shall write as $\delta\sigma(\mathrm{H},\theta)$ to emphasize the vectorial nature of the measurement (again, θ is the angle

between $\mathbf{H}$ and the current density $\mathbf{J}$; see Figure 4.5). In addition to being as specific as possible to the system under study (i.e. accounting for subband effects, etc.), these criteria include that $\delta\sigma(\mathrm{H},\theta)$ should be a continuous function of θ, have well-defined parameter regimes over which the theory applies, predict crossover behaviors, be consistent with previous results, and incorporate ℓ_c throughout the analysis, not merely for parallel fields. I shall touch on these points only briefly.

For purely physical reasons, if measurements are performed over a finite range of magnetic field (say $|\mathbf{H}|\in[-1,+1]$ T), $\delta\sigma(\mathrm{H},\theta)$ should be a *continuous function* of θ. Given a fixed $\mathbf{H} = \mathbf{H_0}$, the magnetoconductance is maximal for $\theta = \pi/2$, minimal for $\theta = 0$, and should monotonically decrease as θ is reduced from $\pi/2$ to 0. This behavior is shown in Figures 5.3 through 5.6. Thus far theoretical papers, especially [62], have addressed this point by decomposing $\mathbf{H}$ into components perpendicular ($\mathbf{H}_\perp = |\mathbf{H}|\sin(\theta)$) and parallel ($\mathbf{H}_\parallel = |\mathbf{H}|\cos(\theta)$) to the 2DEG, and *phenomenologically* introducing an additional dephasing rate due to the parallel field: $1/\tau_\parallel \sim 1/\mathrm{H}_\parallel^2$. Although phenomenology is acceptable and "on the right track", a first-principles theory would be preferable.

That well-defined parameter regimes and predictable crossover behaviors are lacking in the present work is demonstrated by the data shown in Figures 5.9 through 5.13 and the fitting results in Table 5.2. Figure 5.9 captures the essence of the point of view I advocate here. Although quite simple

166
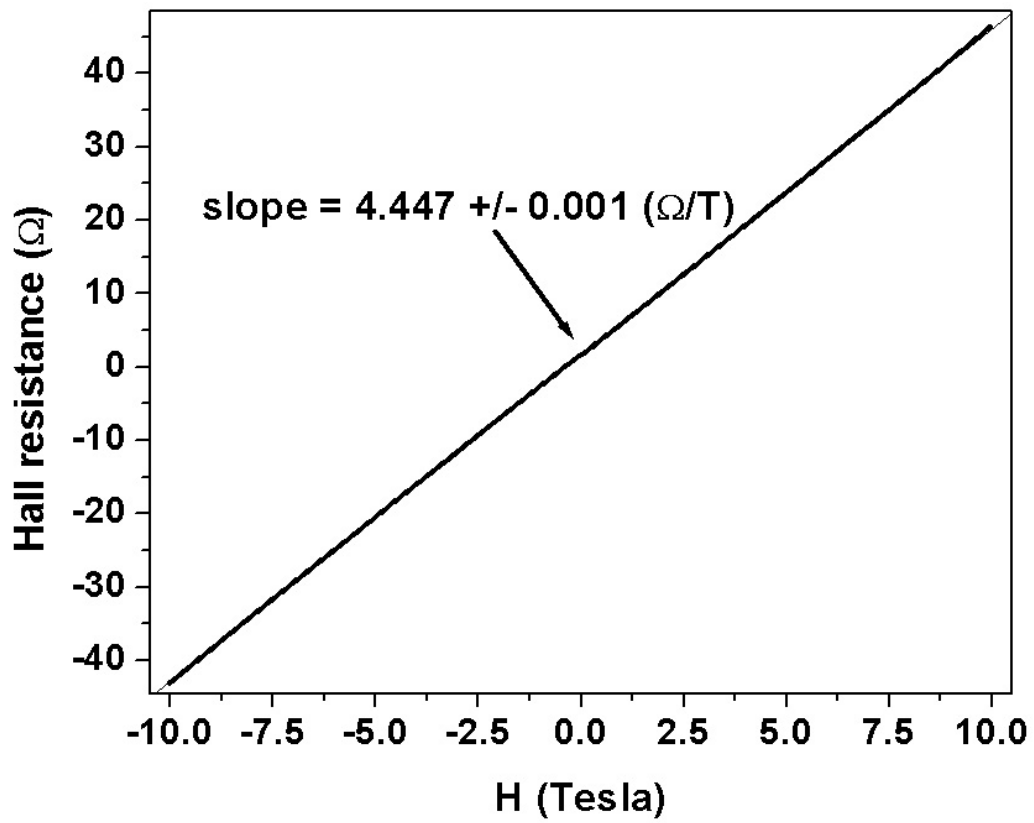
Figure 5.9: Large field Hall data for the cook 0 device. The slope yields a carrier density of n = $1.4x10^{14}/cm^2$.

(Appendix A), the Hall effect is an extremely accurate theory; the measured transverse magnetoresistance is highly linear over the entire accessible magnetic field range in these experiments. The same cannot be said of using equation (5.2) to fit the data shown in Figure 5.10. The longitudinal magnetoconductance shows an almost "resonant" behavior near $\mathbf{H} = 0$, but instead of $\delta\sigma(\mathbf{H}_\perp)$ asymptotically approaching $(2\mathrm{e}^2/\pi\mathrm{h})\ln(2\ell_\phi/\ell_e)$ as predicted by (5.2), the derivative $\mathrm{d}\sigma/\mathrm{d}\mathrm{H}$ instead changes sign near $\mathbf{H} \simeq 2$ T, and progressively decreases as the field magnitude is increased. This effect is likely due to the classical magnetoresistance (CM) contribution to the conductivity, a well-known phenomenon [2] wherein the resistance of a doped semiconductor increases like $|\mathbf{H}|^2$ for large $|\mathbf{H}|$. Such considerations have been omitted from the majority of weak localization analyses, and being able to predict when the CM begins to dominate based on ℓ_e, ℓ_ϕ, etc. would be extremely valuable for interpreting data.

With regard to a consistent theory of weak localization in Si:P δ-layers, Figures 5.11 and 5.13 immediately show several features that are necessary, namely characteristic magnetic field and temperature dependences. The graph in Figure 5.11 shows two measurements of the longitudinal resistance of a device as the temperature is reduced to the dilution refrigerator base temperature. The upper curve corresponds to zero applied magnetic field, the lower curve to a perpendicular field of 2 T. Except for an approximately constant offset, these two curves are nearly identical. Such behavior is
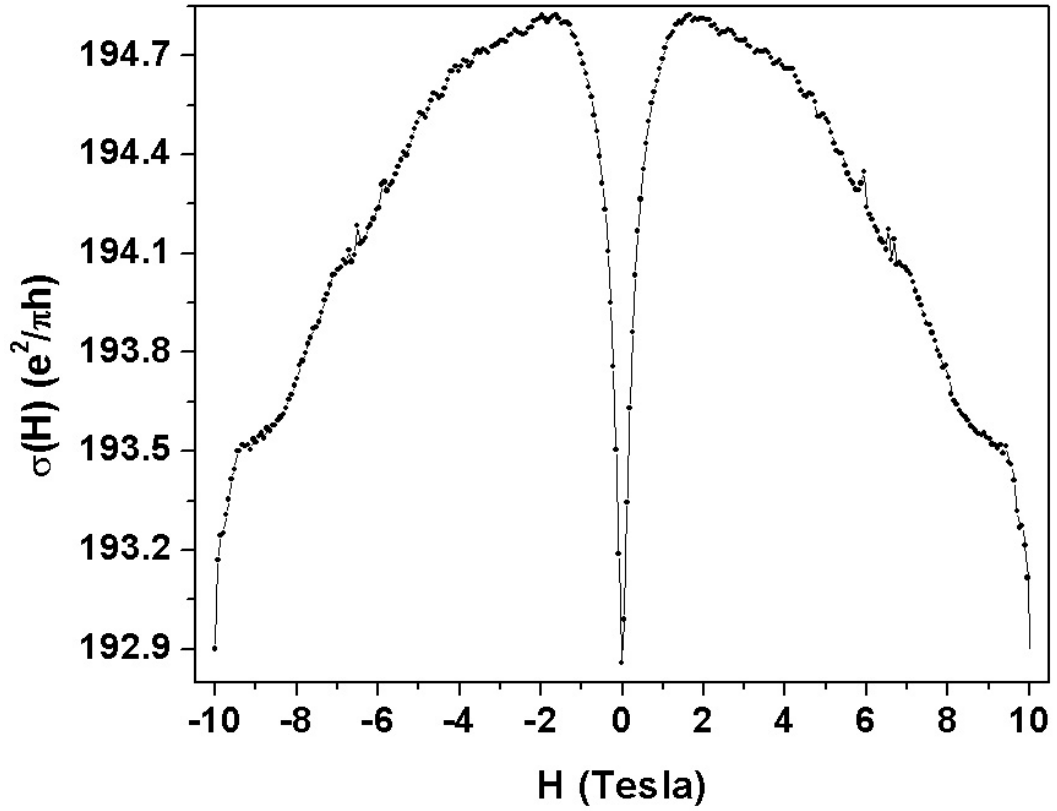
Figure 5.10: Large field weak localization data. The fact that $\sigma(\mathbf{H})$ is not a monotonically increasing function of $|\mathbf{H}|$ shows the limited validity of equation (5.2). The reduction in $\sigma(\mathbf{H})$ for $|\mathbf{H}| \geq 2$ T is likely due to classical magnetoresistance.

expected in a system where dephasing is dominated by the electron-electron interaction [40, 34] (a fit to the predicted logarithmic dependence on T is shown). Thus a theory of localization in these systems should from the beginning consider this interaction as the primary mechanism responsible for the magnetoconductance.

Turning to Figure 5.13, the measured change in resistance versus $\mathbf{H}_\perp$ is plotted for a sample at two fixed temperatures, T = 4.2 K and T = 130 mK (a complement of the data in Figure 5.11, where the temperature was varied and the field held constant). Since the width of this line shape gives a measure of the dephasing time (the sharper the curve, the longer the dephasing time), it is reasonable that the higher the temperature data displays a broader line shape (presumably in part due to phonon-induced dephasing). The canonical interpretation of these results is to argue that the dephasing time becomes infinite as T $\to$ 0 according to a power law, i.e. τ_ϕ $\sim 1/T^p$. However, if one looks closely at the data corresponding to the lowest temperatures of Figure 5.11, it is evident that the resistance *saturates* (ceases to change) for T $\leq$ 200 mK, implying a concurrent saturation of τ_ϕ. To make this saturation more apparent, the $\mathbf{H}$ = 2 T data is plotted on a logarithmic temperature scale in Figure 5.12. Such saturation behavior has been observed in all experimental weak localization studies thus far reported, and a possible explanation in terms of so-called intrinsic decoherence was advanced in [92]. The theoretical fervor which this prompted is still
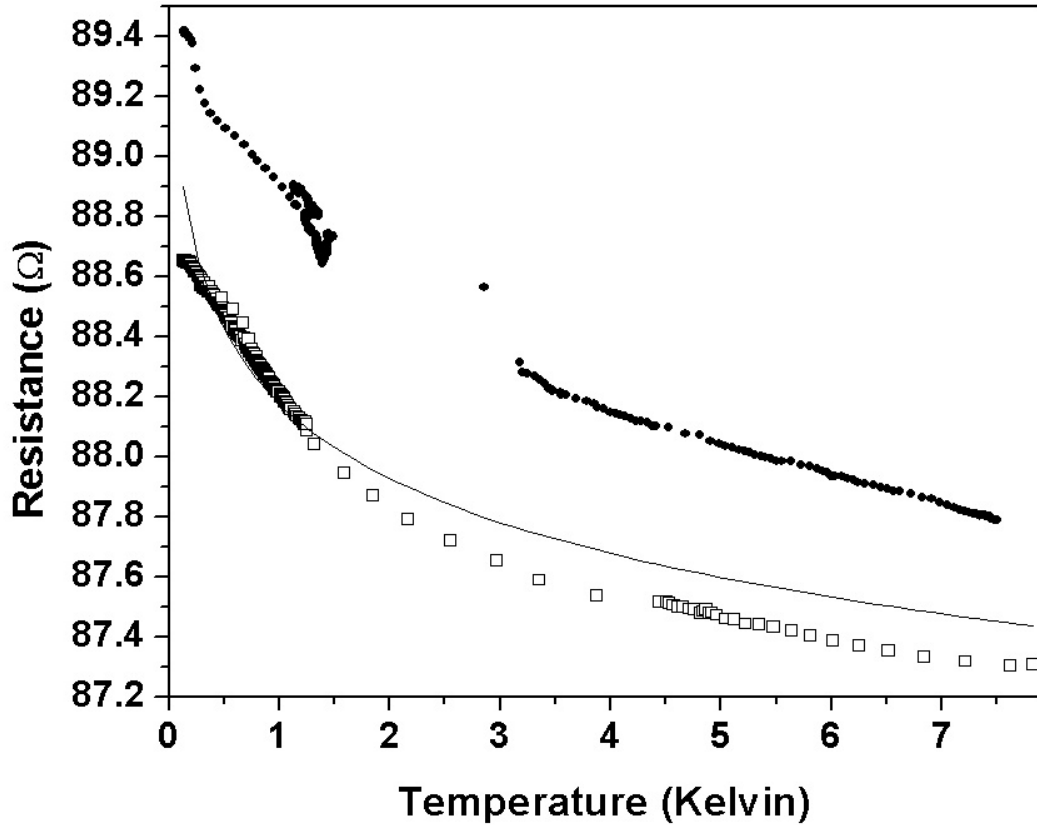
Figure 5.11: Temperature dependent data (constant field). The upper curve (solid points) was recorded with $|\mathbf{H}| = 0$, the lower curve (open squares) with $\mathbf{H} = 2$ T. The fact that the form of curve does not change with the large field applied demonstrates that the electron-electron interaction is responsible for the dephasing in Si:P δ-doped samples. The solid line is a fit to the equation $R(T) = R_0 + A\ln(BT)$, with values $R_0 = 88.1$ Ω, $A = -0.36$ Ω, and $B = 0.86$/K. The jumble of data points for $|\mathbf{H}| = 0$ near $T = 1$ K is due to the refrigerator "hanging up" (ceasing to cool continuously) at this point as mixture was circulated.

171
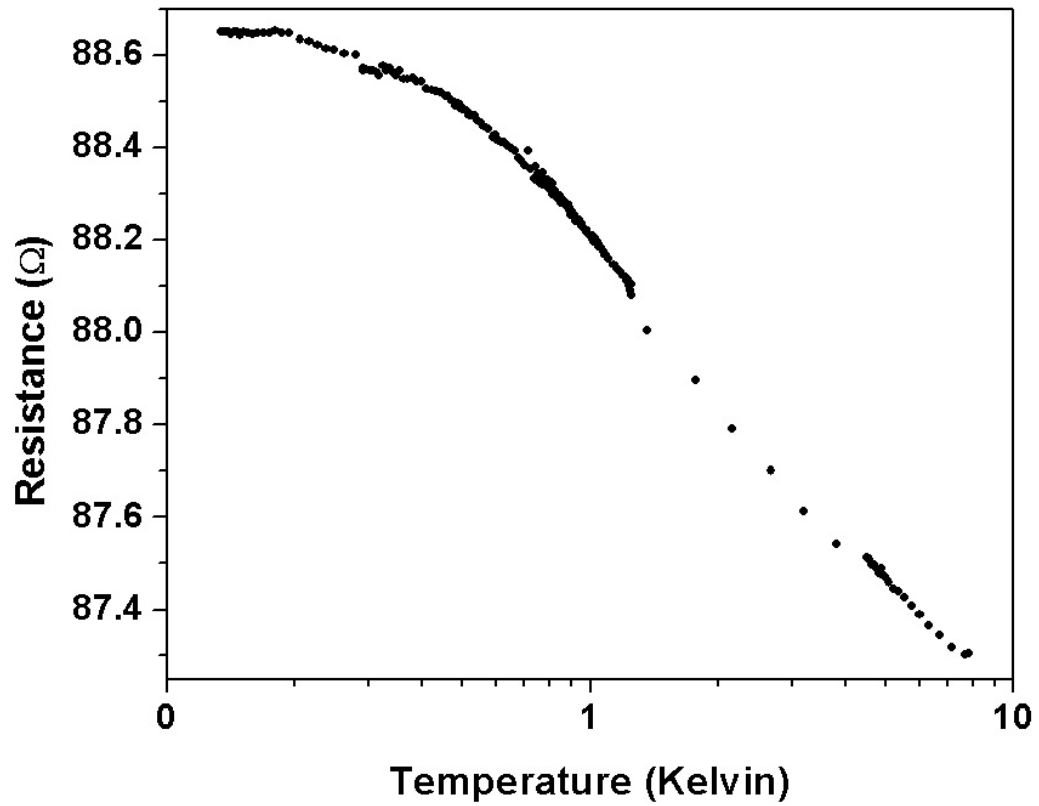
Figure 5.12: Data of Figure 5.11 plotted on a logarithmic temperature scale, highlighting the saturation of R(T) for T $\leq$ 200 mK.

unfolding at the time of this writing, and remains unresolved.

The final theoretical point I consider is the appropriate incorporation of the correlation length, ℓ_c, throughout the magnetoconductance analysis. Although the influence of ℓ_c on $\delta\sigma(\mathbf{H}_\parallel)$ has been considered at length in terms of estimating $\mathcal{T}$, the effect of ℓ_c on $\delta\sigma(\mathbf{H}_\perp)$ has been neglected. Obviously, since weak localization is ultimately reducible to the Aharanov-Bohm effect, and this is itself a manifestation of a geometric phase, the discussion of Chapter 2 makes it clear that the inclusion of ℓ_c in a calculation of $\delta\sigma(\mathbf{H}_\perp)$ is necessary for a complete theory. Furthermore, calculations for systems with multiple subbands, intersubband scattering, etc., should be undertaken for a better understanding of magnetotransport in δ-layers.

Without resorting to any particular model of the δ-layer thickness, a reasonable estimate of $\mathcal{T}$ in the cook 0 device can be obtained by considering the SIMS data of Figure 5.1 and the Hall data of Figure 5.9 (which yields n = $1.4\mathrm{x}10^{14}/\mathrm{cm}^2$). Since the SIMS data gives a three-dimensional P density versus depth in the sample, while the Hall data gives a two-dimensional electron density, *integration* of the SIMS profile produces a two-dimensional density. By starting at the peak of the SIMS profile and progressively stepping away from this point (symmetrically in either direction), the number of two-dimensional electrons in each infinitesimal interval is summed until the resultant two-dimensional density equals the measured Hall density,
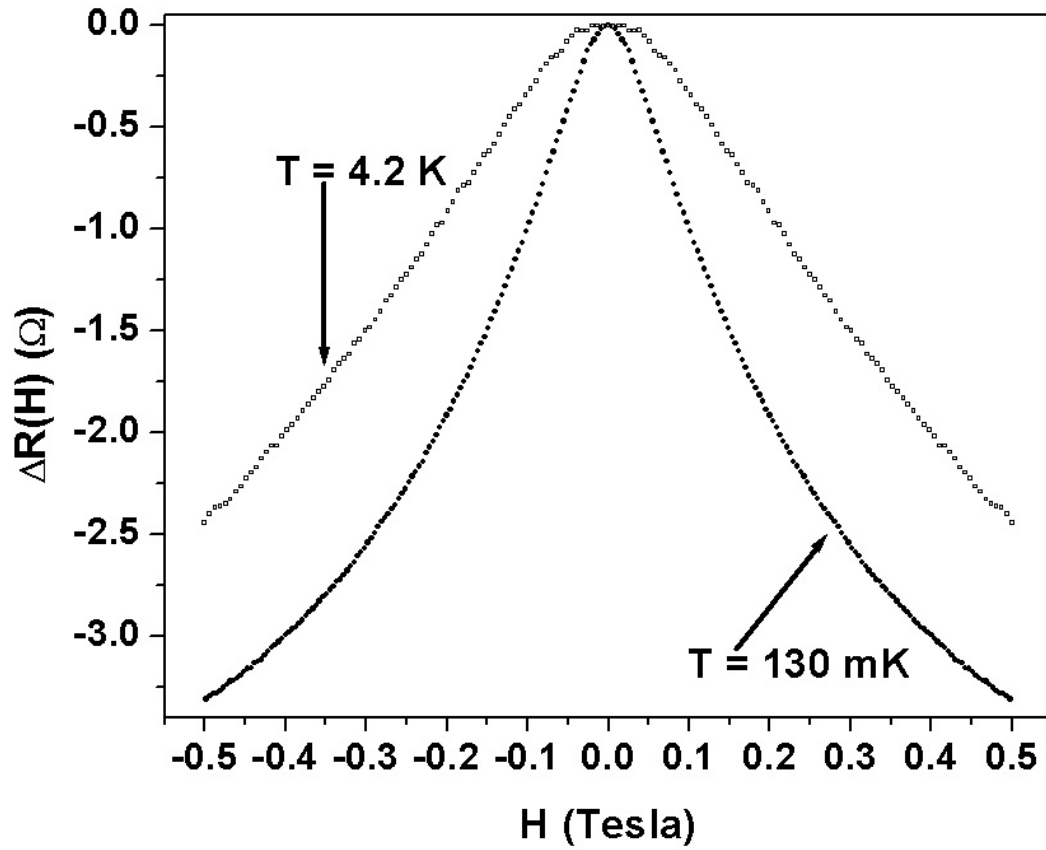
Figure 5.13: Temperature dependent weak localization data. The width of the line

shape is narrower at 130 mK, due to the logarithmic dependence of the dephasing

length on temperature: $\ell_\phi \sim \ln(T)$.

n. The MATLAB routine which carries out this computation is shown in Appendix B. The result, which I denote by $\mathcal{T}_\mathcal{S}$ (for "SIMS"), is $\mathcal{T}_\mathcal{S} = 7.5$ nm. This shall serve as an important benchmark for the theoretical models of $\mathcal{T}$ I consider below.

To obtain an order of magnitude estimate for how theoretical limitations influence the data analysis, consider the results displayed in Table 5.2. Shown are the best-fit results to equations (5.2) and (5.3) for data obtained from the cook 0 device as the fitting range of $|\mathbf{H}|$ is reduced from +/- 1 T to +/- 0.1 T. Also shown for each range are estimates for the δ-layer thickness in this device based on the "uncorrelated" ($\mathcal{T}$) and "correlated" ($\mathcal{T}_\mathcal{C}$) models discussed in Chapter 2. Several features are evident. First, the best-fit values of ℓ_ϕ steadily decrease as the range of $|\mathbf{H}|$ is reduced, and the same trend occurs for ℓ_e, although the variation in this case is much greater. Second, the best-fit values of γ are by contrast rather uniform, suggesting that equation (5.3) is a sufficiently accurate model for parallel field data. Lastly, the $\mathcal{T}$ and $\mathcal{T}_\mathcal{C}$ estimates are actually quite consistent ($\mathcal{T} = 2.3$ +/- 0.06 nm, $\mathcal{T}_\mathcal{C} = 15.8$ +/- 0.6 nm), *provided* one only considers ranges of $|\mathbf{H}| \geq 0.4$ T. For smaller ranges of $|\mathbf{H}|$, the parallel field magnetoconductance changes very little, and the fact that a negative value of γ was found for $|\mathbf{H}| \leq 0.1$ T is a consequence of the data being more noise than signal. Therefore, thickness estimates were excluded in this range.

Obviously, the average thickness of the donors in the sample is

Table 5.2: Dependence of the parameters ℓ_ϕ, ℓ_e, γ, and consequently $\mathcal{T}$, on magnetic field range used in fitting routine.

H limits T	ℓ_ϕ nm	ℓ_e nm	γ T^{-2}	$\mathcal{T}$ nm	$\mathcal{T}_c$ nm
+/- 1.0	103.2	41.1	0.455	2.2	15.9
+/- 0.9	102.2	39.9	0.467	2.2	16.1
+/- 0.8	101.2	38.6	0.483	2.3	16.2
+/- 0.7	100.2	37.0	0.492	2.3	16.2
+/- 0.6	99.3	35.0	0.488	2.3	15.8
+/- 0.5	98.6	33.2	0.493	2.3	15.6
+/- 0.4	97.8	29.9	0.47	2.3	14.6
+/- 0.3	96.7	3.3	0.37	2.1	4.3
+/- 0.2	96.7	3.0	0.02	0.5	1.0
+/- 0.1	92.7	4.1	-0.8	-	-

independent of the range of $|\mathbf{H}|$, so the less the fitting parameters vary with the $|\mathbf{H}|$ interval, the better. Given the enormous variance between the best-fit values of ℓ_e, it is clear that equation (5.2) does not provide a reliable estimate of this parameter. Ignoring this for the time being and using the result $\mathcal{T}_\mathcal{S} = 7.5$ nm, it seems that the "uncorrelated" thickness model ($\mathcal{T} = \hbar\sqrt{\gamma}/2\mathrm{e}\ell_\phi$) *underestimates* the δ-layer thickness by roughly a factor of 3.5, while the model corresponding to $\mathcal{T}_\mathcal{C}$ (equation (5.4)) *overestimates* the thickness by approximately a factor of 2. Even using the estimate for ℓ_e obtained from n and ρ (Appendix A), $\mathcal{T}_\mathcal{C} = 11.7$ nm, which is still nearly 60% larger than $\mathcal{T}_\mathcal{S}$.

What this analysis shows is that although the parallel field weak localization technique is in principle very powerful, and should ultimately prove to be more sensitive than SIMS, the theory necessary for interpretation of the data is still far from adequate for this purpose. Nevertheless, this work has provided a good starting point for further study.

5.1.2   Density Dependence

This subsection of my Si:P δ-layer study is concerned with how the considerations I have discussed depend on the carrier density, n. Originally my hope was to perform the perpendicular and parallel field weak localization measurements on Si:P samples with progressively larger sheet resistivities, apply the analysis previously described, and establish the

critical density (n_c) for the metal-insulator transition in two-dimensions. However, I was not able to carry this study to its conclusion, due to my inability to obtain appropriate samples.

SIMS data for one successfully measured sample is shown in Figure 5.14. This sample came from wafer "B" in Figure 2.10. The corresponding Hall data is shown in Figure 5.15 (the linear fit yields n = 6.5×10^{13}/cm^2) and the base temperature, zero-field resistivity was $\rho = 625$ $\Omega/\square$. The corresponding data for perpendicular and parallel field weak localization measurements is shown in Figure 5.16. The fitting parameters established for this device via equations (5.2) and (5.3) are $\ell_\phi = 94$ nm, $\ell_e = 28$ nm, and $\gamma = 1.12$/T^{-2}. As discussed earlier, a better estimate of $\ell_e = 20.4$ nm can be obtained by combining n and ρ as described in Appendix A. Using the uncorrelated estimate of the thickness, I obtain $\mathcal{T} = 4.3$ nm in this sample, while integration of the SIMS plot yields $\mathcal{T_S} = 20.8$ nm. I offer no explanation for this rather large discrepancy.

SIMS data from wafer "C" of Figure 2.10 is shown in Figure 5.17. Hall data for this sample is shown in Figure 5.18. The density in this device was n = 3.7×10^{13}/cm^2, the zero-field resistivity $\rho = 1063$ $\Omega/\square$, and combining these parameters yields $\ell_e = 15.9$ nm. The best-fit parameters for the corresponding weak localization data, shown in Figure 5.19, are $\ell_\phi = 81$ nm, $\gamma = 1.6$/T^2. Putting everything together, $\mathcal{T} = 5.1$ nm for this device, while integration of the SIMS profile yields $\mathcal{T_S} = 11.6$ nm.
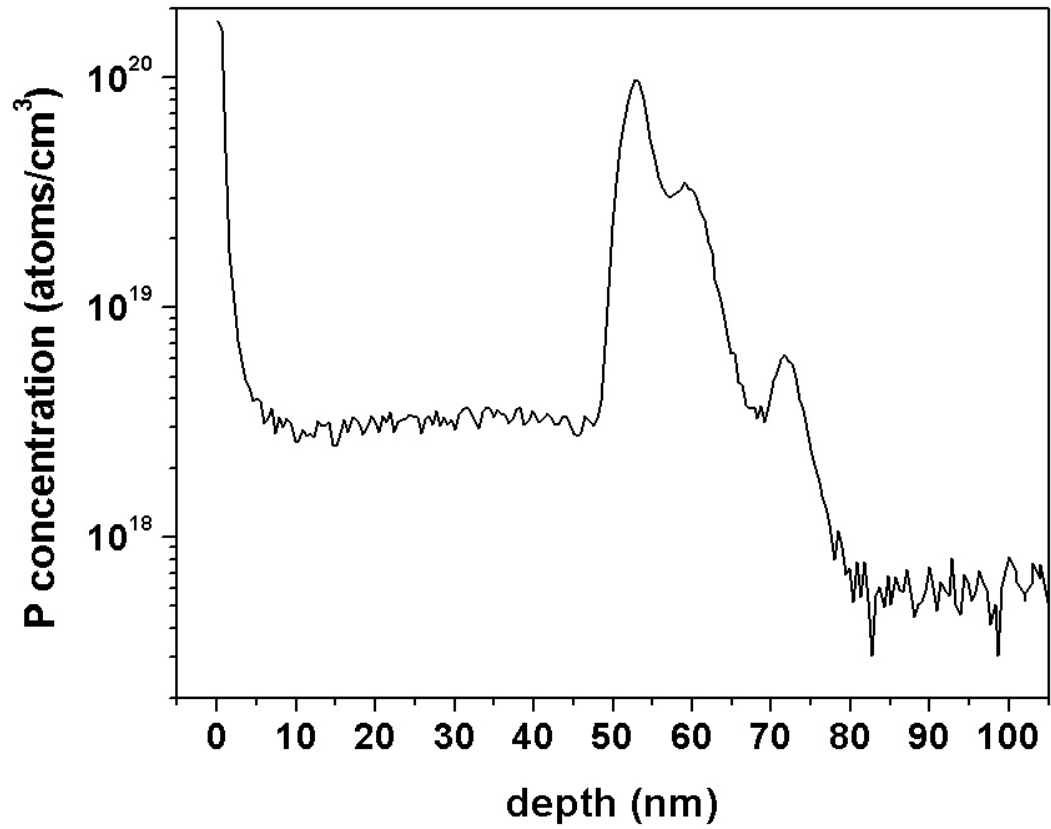
Figure 5.14: SIMS data from a sample of wafer B (see Figure 2.10).

slope = 9.641 +/- 0.003 (Ω/T)
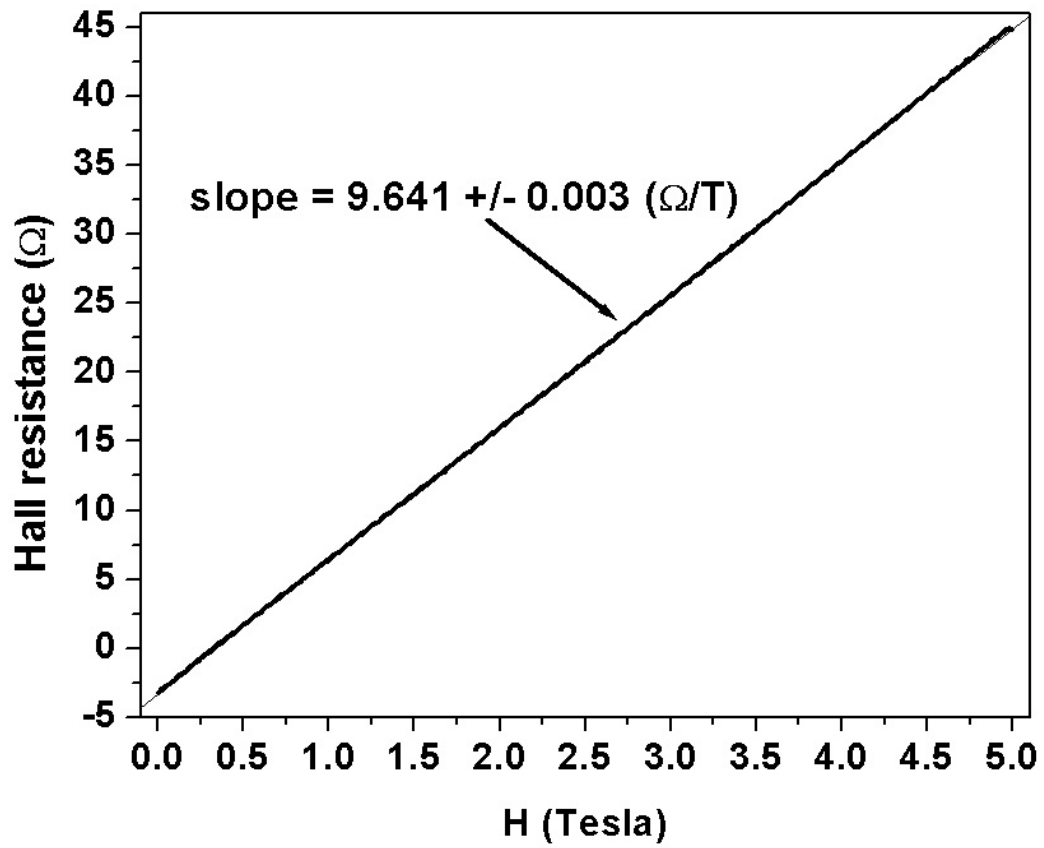
Figure 5.15: Hall data for a device fabricated from wafer B. The linear fit yields n

= $6.5 \times 10^{13}/cm^2$.
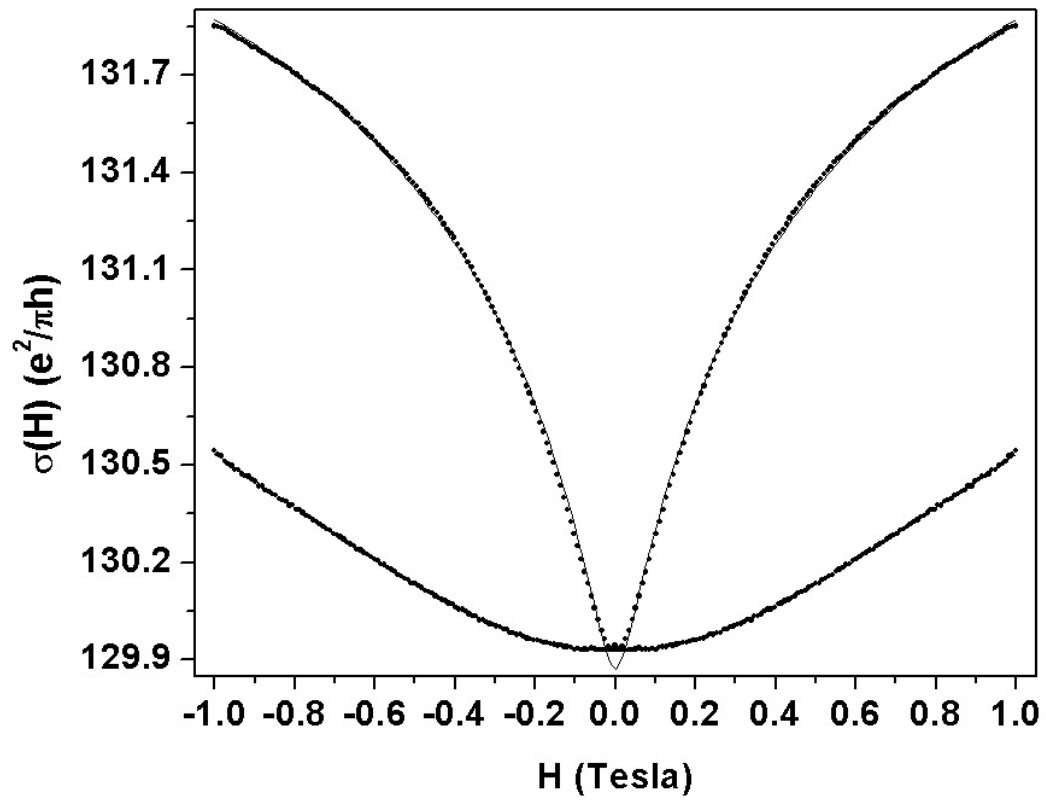
Figure 5.16: Weak localization data from the same device as the Hall data of Figure
5.15 (wafer B). The best-fit weak localization parameters for this device were $\ell_\phi =$
94 nm, $\gamma = 1.12/\mathrm{T}^2$.
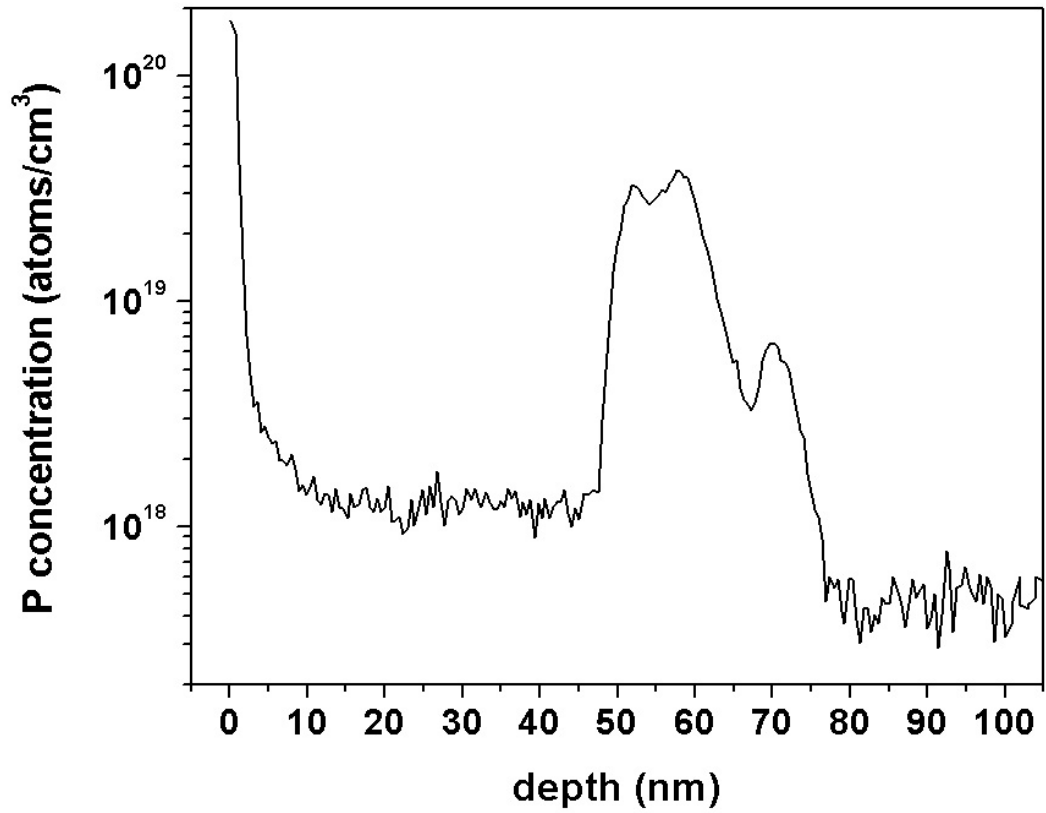
Figure 5.17: SIMS data from a sample of wafer C (see Figure 2.10)
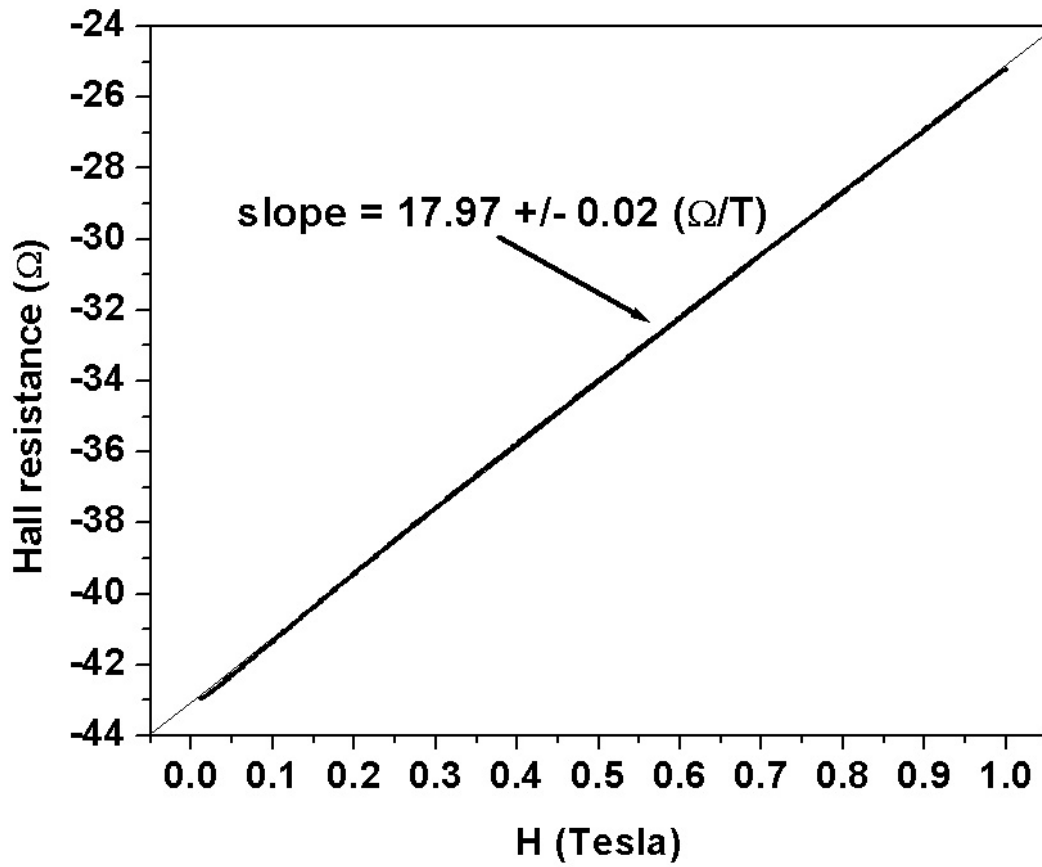
Figure 5.18: Hall data for a device fabricated from wafer C. The linear fit yields n = $3.7 \times 10^{13}/cm^2$ in this device.
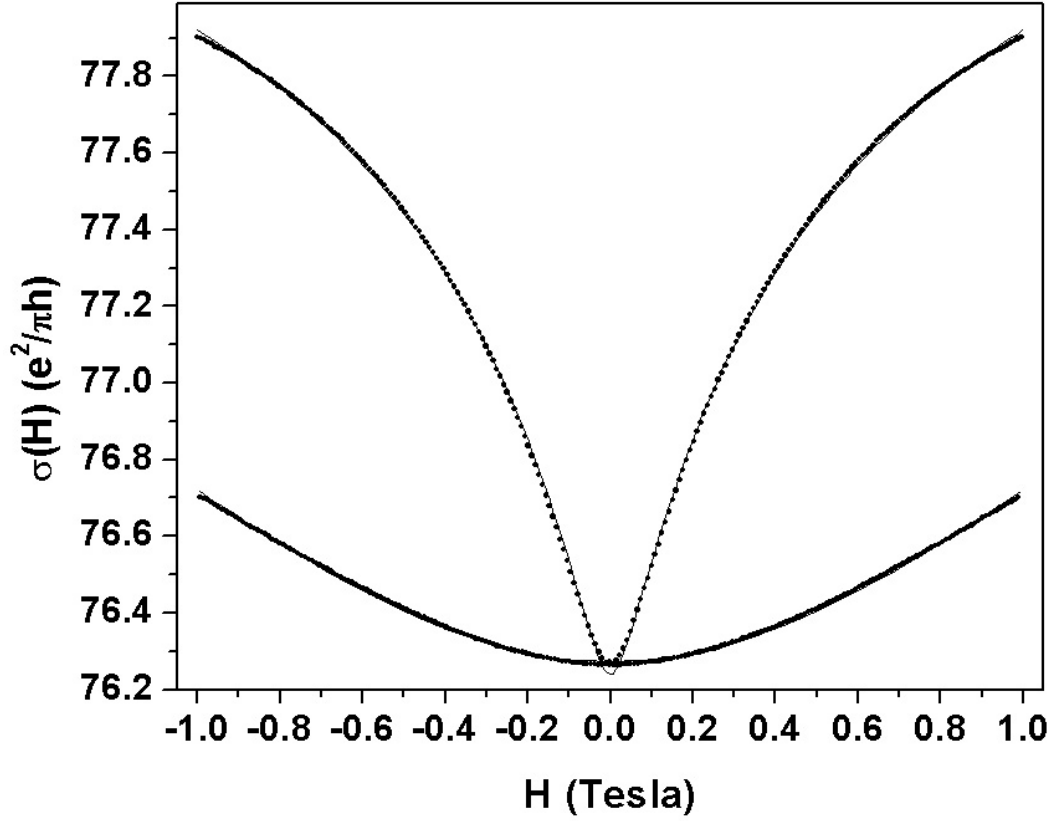
Figure 5.19: Weak localization data from the same device as the Hall data of Figure 5.18 (wafer C). The best-fit weak localization parameters for this device were $\ell_\phi = 81$ nm, $\gamma = 1.6/\text{T}^{-2}$.

One additional sample was measured, but *only* at T = 4.2 K. The reason for the abbreviated investigation of this device is that after measuring the density (n = $2.7\text{x}10^{13}$/cm^2) and resistivity (ρ = 2670 $\Omega/\square$), it was clear that this sample was still far from the desired parameter range of R$_\square \simeq$ h/e^2. Although a cursory perpendicular field measurement showed the expected negative magnetoresistance, instead of performing the standard weak localization measurements and analysis, the dilution refrigerator was cycled to room temperature, and additional samples were sought. As mentioned earlier, despite four different attempts, I was unable to obtain adequate samples, and was forced to conclude this aspect of my investigation.

The results of my work with respect to the two-dimensional MIT in Si:P are graphed in Figure 5.20. We see the expected behavior in this figure that as n is reduced, R$_\square$ increases. Furthermore, weak localization was clearly observed in all of these samples, although a thorough investigation was only performed on the three highest density devices. Completing this graph with progressively lower density samples would be my first research goal if I were to continue studying Si:P δ-layers.

5.1.3   Final Remarks and Summary

This section concludes my discussion of Si:P δ-layers. The material I present here is somewhat "sprawling", and follows no particular pattern. I include it merely to document my own thoughts and perspectives on the
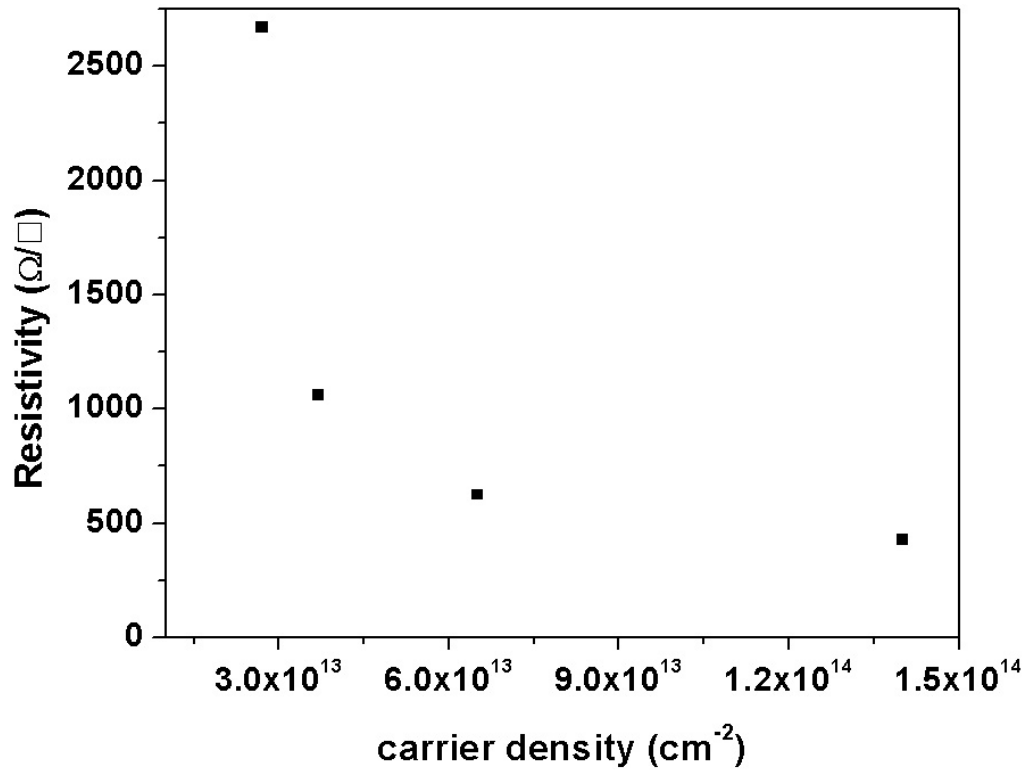
Figure 5.20: Metal-insulator transition data. As expected, the samples become more resistive as the carrier (doping) density n is decreased.

work I have performed, and to clarify why my density dependence work was truncated.

The reason for the diffusivity study was hinted at in Chapter 3, namely to determine how temperature influences $\mathcal{T}$. Being able to precisely quantify both $\mathcal{T}$ and how $\mathcal{T}$ varies with temperature is significant since this information sets thresholds on the temperatures and times which can be incorporated in various fabrication scenarios. Given a particular δ-doped wafer, it seems reasonable to assume that $\mathcal{T}$ throughout the sample is more or less uniform. It is also clear that heating the wafer to a sufficiently high temperature should cause the dopants to diffuse from their original positions in the crystal and increase $\mathcal{T}$. Given these considerations it is obvious that if one were to measure $\mathcal{T}$ of two devices from the same wafer, the device which was annealed at the same temperature but for a longer time should display a larger value of $\mathcal{T}$, and indeed this is shown by my data, as reported in [79].

The density dependence aspect of this work was concerned with establishing how a weak localization measurement of $\mathcal{T}$ depends on n, as well as establishing n_c, the crtical density for the metal-insulator transition in two-dimensions. Particularly interesting for study would have been devices with $R_\square \geq h/e^2$ ($h/e^2 \simeq 25.8$ kΩ), since this condition is equivalent to $k_F \ell_e \leq 1$ (appendix A), and the usual assumptions made when calculating $\delta\sigma(\mathbf{H})$ are invalid. Such an investigation would have allowed the crossover behavior of localization (from weak to strong) to be experimentally established, a

useful result for future theoretical work in this area.

Four separate attempts were made to obtain appropriately doped wafers, but each time the measured resistivity was either too low or too high to be meaningful. Lightly doped samples were tested, but all showed nonlinear I-V characteristics, and even measuring the Hall coefficient on these samples proved impossible (thus n could not be determined). The probable explanation for this behavior is that n in these samples was actually *below* n_c, the observed conduction was due to transport through an impurity band, and was consequently non-ohmic. As discussed in Chapter 3, n is controlled by varying the wafer's exposure time to the P source during growth (lower exposure times correspond to lower doping densities, and therefore higher resistivities). The non-ohmic samples were grown with exposure times of less than 40 seconds, while the low resistivity samples were exposed to the P source for 180 seconds or longer. In a seemingly foolproof effort to obtain highly resistive but ohmic wafers, I requested a series of samples with shutter times of 60, 80, 100, 120, 140, 160, and 180 seconds. Unfortunately, this attempt also failed. After roughly one week of trying to understand these results by performing a battery of processing tests, the effort proved hopeless and was abandoned.

Perhaps the failure to obtain proper samples can be explained by considering the SIMS data shown in Figures 5.1, 5.14, and 5.17. Several features are common to all of these plots. First, all show that the

background P level is much higher after opening the shutter ($\simeq$ 3x10^{18}/cm^3), than before δ-layer growth ($\simeq$ 5x10^{17}/cm^3). This is obviously undesirable. Second, the "bumps" in the spectra before the doping peak (i.e. deeper in the sample) likely correspond to the changes in substrate temperature during growth. These features are clearly much worse in samples B and C, which are decidedly "un-δ-like". Third, although the large surface signal common to all of these spectra is supposedly due to Si:H (see Chapter 3), I found that the surfaces did conduct T = 4.2 K, which is also unwanted. My guess is that the degradation in sample quality I observed and my inability to obtain wafers with specified doping levels had to do with some repairs that Phil made to his MBE system.

An interesting idea for future work would be to convolve a "SIMS potential" with my calculation for band structure. Since a higher doping density corresponds to a deeper potential well, "inverting" a SIMS spectrum would essentially define the potential energy environment experienced by the electrons in the sample. In other words, I expect that the eigen-energies would be given by an expression roughly of the form

$$E = \int n(z)E(n(z))dz \qquad (5.14)$$

where n(z) is specified by the SIMS data, and E(n(z)) is found from my calculation, given n. This is analogous to density functional theory, discussed in Chapter 2.

To summarize my results, the data shown in Figures 5.3 through 5.6, and

the corresponding parameters in Table 5.1, demonstrate that the effective conduction thickness, $\mathcal{T}$, of the 2DEG associated with a δ-doped layer can be measured using weak localization. Furthermore, all models for $\mathcal{T}$ are related to the perpendicular and parallel field weak localization parameters as

$$\mathcal{T} \sim \frac{\sqrt{\gamma}}{\ell_\phi}. \tag{5.15}$$

By determining $\mathcal{T}$ in several different samples annealed at T $=$ 850 $^\circ$C, an estimate of the diffusivity of Si:P has been established at this temperature [79].

Second, the ability to measure $\mathcal{T}$ was shown in samples with carrier densities ranging from approximately $10^{13}/\text{cm}^2$ to $10^{14}/\text{cm}^2$, and this weak localization technique works best in very thin δ-layers, since the signal contrast implied by (5.15) is higher in this situation. However, because ℓ_ϕ decreases with doping density n, for sufficiently low values of n this technique will ultimately fail, presumably when $R_\square \simeq h/e^2$. The influence of the Si:P Bohr radius on this limit has yet to be determined, although since the present theory of weak localization works best for samples with low values of $R_\square$, this implies a large overlap between the donor wave functions.

Finally, temperature and magnetic field dependent resistance measurements suggest that the phase coherence length, ℓ_ϕ, is limited by the electron-electron interaction, and my annealing experiments provide evidence for an enhancement of this dephasing due to lattice defects. Although a great deal of experimental knowledge has been gained about Si:P δ-layers in

Table 5.3: Results for all measured Si:P delta-doped samples discussed in this work, excluding the "cooked" devices of Table 5.1. The carrier density n was obtained from a linear fit to Hall data, and $R_\square$ is the zero-field resistivity. ℓ_e was estimated using equation (A.16), while ℓ_ϕ and γ correspond to the best fit values of the data to equations (5.2) and (5.3), respectively. $\mathcal{T}$ was estimated using $\mathcal{T} = (\hbar/2e)\sqrt{\gamma}/\ell_\phi$. Weak localization data was not obtained for the sample with n = 2.7×10^{13} e$^-$/cm^2.

wafer	n	$R_\square$	ℓ_e	ℓ_ϕ	γ	$\mathcal{T}$	$\mathcal{T_S}$
	e$^-$/cm^2	$\Omega/\square$	nm	nm	Tesla^{-2}	nm	nm
A	1.4×10^{14}	429	20.3	101	0.49	2.3	7.5
B	6.5×10^{13}	625	20.4	94	1.12	3.7	20.8
C	3.7×10^{13}	1063	15.9	81	1.6	5.1	11.6
D	2.7×10^{13}	2670	7.4	-	-	-	-

191

the course of these investigations, it is also clear that more theoretical work is needed to more accurately model the data, in particular with respect to the influence the correlation length ℓ_c has on the magnetoresistance.

These observations are contained in the data presented in Table 5.3 for all of the Si:P samples measured here.

5.2   Si:B δ-layers

Although the majority of the experimental work I performed was on Si:P δ-layers, the other shallow donor in Si, namely Boron (B), was investigated using the same techniques. Being a dopant from column III of the periodic table, B is an acceptor impurity in Si, and therefore the low temperature conduction characteristics displayed in Si:B samples are due to *holes*, not electrons. This makes these samples interesting to study in their own right, but having the two sets of data side-by-side is rather striking, demonstrating several differences that cannot be explained simply by changing the sign of the charge carriers. An accounting of the MBE growth and device fabrication methods, theoretical background, and results of these experiments now follows. The measurement techniques are exactly the same as for Si:P samples (see Chapter 4).

5.2.1 Sample Preparation

Epitaxially grown Si:B δ-doped wafers have, to this point, been studied much more intensively than Si:P samples; see, for example [93]. Segregation in these samples is not an issue, as evidenced by the SIMS analysis shown in Figure 5.21 (performed on a piece of the Si:B wafer used in these measurements). Unlike Si:P, the *backside* of the doping region in this sample appears to be more extended than the front, which is possibly an artifact of the SIMS measurement itself. For this profile, O_2 primary ions were used to bombard the sample, with an incident energy of 3 keV at angle of 52°.

A standard 50 μm x 50 μm Hall bar was constructed for measurement as described in Chapter 3. In order to make ohmic contacts to the B δ-layer, aluminum was evaporated and annealed, instead of the Au-Sb alloy used for Si:P devices. The reason for this choice is purely one of suitable interface chemistry, as trying to use Au-Sb to contact the δ-layer produced insulating samples at low temperatures. This behavior is easily understood when one considers that the Schottky barrier energy is *raised* when an n-type metallic alloy is brought into contact with a p-type semiconductor [19]. Aside from this contact detail, this sample was lithographically identical to the Si:P devices of the previous section and shown in Figure 4.2.
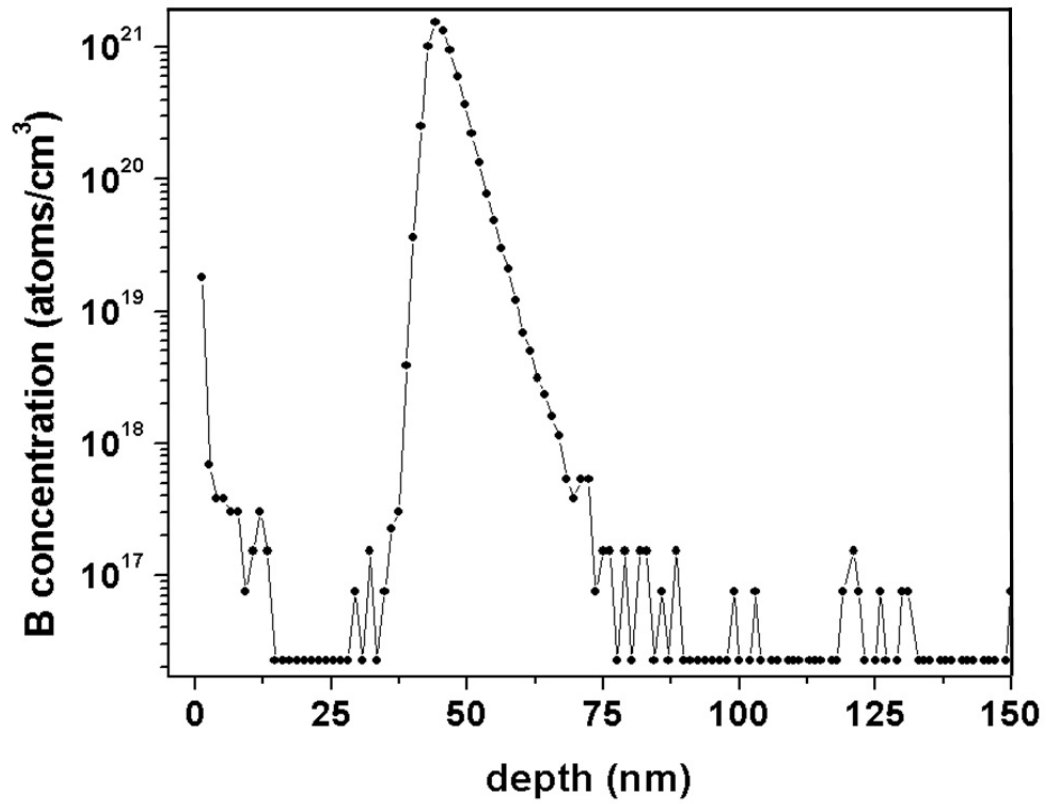
Figure 5.21: SIMS data for an Si:B δ-doped sample. The density of data points was sufficiently small that a line has been drawn through them to guide the eye.

5.2.2 Theory

Since we are considering *hole* transport in this section, several theoretical considerations come into play. One is the that the wave function of a hole has a $p-wave$ character, instead of the s-wave type P donors exhibit. Thus the symmetries obeyed by these wave functions will be different, and in turn so will the transport properties of devices fabricated from an Si:B δ-doped wafer. The primary manifestation of this asymmetry is a strong spin-orbit coupling, which leads to a *positive* magnetoresistance. The appropriate equation for modeling the magnetoconductance for $\mathbf{H} = \mathbf{H}_\perp$ is given by [53]

$$\delta\sigma(H_\perp) = -(\frac{e^2}{4\pi^2\hbar})[\Psi(\frac{1}{2} + \frac{\hbar}{4eH_\perp D\tau_\phi}) + \ln(\frac{4eH_\perp D\tau_\phi}{\hbar})]. \tag{5.16}$$

Note that this produces the desired *positive* magnetoresistance ($\delta\sigma(\mathbf{H}_\perp) < 0$ $\forall$ $\mathbf{H}$), and the prefactor is $(1/2)$ of that shown in (5.2). As before, instead of working with τ_ϕ I consider ℓ_ϕ through the relation $\ell_\phi = \sqrt{D\tau_\phi}$.

In parallel fields, I will use a slightly modified version of (5.3):

$$\delta\sigma(H_\parallel) = \alpha(\frac{e^2}{2\pi^2\hbar})\ln(1 + \gamma H_\parallel^2) \tag{5.17}$$

where α is an additional fitting parameter which I have introduced "by hand" (post hoc). In other words, I have no physical argument justifying the use of α, except that it's introduction allows the data to be fit better!
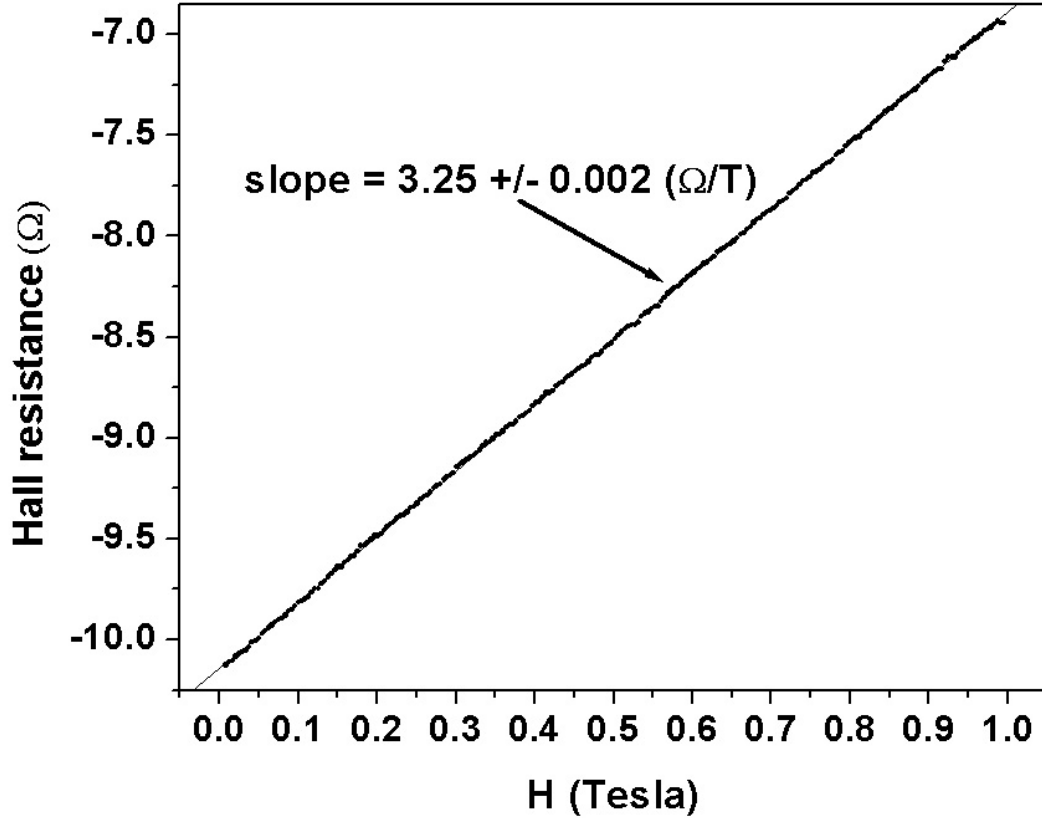
Figure 5.22: Hall data for the Si:B δ-doped device. The slope yields a hole density of n = 1.43x10^{14}/cm^2.

5.2.3 Results

First, I note that the Hall data in Figure 5.22 yields n = 1.43x10^{14}/cm^2 in this sample, a density comparable to the cooked Si:P devices of [79]. The zero-field sheet resistivity, however, is substantially higher: R$_\square$ = 2450 Ω/$\square$. Combining these quantities, I estimate the mean free path ℓ_e = 3.5 nm in this device. The density of data points in Figure 5.21 was too small to integrate and thus estimate the conduction thickness.

The weak localization data shown in Figure 5.23 yields the following results for the best-fit parameters: $\ell_\phi = 44.3$ nm, $\alpha = 0.09$, and $\gamma = 5.35/\text{T}^2$. The fact that α is significantly different from 1 strongly suggests the need for a better parallel field fitting equation than (5.17). Putting this question aside for future work and plowing ahead with the canonical analysis, I obtain an uncorrelated estimate of $\mathcal{T} = 17.2$ nm for this device.

Carrying out the analogous temperature and field dependent measurements on this sample produced several interesting results. First, by measuring the longitudinal resistance as the sample was cooled from T = 4.2 K to base temperature, a very strong saturation of the resistance was observed, setting in near T $\simeq$ 800 mK; see Figure 5.24. Although the physical reason for this behavior is unknown, similar results have been reported previously [94, 95]. Second, performing weak localization magnetic field sweeps at constant temperatures (Figure 5.25) showed that the width of the line shape *decreases* with T, as one would expect for a temperature-dependent dephasing time. I also note that the longitudinal magnetoconductance is well-fit by equation (5.16) all the way out to $|\mathbf{H}| =$ +/- 10 T. The best-fit value of ℓ_ϕ for this data is $\ell_\phi = 47.7$ nm, within 10% of the value obtained for sweeps between +/- 1 T. Thus another difference between Si:B and Si:P samples has been established: evidence of classical magnetoresistance effects is harder to discern in Si:B devices.

To summarize my results for this limited Si:B δ-layer study, I first note
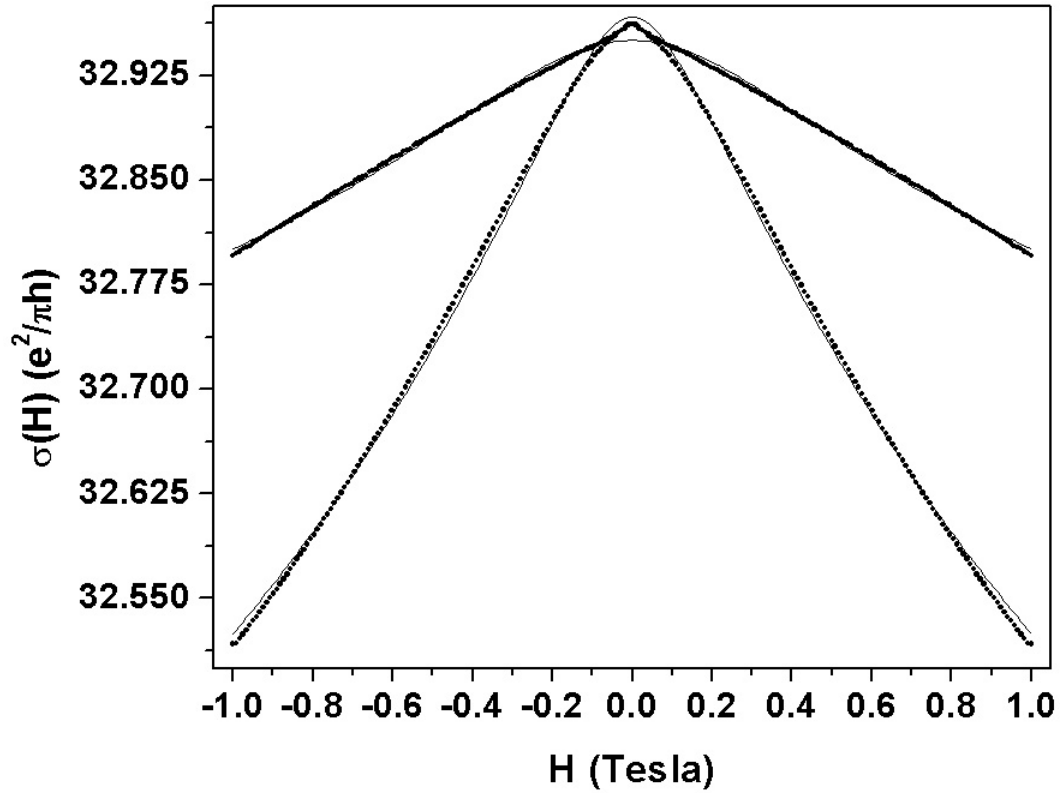
Figure 5.23: Weak localization data for the Si:B sample. Note the *negative magnetoconductance*, as compared to the positive magnetoconductance of Si:P samples. The best-fit parameters to equations (5.16) and (5.17) are $\ell_\phi = 44.3$ nm, $\alpha = 0.09$, and $\gamma = 5.35/\text{T}^2$. The fact that α is substantially different from unity suggests that (5.17) is an inadequate model for the parallel field magnetoconductance.
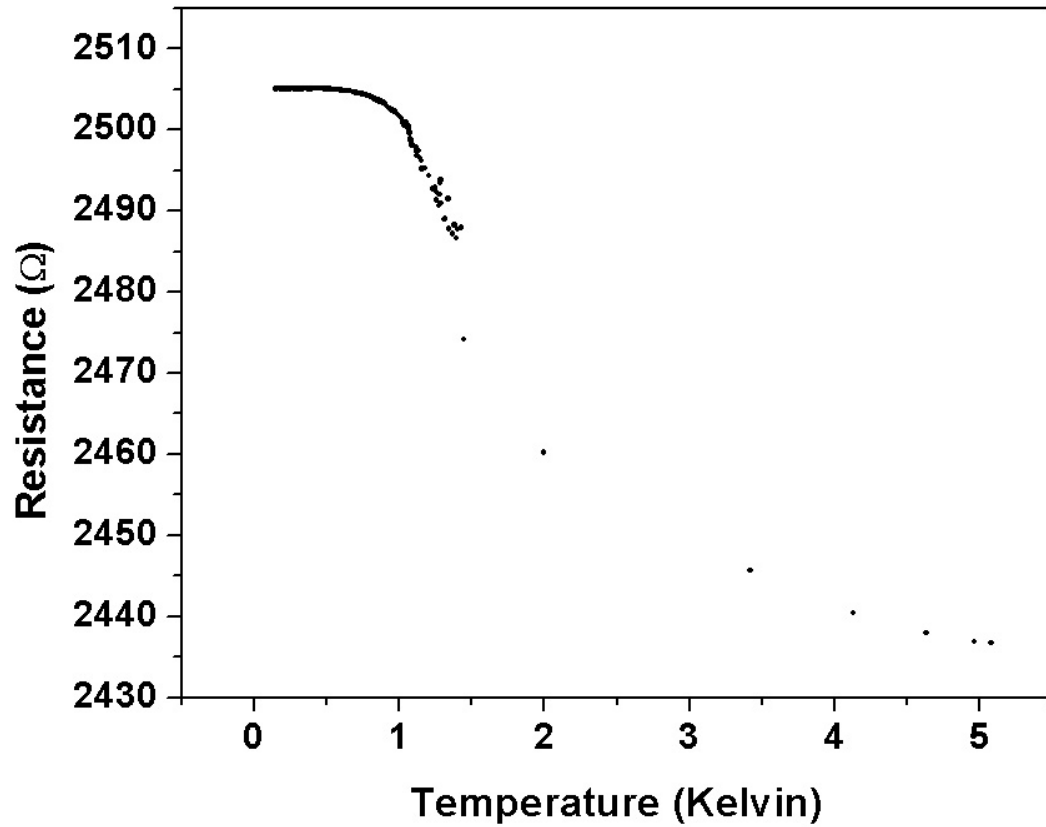
Figure 5.24: Si:B temperature dependent data in zero magnetic field. The saturation of this data occurs at a much higher temperature (T $\simeq$ 800 mK) than in Si:P samples (T $\simeq$ 200 mK). The origin of this behavior is unknown.
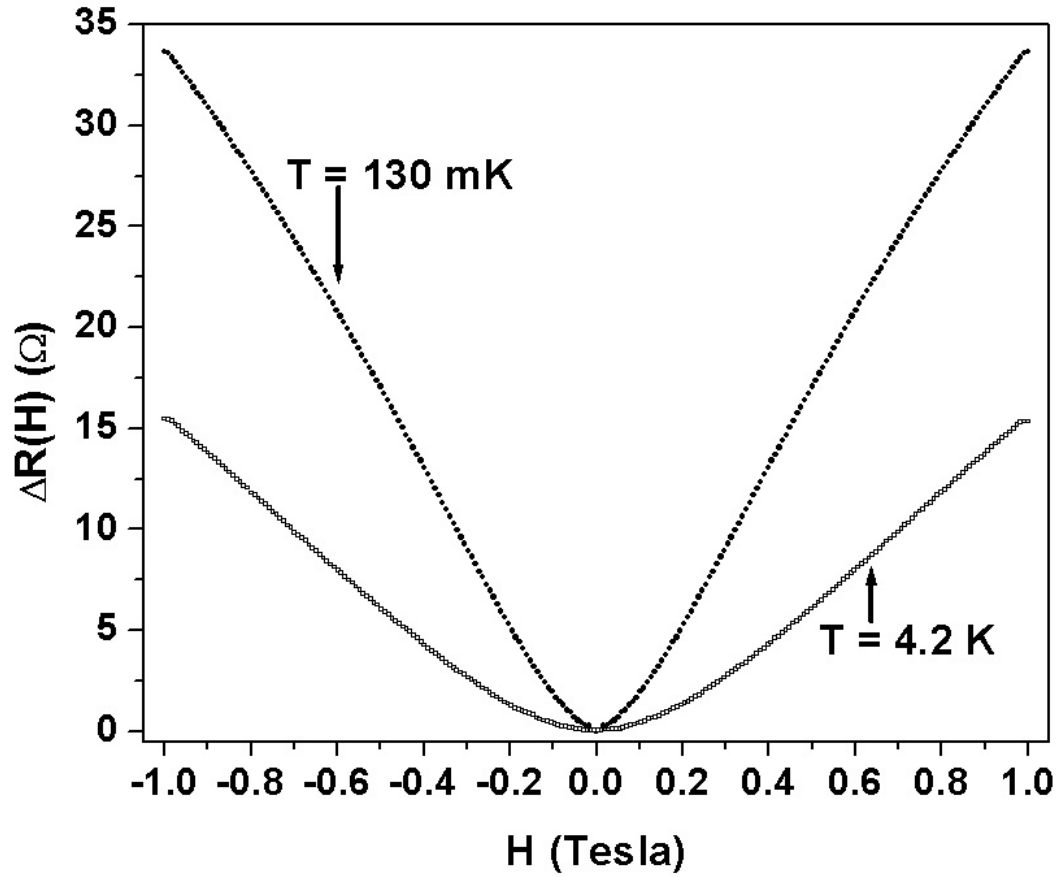
Figure 5.25: Si:B temperature-dependent data. As with Si:P samples, the lower the temperature, the narrower the line shape, due to the logarithmic dependence of ℓ_ϕ on temperature.
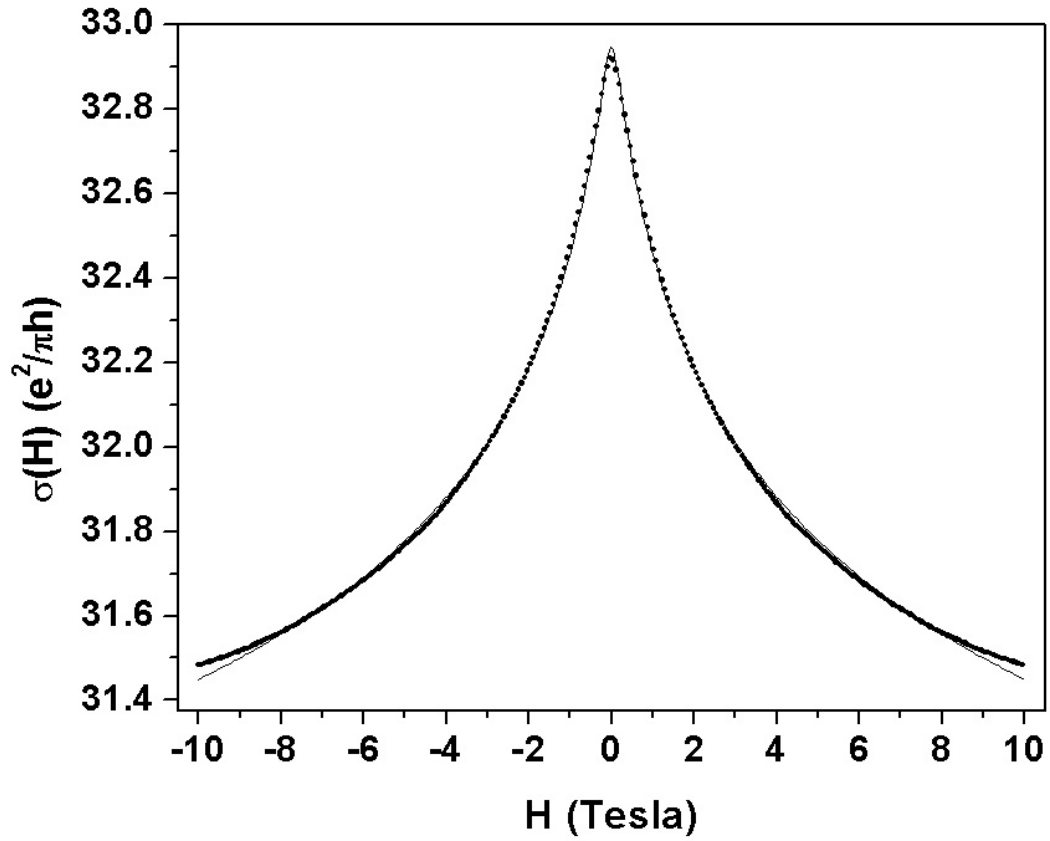
Figure 5.26: Large field sweep for Si:B sample. This data is to be contrasted with that of an Si:P sample (Figure 5.10), where non-monotonic behavior is observed. The line fit to this data yields $\ell_\phi = 47.7$ nm, close to that obtained when the field limits were only +/- 1 T ($\ell_\phi = 44.3$ nm).

that a positive magnetoresistance is observed for all fields and orientations, presumably due to the strong spin-orbit scattering effects associated with the p-wave B acceptor impurity. The device was substantially more resistive ($\sim$ 6x) than its Si:P counterparts of comparable density. The asymmetry between the $\mathbf{H}_\perp$ and $\mathbf{H}_\parallel$ data suggests that one should be able to measure $\mathcal{T}$ using weak localization in these samples, and from the best-fit parameters I estimate $\mathcal{T} = 17.2$ nm. However, the anomalously low value of α in equation (5.17) suggests that this area of the theory needs further development. Perhaps some interesting results relating to the spin-orbit effect in parallel fields are involved. Finally, I note that the R(T) curve saturates at a much higher temperature than in Si:P devices.

Chapter 6

Conclusion

A brief look at possible directions of future research and a summary of the results I obtained in the course of this work comprise the final chapter of this dissertation.

6.1 Future Directions

Several avenues for further work would be worthwhile pursuing. For one, determining the two-dimensional metal-insulator transition densities for both Si:P and Si:B would provide answers to a variety of interesting questions. Is this transition of the Anderson or Mott type? For what value of the carrier density does the canonical theory of weak localization, used throughout this dissertation, collapse? How do holes behave differently from electrons in this limit? Can aspects of the two-dimensional scaling theory of localization be

observed in δ-doped devices? Can x-ray diffraction studies be used to quantify lattice disorder and therefore probe the electron-electron interaction theory? Do Hall measurements yield additional information on the electron-electron dephasing time, τ_{e-e}? How does the *noise* of these samples change when in the presence of a magnetic field, including perpendicular and parallel to the plane of the δ-layer? The list is extensive, and no doubt will be eventually undertaken.

Another aspect of these samples worth exploring is in terms of $one-dimensional$ transport physics. This includes phenomena such as universal conductance fluctuations, different weak localization characteristics, etc [68]. Simply by reducing the *width* of the Hall bar to less than the phase coherence length (W $\ll \ell_\phi$), the device becomes effectively one-dimensional, literally a *nanowire*. Such an approach would be fairly easy to address from a fabrication standpoint using electron beam lithography, and a wealth of experimental possibilities also exist in this context.

In terms of actual device fabrication, constructing silicon single electron transistors (SETs), using either Schottky barriers or electrostatic gates, would be useful from a variety of perspectives. In immediate terms, having an alternative SET design would produce more knowledge on the charge offset phenomenon, which presently prevents SETs from being used in a current standard [13]. From a long-term perspective, investigating these devices would clarify whether or not their use as controllable charge

detectors is feasible.

Finally, detailed theoretical calculations of δ-doped silicon need to be realistically addressed. Most importantly for this dissertation, models of magnetoconductance phenomena incorporating the correlation length ℓ_c suitably defined for δ-layers need to be performed, in order that a competent experimentalist has the modeling necessary for a quantitative comparison with measurements.

6.2   Summary

To summarize this dissertation, δ-doping in silicon is technologically important, and Chapter 1 motivated my experiments. Chapter 2 discussed the three theoretical aspects of δ-layers crucial for interpreting the measurements presented in this work, including band structure, weak localization, and Berry phase. In Chapter 3, I discussed the epitaxial growth methods and device fabrication techniques incorporated in these experiments, along with the research of other workers. The measurement conditions and data acquisition approaches were the topics of Chapter 4. The results of my magnetoconductance experiments were presented in Chapter 5, including a study of the diffusivity of Si:P at T = 850 °C, testing the parallel field weak localization technique in Si:P devices with differing carrier densities, and an analogous set of measurements on Si:B δ-layers. Many differences were apparent in these samples, most notably that Si:P

δ-layers exhibit a *negative* magnetoresistance, while a *positive* magnetoresistance is observed in Si:B δ-doped devices, as expected.

6.3   Conclusion

Several noteworthy results were achieved in the course of this work. First, by adapting a previously demonstrated experimental technique employed on Si MOSFETs, I have established that a comparison of weak localization signals in perpendicular and parallel magnetic fields enables a precise measurement of the effective conduction thickness, $\mathcal{T}$, in a δ-doped Si device. Second, by measuring $\mathcal{T}$ in several devices subjected to T = 850 °C anneals, an estimate of the diffusivity in these epitaxially grown Si:P δ-layers has been produced. Third, by investigating the temperature and magnetic field dependence of these measurements, I have established that the electron-electron interaction is the primary mechanism limiting quantum mechanical phase coherence in Si:P δ-layers, and shown evidence for the enhancement of this effect due to lattice disorder, inherent in MBE growth techniques. Fourth, these characteristic weak localization phenomena were observed in numerous samples (four were discussed here), with carrier densities ranging from approximately 10^{13} to 10^{14} cm^{-2}, showing a reasonably broad range of applicability. Fifth, a brief study of Si:B δ-layers suggests that a complementary localization investigation in these structures would be informative and straightforward to carry out. Sixth and finally,

several theoretical issues with regard to the interpretation of these measurements have been suggested. In all, this work has been broad in scope, informative in its results, and, on the whole, enjoyable to carry out.

These results establish weak localization as a powerful tool in the materials analysis of ultra-thin conducting samples. Although weak localization has long been appreciated from rather esoteric theoretical and experimental perspectives, there are indeed practical applications of this phenomenon, as is evident by the work I have presented here.

Appendix A

Elementary Transport Theory

In this appendix I will derive several useful results concerning 2DEG transport. Although these are standard relations and straightforward to derive, having them all in one appendix is beneficial from a completeness standpoint, as well as establishing equivalent ways of interpreting my measurements. The quantities I consider include the conductivity, σ; the carrier density, n; the mean free path ℓ_e; the carrier mobility, μ; and the density of states, $\rho(E)$.

A.1   Classical Conductivity

Recall that the classical conductivity of a 2DEG, σ, is related to its resistivity ρ (or, equivalently, $R_\square$) by $\sigma = 1/\rho$. An expression for σ using Newton's second law, combined with Ohm's law, can be obtained as follows.

First, the application of an electric field **E** (in the form of a voltage bias) accelerates the electrons of a conducting sample in the direction *opposite* to **E**. The electrons (with effective mass m*), on average, accelerate for a time τ_e before experiencing a scattering event in which their momentum is randomized. Therefore, they acquire an average *drift velocity*, $\mathbf{v}_d$, before scattering. For the time-independent, steady state situation, the acceleration due to **E** and the momentum relaxation balance each other, i.e., we have the equality

$$\mathbf{F} = m^*\mathbf{a} = e\mathbf{E} - \frac{m^*\mathbf{v}_d}{\tau_e} = 0. \tag{A.1}$$

From this we obtain

$$\mathbf{v}_d = \left(\frac{e\tau_e}{m^*}\right)\mathbf{E}. \tag{A.2}$$

On the other hand, Ohm's law relates the current density **J** to the applied field **E** via

$$\mathbf{J} = \sigma\mathbf{E}. \tag{A.3}$$

If we assume that the sample has n electrons per unit area, **J** can also be expressed as

$$\mathbf{J} = ne\mathbf{v}_d. \tag{A.4}$$

Substituting (A.2) into (A.4), and equating this with (A.3), we obtain the well-known Drude result for the classical conductivity

$$\sigma = \frac{ne^2\tau_e}{m^*}. \tag{A.5}$$

I now discuss how n can be determined with Hall effect measurements. Before proceeding, however, I note that even with σ and n experimentally

determined (and the electron charge e obviously well-known), we still have incomplete information about the electrons in the sample, since the parameters τ_e and m* are unknown. Other measurements, beyond the scope of this thesis (such as Shubnikov de-Haas oscillations), must be performed to determine these quantities.

A.2 Hall Effect

Since the results of this thesis are very sensitive to the precise angle θ between the magnetic field **H** and the current density **J**, I now derive the relationship between these quantities and the Hall resistance, R_H.

To proceed, I consider the square Hall bar geometry of Figure 4.2, and assume, for the moment, that the electric current is carried by particles with *positive* charge q (I will later take q $= e$, the electron charge). When q moves with a velocity **v** in a magnetic field **H**, it experiences a Lorentz force **F** which is orthogonal to both these vectors, given by

$$\mathbf{F} = q(\mathbf{v} \times \mathbf{H}). \tag{A.6}$$

Since this force is proportional to the cross product of **v** and **H**, the *magnitude* of **F** depends on the angle θ between these vectors:

$$|\mathbf{F}| = q\,|\mathbf{v}|\,|\mathbf{H}|\,sin(\theta). \tag{A.7}$$

In words, if **v** and **H** are *parallel* ($\theta = 0$), no force acts on q, whereas if they are perpendicular ($\theta = \pi/2$), **F** is maximal. For perpendicular fields, q is

deflected towards one side of the device, determined by applying the

"right-hand rule" to (A.6).

Next, I take $\mathbf{v}$ to be the drift velocity $\mathbf{v}_d$ of the electric current in a

sample with n charges per unit area:

$$\mathbf{J} = nq\mathbf{v}_d. \tag{A.8}$$

From (A.7), I define an effective electric field, $\mathbf{E}_H$, associated with the Hall

effect, given by

$$|\mathbf{E}_H| = |\mathbf{v}_d||\mathbf{H}|sin(\theta). \tag{A.9}$$

Solving (A.8) for $|\mathbf{v}_d|$ and substituting this into (A.9) I obtain

$$|\mathbf{E}_H| = \frac{|\mathbf{J}|\,|\mathbf{H}|\,sin(\theta)}{nq}. \tag{A.10}$$

This "deflection" field pushes the electrons towards one side of the device,

thereby inducing a charge gradient across the sample, and consequently a

transverse *Hall voltage*, V_H. Since $V_H = -\int \mathbf{E}_H \cdot d\mathbf{l}$, and the line integral is

simply the transverse distance W across the width of the sample,

$$V_H = \frac{|\mathbf{J}|\,|\mathbf{H}|\,W sin(\theta)}{nq}. \tag{A.11}$$

However, as mentioned in Chapter 4, for a 2DEG, $|\mathbf{J}| = I/W$, where I is the

current bias through the device. Incorporating this relation into (A.11) and

taking q = e, I arrive at our final expression for the Hall voltage induced in a

2DEG:

$$V_H = \frac{I\,|\mathbf{H}|\,sin(\theta)}{ne}. \tag{A.12}$$

It is worth noting that V_H is independent of the device width W, and that V_H can naturally be associated with a *Hall resistance*, R_H, by dividing through by the bias current I:

$$R_H = \frac{|\mathbf{H}| \, sin(\theta)}{ne}.$$

(A.13)

The $sin(\theta)$ dependence was crucial in this research, since the Hall effect was used to determine the angle between the $\mathbf{J}$ and $\mathbf{H}$.

As implied by (A.13), plotting R_H versus $|\mathbf{H}|$ in perpendicular fields ($sin(\theta) = 1$), produces a line whose slope determines the carrier density, n. The importance of n can be appreciated by noting the frequency with which it appears in the following derivations.

A.3 Mean Free Path

An extremely useful length scale which can be inferred from magnetoconductance measurements is the mean free path, ℓ_e. The obvious relationship which holds on a microscopic scale is

$$\ell_e = v_F \tau_e$$

(A.14)

since the electrons are "whizzing" around the lattice at the Fermi velocity v_F and are scattered, on average, every τ_e seconds. Substituting this for τ_e in the Drude expression (A.5) for the *resistivity* yields

$$\frac{1}{R_\square} = \frac{ne^2 \ell_e}{mv_F} = \frac{ne^2 \ell_e}{p_F}.$$

(A.15)

212

The advantage of doing this is that now ℓ_e can be expressed in terms of two measurable quantities: the resistivity $R_\square$ and the density n (via Hall measurements). Substituting $p_F = \hbar k_F = \hbar\sqrt{2\pi n}$ into (A.15) and solving for ℓ_e, I find

$$\ell_e = \left(\frac{h}{R_\square e^2 \sqrt{2\pi n}}\right) = \left(\frac{h}{e^2}\right)\left(\frac{1}{R_\square k_F}\right). \tag{A.16}$$

Several features about this expression are noteworthy. For one, the prefactor of the resistance quantum, (h/e^2) highlights the quantum mechanical nature of electronic transport. Second, the fact that ℓ_e scales like $(1/R_\square)$ is physically appealing, since a device with a low value of $R_\square$ should have a long mean free path. Similarly, given that the donor atoms become ionized scattering centers for the electrons to bounce off of, the fewer of these scatterers are present, the longer ℓ_e should be, as suggested by the $(1/\sqrt{n})$ dependence.

Most relevant for this work, however, is the fact that $\ell_e \propto k_F^{-1}$. As mentioned in Chapter 2, calculations of the weak localization correction to the Drude conductivity, $\delta\sigma(\mathbf{H})$, are predicated on the so-called "disorder parameter", $k_F\ell_e$, being large compared to unity: $k_F\ell_e \gg 1$. What is immediately apparent from (A.16) is that this condition is *equivalent* to the resistivity being small compared to the resistance quantum:

$$k_F\ell_e \gg 1 \Leftrightarrow R_\square \ll \frac{h}{e^2}. \tag{A.17}$$

This inequality was satisfied for all of the samples investigated in the course of my research, with the smallest observed value of $k_F\ell_e$ being approximately

213

8. One of the original goals of this work was to determine precisely for what values of $k_F \ell_e$ did the "weakly localized" regime break down, which, according to (A.17) should occur for $R_\square \simeq (h/e^2)$ (approximately 25.8 kΩ). Unfortunately (as mentioned in Chapter 5), I was unable to obtain suitable samples for investigation, and consequently could not carry this program to fruition.

A.4   Mobility

An alternative measure of "how well a sample conducts" is the electronic mobility, μ, defined as the proportionality constant between the drift velocity, $\mathbf{v}_d$, and the applied electric field $\mathbf{E}$:

$$\mathbf{v}_d = \mu \mathbf{E}. \tag{A.18}$$

Of course, we can also express the current density as in (A.3) and (A.4):

$$\mathbf{J} = \sigma \mathbf{E} = ne\mathbf{v}_d. \tag{A.19}$$

Substituting (A.18) into (A.19), I find that

$$ne\mu = \sigma = \frac{1}{\rho}. \tag{A.20}$$

Therefore our final expression for μ becomes

$$\mu = \frac{1}{ne\rho}. \tag{A.21}$$

That nothing new has been introduced by considering μ can be seen by solving (A.21) for ρ and equating the result with that of (A.5). The result is

$$\mu = \frac{e\tau_e}{m^*}.$$ (A.22)

We are still left with the difficulty of disentangling the elastic scattering time τ_e with the effective mass m*, as mentioned in section A.1.

A.5 Density of States

I present here two calculations for the density of states, $\rho(E)$, of a two-dimensional electron gas. The first calculation assumes an isotropic mass (circular dispersion relation), while the second assumes an anisotropic mass (elliptical dispersion). Both of these results are used in my band structure calculation described in Chapter 2.

The physical significance of $\rho(E)$ is that it describes the number of electrons per unit area in a 2DEG as a function of energy. That is, if there are n_0 electrons in a given subband of a 2DEG with energies between E_1 and E_2, then $\rho(E)$ is defined by

$$n_0 = \int_{E_0}^{E_1} \rho(E)dE.$$ (A.23)

Equivalently, $\rho(E)$ can also be defined by differentiating both sides of equation (A.23) with respect to E:

$$\rho(E) = \frac{dn}{dE}.$$ (A.24)

Before carrying out the calculations, I briefly digress to make an important point regarding low temperature electronic transport.

Because electrons possess an intrinsic "spin" angular momentum equal to $\hbar/2$, they are classified as spin-1/2 fermionic particles. Consequently, they are subject to the Pauli exclusion principle, and obey Fermi-Dirac statistics. This is significant for my work since at low temperatures electronic conduction is entirely due to electrons within roughly $k_B T$ of the Fermi energy, E_F. This is apparent by considering the low temperature behavior of the Fermi-Dirac distribution function, which gives the probability that an electronic state with energy E is occupied [87]:

$$f(E) = \frac{1}{e^{\beta(E-E_F)} + 1} \tag{A.25}$$

where $\beta = 1/k_B T$. For $T \to 0$, all states with $E < E_F$ are occupied, while all states with $E > E_F$ are unoccupied. Given the low temperatures associated with the measurements in my experiments ($T \simeq 130$ mK), the assumption that the transport physics is dominated by electrons very close to E_F is clearly a good approximation.

A.5.1   Isotropic Mass

To derive $\rho(E)$ for a 2DEG with an isotropic mass m*, I consider a system of N such electrons confined to a square of side L at $T = 0$. According to the Pauli principle, the lowest single-electron energy levels are

doubly occupied up to the highest energy in the system, E_F. I now establish how E_F depends on N and L.

In **k**-space, the electrons will occupy all states out to some radius k_F, the Fermi wavevector, and states with $|\mathbf{k}| > k_F$ will remain unoccupied. The area of this "Fermi circle" is πk_F^2. Due to the boundary conditions that the wavefunction must be zero on the perimeter of the square, the smallest allowed wavevector, k_{min} will have a magnitude of π/L, and all other allowed wavevectors in the system will be integral multiples of k_{min}. For spin-zero particles, N is simply the ratio of the total volume occupied in **k**-space (πk_F^2) divided by the volume occupied by the *standing wave mode* corresponding to k_{min} $((2\pi/L)^2)$ [78]. For spin-1/2 electrons this ratio must be multiplied by 2 to take account of the spin degeneracy, and we have

$$N = \frac{k_F^2 L^2}{2\pi}. \tag{A.26}$$

Clearly the density of electrons $n = N/L^2$, and thus I obtain the following relation (used previously) between k_F and n:

$$k_F = \sqrt{2\pi n}. \tag{A.27}$$

Since I am assuming an isotropic dispersion relation (i.e. $E = \hbar^2 k^2/2m^*$), the Fermi energy is given by

$$E_F = \frac{\pi\hbar^2 n}{m^*}. \tag{A.28}$$

Therefore E_F in a 2DEG is directly proportional to n. Furthermore, since E_F is purely kinetic in nature, we can also identify $E_F = m^* v_F^2/2 = p_F^2/2m^*$,

where v_F is the Fermi velocity and p_F the Fermi momentum of the conduction electrons ($p_F = \hbar k_F$).

Given the discussion in Chapter 2 on band structure, it should be noted that this derivation neglects effects associated with interactions between the electrons, or band degeneracies due to the lattice symmetry, which *reduce* the value of k_F from that of (A.27) [28]. $\rho(E)$ is now easily found by solving equation (A.28) for n and then differentiating with respect to E_F. The result is

$$\rho(E) = \frac{m^*}{\pi \hbar^2} \qquad (A.29)$$

A.5.2 Anisotropic Mass

I now calculate $\rho(E)$ for a 2DEG with an elliptical dispersion relation. In other words, I consider a system (such as Si) in which the energy of an electron depends not only on the magnitude of $\mathbf{k}$, but also it's *direction*. Representing this dependence in Cartesian coordinates

$$E(k_x, k_y) = \frac{\hbar^2 k_x^2}{2m_x} + \frac{\hbar^2 k_y^2}{2m_y}. \qquad (A.30)$$

Generalizing my calculation for the isotropic mass, I assume that N electrons occupy a spatial region of dimensions L_x by L_y at T = 0. In $\mathbf{k}$-space, the length of the Fermi wave vector will now be directionally dependent, i.e. $\mathbf{k}^F$ = (k_x^F,k_y^F) (I use a superscript to keep the notation uncluttered). Thus the occupied area is given by an ellipse with semi-major and semi-minor axes

lengths of k_x^F and k_y^F. Again equating N with the ratio of occupied **k**-space to the minimum allowed based on L_x and L_y, I find

$$N = \frac{k_x^F k_y^F L_x L_y}{2\pi} \tag{A.31}$$

or

$$n = \frac{k_x^F k_y^F}{2\pi} \tag{A.32}$$

since the sample area $A = L_x L_y$.

E_F can be attained either for $k_x = 0$, $k_y = k_y^F$ or $k_x = k_x^F$, $k_y = 0$ (i.e. $k_x^F = \sqrt{2m_x E_F/\hbar^2}$, $k_y^F = \sqrt{2m_y E_F/\hbar^2}$). Substituting k_x^F and k_y^F into (A.32), I obtain

$$n = \frac{E_F \sqrt{m_x m_y}}{\pi \hbar^2}. \tag{A.33}$$

Finally, by differentiating (A.33) with respect to E_F, I arrive at my final expression for $\rho(E)$ in an anisotropic 2DEG:

$$\rho(E) = \frac{\sqrt{m_x m_y}}{\pi \hbar^2}. \tag{A.34}$$

Both of the above results for $\rho(E)$ shed light on why quantum Hall effect physics is of little concern for 2DEGs in δ-layers. The first quantum Hall plateau occurs when the ratio of the magnetic field to the carrier density equals h/e: $|\mathbf{H}|/n = h/e$. Inserting our canonical density of $10^{14}/cm^2$, I find that this requires a field of $|\mathbf{H}| \simeq 4000$ Tesla! It is highly improbable that such fields will ever be achieved on earth, and even samples with densities near the metal-insulator transition limit ($n \simeq 5 \times 10^{12}/cm^2$) require $|\mathbf{H}| \simeq 200$ T; still impractical fields. Thus, it seems unlikely that the quantum Hall

effect will ever be observed in δ-doped Si samples, even if one considers higher index plateaus (since the spacing between these plateaus decreases as the Landau level index increases).

Appendix B

Data Analysis Routines

This appendix contains the MATLAB (version 6.5) code which was used in various aspects of this work. Included are algorithms for fitting data to the perpendicular field correction to the conductivity, $\delta\sigma(\mathbf{H}_\perp)$, determining the resistivity of a device using the van der Pauw theorem, and estimating the δ-layer thickness based on SIMS data and Hall measurements. Linear fits to Hall data and logarithmic fits to $\delta\sigma(\mathbf{H}_\parallel)$ data were performed using pre-packaged routines in the Origin (version 6.1) library.

B.1 $\quad \delta\sigma(\mathbf{H}_\perp)$

The following three sets of code were used to fit perpendicular field weak localization data. The algorithm used by MATLAB was a nonlinear least-squares routine, which, according to MATLAB, incorporated a

"subspace trust region method based on the interior-reflective Newton method" (whatever that means). There were three subroutines to the which comprised the complete fitting algorithm: WL1p3, deltaGWL1p3, and perpfitWL1p3. The reason MATLAB was used for this task is that the digamma function, $\Psi(x)$, ("psi(x)" in MATLAB) is a built-in function in MATLAB, but not in Origin. Similar sets of code were written for fitting Si:B data, but have been omitted from this section.

B.1.1 WL1p3

The first part of the fitting routine, WL1p3 (for "weak localization 1, 3 parameters") is simply the MATLAB version 6.5 code for equation (5.2), with fitting parameters p(1), for the offset conductance (in units of $(e^2/\pi h)$), p(2) for the dephasing length ℓ_ϕ (in nm), and p(3) for the mean free path ℓ_e (in nm)). H obviously stands for the magnetic field value.

function Y = WL1p3(H,p)

if H==0

Y=p(1);

else

Y = p(1) + (psi(0.5 + (164.57)/(abs(H)*p(2)^2)) - psi(0.5 +

(329.14)/(abs(H)*p(3)^2)) + log(2*(p(2)/p(3))^2));

end

B.1.2   deltaGWL1p3

The second part of the fitting routine, deltaGWL1p3 (for "difference

(delta) between weak localization theory and measured data"), "loaded" the

measured data (gm) into the routine, calculated the theoretically expected

conductance (gc) using WL1p3 based on the values of the fitting parameters

p(i) defined above, and compared the difference between the two.

function G = deltaGWL1p3(p)

gm = load('C:\ data, etc\ perpSiPdata\ filename.dat');

[M,N]=size(gm);

k=1:M;

gc=zeros(M,N);

gc(k,1)=gm(k,1);

for i=1:M

gc(i,2)=WL1p3(gc(i,1),p);

end

for i=1:M

x(i)=gm(i,1);

G(i)=gm(i,2)-gc(i,2);

end

B.1.3   perpfitWL1p3

The last part of the routine, perpfitWL1p3 (for "fitting perpendicular field data to WL1p3") iterated the fitting procedure until the sum $\sum_i(\text{gc(i)-gm(i)})^2$ was minimized, which is essentially the same as minimizing χ^2. The fit was started with the initial parameters p0 and was constrained to remain within the physically reasonable bounds defined by lb and ub. This was carried out using the MATLAB's built-in non-linear least-squares fitting routine, "lsqnonlin".

p0 = [100 100 10];

lb = [0,10,1];

ub = [1e5,1e4,1e4];

[p,resnorm] = lsqnonlin(@deltaGp3,p0,lb,ub)

B.1.4 deltaLp

Unfortunately, the lsqnonlin routine in MATLAB 6.5 only produces the best-fit values for the parameters p(i), and not the uncertainties in these parameters. To overcome this deficiency, separate routines were written to perform this task, and here we show deltaLp (for "uncertainty in ℓ_ϕ"). The way the uncertainties were determined was to find the best-fit values of the parameters using perpfitWL1p3, gradually increment ℓ_ϕ away from its minimum while holding all other values fixed at their best-fit values, calculating a new value of χ^2 for each step, and iterating this procedure until χ^2 was doubled from its minimum value: $\chi^2 \to 2\chi^2$. According to [83], this procedure probably *overestimates* the errors in the fitting parameters, but when compared with the theoretical uncertainties facing the interpretation of these measurements, is relatively unimportant. The routine for finding the error in ℓ_e is virtually identical to that of ℓ_ϕ, and will not be shown here.

function f = deltaLp(gm,p)

[m,n]=size(gm);

```
for i=1:m

H(i)=gm(i,1);

gc(i)=WL1p3(H(i),p);

end


r0=chi2(gm,gc);


r=r0;


while (r <= 2*r0)

p(3)=p(3) + 0.001;

gc(i)=WL1p3(H(i),p);

r=chi2(gm,gc); end


r0

r

f=p(3);
```

B.2   van der Pauw Theorem

This routine takes two properly measured resistances from a van der
Pauw device, R1 and R2, and applies the van der Pauw theorem to

determine the resistivity ρ (here denoted by R).

R1 = input('Enter the first resistance:');

R2 = input('Enter the second resistance:');

R=(R1 + R2)/2;

x=exp(-pi*R1/R) + exp(-pi*R2/R);

if x < 1

while (1-x)>.0001

R= R + .001;

x = exp(-pi*R1/R) + exp(-pi*R2/R);

end

else

while (x-1)>.0001

R = R - .001;

x = exp(-pi*R1/R) + exp(-pi*R2/R);

end

end

R

B.3 SIMS $\mathcal{T}$

As discussed in Chapter 5, an estimate of the conduction thickness $\mathcal{T}$ can be obtained once given a SIMS profile and a Hall density, n. The way this is accomplished is by integrating the three-dimensional density of the SIMS plot until the resulting two-dimensional density equals that obtained by the Hall effect. The integration is started at the maximum value of the density in the SIMS plot, then symmetrically stepping away from the maximum and summing the contribution from each interval. The density of each interval is estimated by averaging the values of the endpoints, while the length of the interval is given by the difference in depths. The algorithm is shown below, where the parameter nH is the input Hall density, n2D is the "running tally" of the integrated SIMS density, and T the corresponding thickness estimate.

function F = SIMS(nS,nH)

nS=load('C:\data, etc\perpSiPdata\filename.dat');

nH=1.43e14;

[m,n]=size(nS);

```
for i=5:m

n(i-4,1)=1e-8*nS(i,1);

n(i-4,2)=nS(i,2);

end


[k,l]=size(n);


M=max(n);


for i=1:k

if (n(i,2)~=M)

continue

else

dM=n(i,1);

j=i;

end

end


T=(n(j+1,1)-n(j-1,1))*1e7;
```

```
n2D=((n(j-1,2)+n(j,2))/2)*(n(j,1)-n(j-1,1)) +

((n(j,2)+n(j+1,2))/2)*(n(j+1,1)-n(j,1));


p=0;


while (n2D<nH)

p = p+1;

T =(n(j+p+1,1)-n(j-p-1,1))*1e7;

n2D = n2D + ((n(j-p-1,2)+n(j-p,2))/2)*(n(j-p,1)-n(j-p-1,1)) +

((n(j+p+1,2)+n(j+p,2))/2)*(n(j+p+1,1)-n(j+p,1));

end

j

p

T

n2D
```

Appendix C

Dilution Refrigerator

Modifications

This appendix is primarily devoted to the wiring modifications which were performed on the dilution refrigerator used in these experiments. However, *twice* in the course of this work, the flow of the mixture became blocked at liquid nitrogen temperatures (presumably by pump oil), which necessitated the disassembly and cleaning of the refrigerator. Therefore, should the same fate befall some future graduate student, the procedures which were followed to remove the blockage will be briefly outlined.

C.1 Wiring

Originally, the dilution unit had ten wires available for measuring samples on it. Consequently, a maximum of one Hall bar or two van der Pauw samples could be measured in a single cooldown. After the second blockage occurred, it became clear that the time required to rewire the unit would be well spent by enabling much more data to be obtained in a given cooldown. Given the spatial constraints of the magnet bore (chapter 4), it was decided that twenty *sample* wires would be the maximum number which could be conveniently housed in the inner vacuum can (IVC). The various control and monitoring elements of the refrigerator, including the RuO_2 thermometers of the mixing chamber (MC), 1 Kelvin pot (1KP), and still, along with the MC and still heaters, also required additional wires.

It is probably easier to understand the wiring through the use of diagrams. To this end, figure C.1 shows the room temperature "breakout box" which serves as the electrical "point of entry" to the dilution unit. The twenty BNC connectors leading to the sample wires were each equipped with a toggle switch, allowing a direct connection to the corresponding sample wire at the MC when in the "up" position, and to ground when in the "down" position.

One detail which deserves mention is in regard to the thermometers. As mentioned in chapter 4, the thermometry was achieved via 4-wire measurements on calibrated RuO_2 resistors. Although 4 individual wires were used for measuring the MC thermometer, the 1KP and still
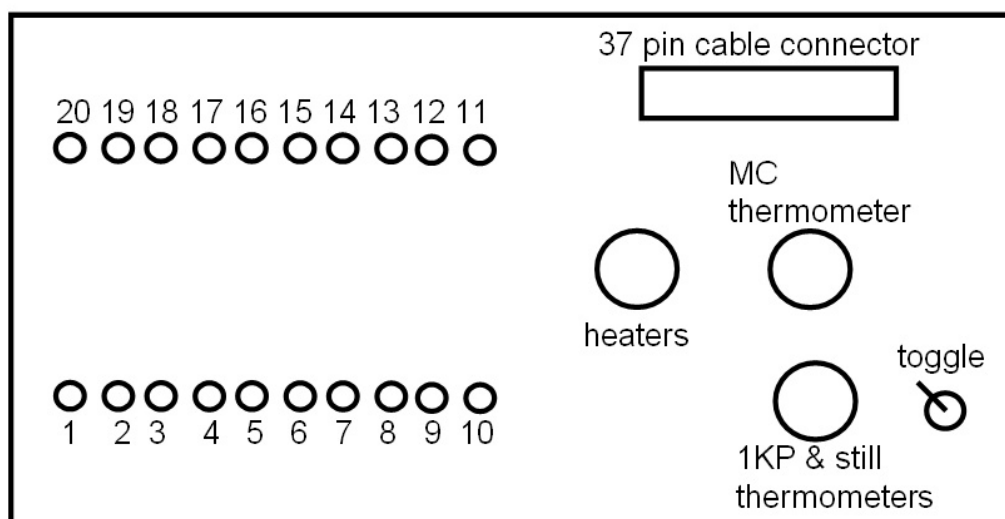
Figure C.1: Breakout box schematic used in these experiments. In addition to the 20 sample wires, this box also enabled the thermometers of the mixing chamber (MC), 1 Kelvin pot (1KP) and still to be monitored, as well as allowing power to be applied to the MC and still via the heaters. The 1KP and still thermometers were connected in *series*, and the toggle switch, when in the "up" position, measures the voltage across the 1KP thermometer. When toggled to the "down" position, the voltage across the still is measured.

|					
20	21			22	21
19	x			23	22
18	11			10	23
17	12			9	24
16	13			8	25
15	14		SAMPLE WIRES	7	26
14	15	SAMPLE WIRES		6	27
13	16			5	28
12	17			4	29
11	18			3	30
10	19			2	31
9	20			x	32
8	35	V+ MC therm	V- MC therm	36	33
7	34	I+ MC therm	I- MC therm	37	34
6	31	V+ 1KP therm	V- still therm	32	35
5	x			x	36
4	29	V- 1KP, V+ still	I- 1KPS therm	33	37
3	28	I+ 1KPS therm	still heater	25	38
2	24	still heater	MC heater	27	39
1	26	MC heater		x	40

37 pin cable contacts
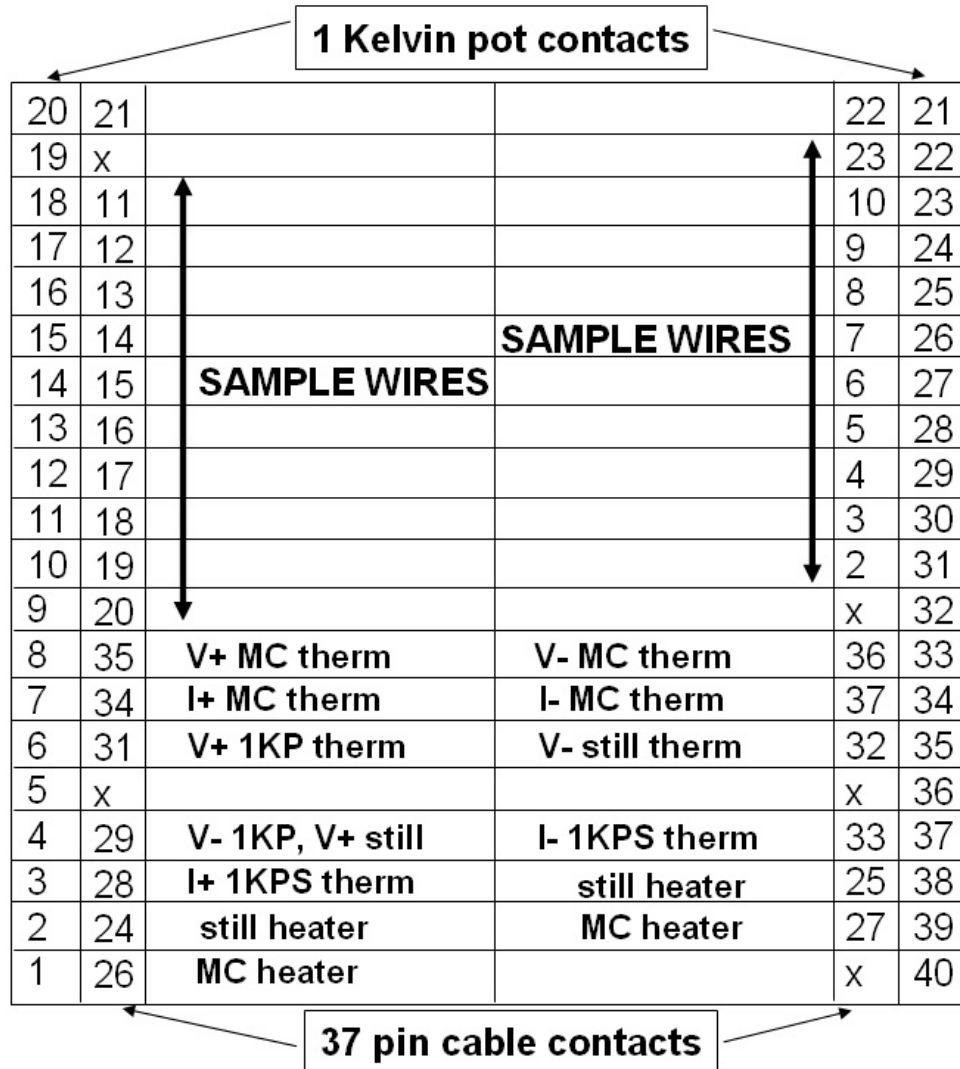
Figure C.2: Wiring diagram for the dilution refrigerator. As labeled, the outermost column corresponds to the wiring of the 40 pin connector at the 1KP. The next column in on either side corresponds to the wires associated with the 37 pin cable connector, which connects the breakout box to the refrigerator. The middle columns specify the function of each contact. An "x" denotes a pin which is either open or shorted to ground. Note that 1KP contacts 20 and 21 are available for use, should the need arise.

thermometers were connected in series, with the bias current first flowing through the 1KP resistor, then the still resistor. Thus the "bottom" (V-, low voltage end) of the 1KP and the "top" (V+, high voltage end) of the still were at the same potential. Because the Neocera temperature controller could only read two thermometers at a time, and one of these was dedicated to the MC, a toggle switch was implemented allowing one to read the 1KP when in the "up" position, and the still when in the "down" position.

The wires from the breakout box were connected to the dilution unit via a 37 pin cable connector, which before entering the unit were filtered through 1 MHz π filters, as discussed in chapter 4. The wires were then thermally sunk at 4.2 Kelvin, and then at the 1KP. At this stage, the wires were soldered to two, 20 pin DIP connectors, and from this point, the wires were distributed throughout the dilution unit to perform their respective functions. The 20 device measurement lines were further filtered by passing them through 10 kHz RC filters, and were thermally sunk at the still and the MC before being soldered to the sample mount on the tilt stage.

The correspondence between the breakout box wires, the 37 pin cable connector, and the 40 pin 1KP stage is shown in figure C.2. This figure assumes one is viewing the 1KP wires from the "front", that is, on the side *opposite* to where the wires enter the IVC, are thermally sunk on a 4.2 K post, then at the 1KP. The outer most columns represent the 40 contacts at the 1KP stage. Moving in from either side, the next set of columns

correspond to the wires associated with the 37 pin cable connector. The middle of the figure simply labels what function was performed by each pin. For example, the device wires correspond to pins 9-18 and 22-31 at the 1KP, and pins 11-20 and 2-10, 23, respectively on the cable connector, while the mixing chamber is measured with the current source wire I+ (1KP pin 7, cable pin 34) , current drain wire I-, (1KP pin 34, cable pin 37), and voltage contacts V+ (1KP pin 8, cable pin 35), and V- (1KP pin 33, cable pin 36). Those pins marked with an "x" are dysfunctional for one reason or another; either because they are open circuits, or shorted to ground. Note that there remain two unused wires (1KP pins 20 and 21), which could be serve as replacements for one of the components should the need arise.

Having said all of this, if a problem *does* arise (as it inevitably will at some point - this is experimental low temperature physics after all!), straightforward continuity tests with a hand held DVM go a long way towards understanding the source of the problems, and the diagram in figure C.2 should help. If you are reading this appendix because some electrical aspect of the apparatus isn't functioning properly, all I can say is good luck! You'll need it.

C.2   Repair

The last item which shall be discussed here are the steps to take should the dilution unit become blocked. A new rotary pump was purchased to

circulate the mixture, which hopefully will make this concern a non-issue. Unfortunately, if the unit does become blocked again, there are no quick-fix solutions. My experience shows that the blockage occurs in the condenser line of the refrigerator, which shouldn't be too surprising considering this is the smallest impedance in the unit. The only way to fix the problem is to disassemble the refrigerator, which is straightforward to do.

First, disconnect all wires below the still, so that the MC can be easily removed without being attached to the rest of the nit via wires. Next, *carefully* remove the mixing chamber from the rest of the refrigerator, by disconnecting both the MC and still, which requires nothing more than turning screws and bolts. Be especially careful with the condenser line, which is the most fragile part of the unit. After this, remove the "tail" from the mixing chamber (again by turning screws), which basically "splits open" the MC. Upon looking inside, you can see a small orifice (the condenser, where the mixture enters the MC) and a larger tube (the still line) which extends approximately 1 cm into the MC. At this point, you're ready to roll.

Support the MC so that it is in the upright position, and flush the condenser line with TCE (trichloroethylene). Be careful with this stuff, because it is carcinogenic. I had a fan blowing while I was dispensing it, as well as wearing gloves and a mask. J.B. Dotellis made a special apparatus to do this, so see if it's still around. It's an unmistakable contraption, since the two attachments are of just the right size to be attached to the still and

condenser lines. If you want, you can pressurize the condenser line with either nitrogen or helium gas to help force the TCE through. The TCE should start to drip fairly soon, but the "drip rate" is very slow, again due to the high impedance of the condenser line. The best thing to do is probably keep the condenser line pressurized with gas for about a week to be sure that all of the TCE has evaporated.

After the week has elapsed, the block should be cleared. You can now proceed to reassemble the refrigerator, and carry on with your research. My experience has been that by doing a "throughput" test with helium gas at liquid nitrogen temperatures, you'll know whether or not your efforts have been successful. A throughput test is nothing more than a mechanical continuity test to see if gas flows through the unit, and by pressurizing the condenser side of the unit to roughly 0.5 atmospheres with helium gas, then opening a valve to let it flow through the unit, do you see the pressure rise on the still side? If yes, the block is gone, if not...sorry.

I apologize if this explanation seems a bit terse and cryptic, but it really is this simple to fix a blocked dilution refrigerator. Rather than relying on the few paragraphs I have written here, I would also highly recommend calling Oxford instruments and speaking to one of their technicians about the problem. The people who talked me through this process for the first time were Mark Jackson and Nick Dent, both of whom were very helpful, especially "Jacko". Again, if you find yourself reading this because the unit

has become blocked, all I can say is good luck. I hope this appendix helps.

Bibliography

[1] Schubert, E.F., editor, *Delta-doping of semiconductors*, Cambridge
University Press, Cambridge (1996).

[2] Kittel, C., *Introduction to Solid State Physics*, sixth edition, John Wiley
& Sons, New York (1986).

[3] Ashcroft, N.W., and N.D. Mermin, *Solid State Physics*, Saunders College
Publishing, Fort Worth (1976).

[4] Kane, B.E., *Nature*, vol. **393**, p. 133 (1998).

[5] Shor, P.W., and S. Goldwasser, editor,
Proceedings of the 35th Annual Symposium of Foundations of Computer Science,
IEEE Computer Society Press, p. 124 (1994).

[6] Koiller, B., X. Hu, and S. Das Sarma, *Physical Review Letters*, vol. **88**, p.
027903 (2002).

[7] Schofield, S.R., N.J. Curson, M.Y. Simmons, F.J. Rueß,T. Hallam, L.
Oberbeck, and R.G. Clark, *Physical Review Letters*, vol. **91**, p. 136104
(2003).

[8] Gurtovoi, V.L., V.V. Valyaev, S.Y. Shapoval, S.V. Morozov, S.V. Dubonos, A.A. Asryan, and A.N. Pustovit, *Russian Microelectronics*, vol. **29**, p. 1 (2000).

[9] Heinig, K.H., T. Muller, B. Schmidt, M. Strobel, and W. Moller, *Applied Physics A*, vol. **A77**, p. 17 (2003).

[10] Hoenk, M.E., P.J. Grunthaner, F.J. Grunthaner, R.W. Terhune, M. Fattahi, and H.-F. Tseng, *Applied Physics Letters*, vol. **61**, p. 1084 (1992).

[11] Nikzad, S., Y. Qiuming, A.L. Smith, T.J. Jones, T.A. Tombrello, and S.T. Elliott, *Applied Physics Letters*, vol. **73**, p. 3417 (1998).

[12] Thompson, P.E., K.D. Hobart, M.E. Twigg, G.G. Jernigan, T.E. Dillon, S.L. Rommel, P.R. Berger, D.S. Simons, P.H. Chi, R. Lake, and A.C. Seabaugh, *Applied Physics Letters*, vol. **75**, p. 1308 (1999).

[13] Fujiwara, A., N.M. Zimmerman, Y. Ono, and Y. Takahashi, *Applied Physics Letters*, vol. **84**, p. 1323 (2004).

[14] Kane, B.E., N.S. McAlpine, A.S. Dzurak, R.G. Clark, G.J. Milburn, H.B. Sun, and H. Wiseman, *Physical Review B*, vol. **61**, p. 2961 (2000).

[15] von Klitzing, K., G. Dorda, and M. Pepper, *Physical Review Letters*, vol. **45**, p. 494 (1980).

[16] Taylor, B.N., and T.J. Witt, *Metrologia*, vol. **26**, p. 47 (1989).

[17] Tsui, D.C., H.L. Störmer, and A.C. Gossard, *Physical Review Letters*, vol. **48**, p. 1559 (1982).

[18] Laughlin, R.B., *Physical Review Letters*, vol. **50**, p. 1395 (1983).

[19] Sze, S.M., *Physics of Semiconductor Devices*, second edition, John Wiley & Sons, New York (1981).

[20] Hull, R., editor, *Properties of Crystalline Silicon*, INSPEC, The Institution of Electrical Engineers, London (1999).

[21] Lide, D.R., editor-in-chief, *CRC Handbook of Chemistry and Physics*, 85th edition, CRC Press, New York (2004).

[22] Hensel, J.C., H. Hasegawa, and M. Nakayama, *Physical Review*, vol. **138**, p. A 225 (1965).

[23] Shklovskii, B.I., and A.L. Efros, *Electronic Properties of Doped Semiconductors*, Springer-Verlag, Berlin, (1984).

[24] Goldstein, H., *Classical Mechanics*, second edition, Addison-Wesley, Reading, MA (1980).

[25] Hohenberg, P., and W. Kohn, *Physical Review B*, vol. **136**, p. 864 (1964).

[26] Pines, D., *Elementary Excitations in Solids*, W.A. Benjamin, Inc., New York (1963).

[27] Kohn, W., and L.J. Sham *Physical Review*, vol. **140**, p. A1133 (1965).

[28] Ando, T., A.B. Fowler, and F. Stern, *Reviews of Modern Physics*, vol. **54**, p. 437 (1982).

[29] Abramowitz, M., and I.A. Stegun, editors,

Handbook of Mathematical Functions, Dover, New York (1972).

[30] Pifer, J.H., Physical Review B, vol. **12**, p. 4391 (1975).

[31] Qian, G., Y.-C. Chang, J.R. Tucker, Physical Review B, vol. **71**, p.

045309 (2005).

[32] Ashbaugh, M.S., and Morgan III, J.D., Journal of Physics A, vol. **14**, p.

809 (1981).

[33] Iwabuchi, S., and Nagaoka, Y., Journal of the Physical Society of Japan,

vol. **58**, p. 1325 (1989).

[34] Agan, S., O.A. Mironov, E.H.C. Parker, T.E. Whall, C.P. Parry, V.Y.

Kashirin, Y.F. Komnik, V.B. Krasovitsky, and C.J. Emeleus,

Physical Review B, vol. **63**, p. 075402 (2001).

[35] Anderson, P.W., Physical Review, vol. **109**, p. 1492 (1958).

[36] Langer, J.S., and T. Neal, Physical Review Letters, vol. **16**, p. 984

(1966).

[37] Edwards, J.T., D.J. Thouless, Journal of Physics C, vol. **5**, p. 807

(1972).

[38] Abrahams, E., P.W. Anderson, D.C. Licciardello, and T.V.

Ramakrishnan, Physical Review Letters, vol. **42**, p. 673 (1979).

[39] Altshuler, B.L., and A.G. Aronov, A.L. Efros and M. Pollak, editors,

Electron-Electron Interactions in Disordered Systems, Elsevier,

Amsterdam (1985).

[40] Lee, P.A., and T.V. Ramakrishnan, *Reviews of Modern Physics*, vol. **57**, p. 287 (1985).

[41] Dolan, G.J., and D.D. Osheroff, *Physical Review Letters*, vol. **43**, p. 721 (1979).

[42] Bush, G.W., and R.B. Cheney, *et al.*, *Stealing Elections and Starting Wars*, enter "bush criminal" at www.google.com to see evidence of crimes committed between (2001-2005).

[43] Bergmann, G., *Physics Reports*, vol. **107**, p. 1 (1984).

[44] Chakravarty, S., and A. Schmid, *Physics Reports*, vol. **140**, p. 193 (1986).

[45] Aleiner, I.L., B.L. Altshuler, and M.E. Gershenson, *Waves in Random Media*, vol. **9**, p. 201 (1999).

[46] Jackson, J.D., *Classical Electrodynamics*, second edition, John Wiley and Sons, New York (1975).

[47] Sakurai, J.J., *Modern Quantum Mechanics Revised Edition*, Addison Wesley, Reading, MA (1994).

[48] Aharonov, Y., and D. Bohm, *The Physical Review*, vol. **115**, p. 485 (1959).

[49] Kubo, R., *Journal of the Physical Society of Japan*, vol. **12**, p. 570 (1957). Greenwood, D.A., *Proceedings of the Royal Society of London*, vol.

71, p. 585 (1958).

[50] Abrikosov, A.A., L.P. Gorkov, and I.E. Dzyaloshinskii,

Methods of Quantum Field Theory in Statistical Physics, Prentice-Hall,

Englewood Cliffs, NJ (1963).

[51] Rammer, J., and Pines, D., editor, *Quantum Transport Theory*, Perseus

Books, Reading, MA (1998).

[52] Mattuck, R.D.,

A Guide to Feynman Diagrams in the Many-Body Problem, second

edition, Dover, New York (1976).

[53] Hikami, S., A.I. Larkin, and Y. Nagaoka,

Progress of Theoretical Physics, vol. **63**, p. 707 (1980).

[54] Dugaev, V.K., and D.E. Khmel'nitskii,

Journal of Experimental and Theoretical Physics (JETP) Letters, English

translation of *Pis'ma v Zhurnal Eksperimental' noi i Teoreticheskoi Fiziki*,

vol. **59**, p. 1038 (1985).

[55] Giordano, N., and M.A. Pennington, *Physical Review B*, vol. **47**, p. 9693

(1993).

[56] Meyer, J.S., A. Altland, and B.L. Altshuler, *Physical Review Letters*,

vol. **89**, p. 206601 (2002).

[57] Pieper, J.B., J.C. Price, and J.M. Martinis, *Physical Review B*, vol. **45**,

p. 3857 (1992).

[58] Sarachik, M.P., D. Simonian, S.V. Kravchenko, S. Bogdanovich, V. Dobrosavljevic, and G. Kotliar, *Physical Review B*, vol. **58**, p. 6692 (1998).

[59] Berry, M.V., *Proceedings of the Royal Society of London*, vol. **392**, p. 45 (1984).

[60] Shapere, A., and Wilczek, F., editors, *Geometric Phase in Physics*, World Scientific, Singapore (1989).

[61] Mal'shukov, A.G., V.A. Froltsov, and K.A. Chao, *Physical Review B*, vol. **59**, p. 5702 (1999).

[62] Mathur, H., and H.U. Baranger, *Physical Review B*, vol. **64**, p. 235325 (2001).

[63] Eisele, I., *Superlattices and Microstructures*, vol. **6**, p. 123 (1989).

[64] Shen, T.-C., J.-Y. Ji, M.A. Zudov, R.-R. Du, J.S. Kline, and J.R. Tucker, *Applied Physics Letters*, vol. **80**, p. 1580 (2002).

[65] Oberbeck, L., N.J. Curson, M.Y. Simmons, R. Brenner, A.R. Hamilton, S.R. Schofield, and R.G. Clark, *Applied Physics Letters*, vol. **81**, p. 3197 (2002).

[66] Goh, K.E.J., L. Oberbeck, M.Y. Simmons, A.R. Hamilton, and R.G. Clark, *Applied Physics Letters*, vol. **85**, p. 4953 (2004).

[67] Kim, Y.B., M.R. Baklanov, T. Conrad, M. de Potter, and S. Vanhaeleemeersch, *Journal of The Electrochemical Society*, vol. **146**, p. 1549 (1999).

[68] Washburn, S., and R.A. Webb, *Reports on Progress in Physics*, vol. **55**, p. 1311 (1992).

[69] Onsager, L., *Physical Review*, vol. **37**, p. 405 (1931).

[70] Landauer, L., *IBM Journal of Research and Development*, vol. **1**, p. 223 (1957).

[71] Landauer, L., and B. Kramer, G. Bergmann and Y. Bruynseraede, editors, *Localization, Interaction, and Transport Phenomena*, Springer-Verlag, Berlin, p. 38 (1985).

[72] van der Pauw, L.J., *Philips Research Reports*, vol. **13**, p. 1 (1958).

[73] Büttiker, M., *IBM Journal of Research and Development*, vol. **32**, p. 317 (1988).

[74] Shibata, H, and R. Terakado, *Journal of Applied Physics*, vol. **66**, p. 4603 (1989).

[75] Ott, H.W., *Noise Reduction Techniques in Electronic Systems*, second edition, John Wiley & Sons, New York (1988).

[76] Misek, K., and P. Svoboda, *Cryogenics*, vol. **17**, p. 177 (1977).

[77] Wellstood, F.C., C. Urbina, and J.C. Clarke, *Physical Review B*, vol. **49**, p. 5942 (1994).

[78] Feynman, R.P., R.B. Leighton, and M.L. Sands, *The Feynman Lectures on Physics*, volume two, Addison Wesley, Reading, MA (1989).

[79] Sullivan, D.F., B.E. Kane, and P.E. Thompson, *Applied Physics Letters*, vol. **85**, p. 6362 (2004).

[80] Mensz, P.M., and R.G. Wheeler, *Physical Review B*, vol. **35**, p. 2844 (1987).

[81] Bahr, D., J. Falta, G. Materlik, B.H. Mueller, and M. Horn-von Hoegen, *Physica B*, vol. **221**, p. 96 (1996).

[82] Washburn, S., and R.A. Webb, *Advances in Physics*, vol. **35**, p. 375 (1986).

[83] Bevington, P.R., and D.K. Robinson, *Data Reduction and Error Analysis for the Physical Sciences*, second edition, McGraw Hill, New York (1992).

[84] Yonekybo, S., D. Ichiryu, and Y. Horikoshi, *Journal of Crystal Growth*, vol. **227**, p. 88 (2001).

[85] P. Shewmon, *Diffusion in Solids*, second edition, The Minerals, Metals & Materials Society, Warrendale, PA (1989).

[86] Chandrasekhar, S., and N. Wax, editor, *Selected Papers on Noise and Stochastic Processes*, Dover, New York (1954).

[87] Kittel, C., and H. Kroemer, *Thermal Physics*, second edition, W.H. Freeman and Company, New York (1980).

[88] Ross, S., *A First Course in Probability*, third edition, Macmillan, New York (1988).

[89] Hadara, Y.M., B.T. Folmer, M.E. Law, and T. Buyuklimanli, *Applied Physics Letters*, vol. **77**, p. 1976 (2000).

[90] Fisher, D.J., editor, *Diffusion in silicon: 10 years of research*, SciTec publications, Zurich, (1998), also online at www.scientific.net.

[91] Nassibian, A.G., and R.B. Calligaro, *Journal of Applied Physics*, vol. **48**, p. 1631 (1977).

[92] Mohanty, P., E.M.Q. Jariwala, and R.A. Webb, *Physical Review Letters*, vol. **78**, p. 3366 (1997).

[93] Thompson, P.E., and J. Bennett, *Journal of Applied Physics*, vol. **92**, p. 6845 (2002)

[94] Washburn, S., R.A. Webb, E.E. Mendez, L.L. Chang, and L. Esaki, *Physical Review B*, vol. **29**, p. 3752 (1984).

[95] Mattey, N.L., T.E. Whall, R.A. Kubiak, and M.J. Kearney, *Semiconductor Science and Technology*, vol. **7**, p. 604 (1992).